Diplomarbeit R-1229-D

Visibility studies and orbit determination of space debris objects for a combined passive-optical and laser ranging station

Jonas Radtke

November 2012

Seiten:	202
Abbildungen:	90
Tabellen:	52

Prof. Dr.-Ing. Peter Vörsmann
Technische Universität Braunschweig
Institut für Luft- und Raumfahrtsysteme
Hermann-Blenk-Straße 23, 38108 Braunschweig

Dr. Uwe Völker
Deutsches Zentrum für Luft- und Raumfahrt
Institut für technische Physik
Pfaffenwaldring 38, 70569 Stuttgart

Eidesstattliche Erklärung

Ich erkläre hiermit an Eides Statt, dass ich die nachfolgende Arbeit selbständig und nur unter Zuhilfenahme der angegebenen Literatur angefertigt habe.

Unterschrift

Braunschweig, den 19. November, 2012

Visibility studies and orbit determination of space debris objects for a combined passive-optical and laser ranging station

Abstract

At the Institute of Technical Physics at the German Aerospace Center (DLR-TP), a proposed concept combines two methods of well established orbital observations: First, optical observations using passive reflection of sunlight, which is in constant use for characterizing space debris in GEO regions. Second, an active satellite range laser ranging, which has been used for decades to measure distances to cooperative LEO and MEO objects at accuracies down to few millimeters.
In the new approach, passive optical observations shall first detect space debris objects in LEO regions during twilights and following guide a laser to illuminate the object for a high accurate range measurement.
In the scope of this thesis, first a general assessment of the accuracy of initial orbit determination with three different space debris observation techniques (radar, passive-optical and combined laser ranging and tracking) have been performed, to point out general advantages of the laser ranging methods regarding accuracies.
Following, using ESA's PROOF-2009 (**P**rogram for **R**adar and **O**ptical **O**bservation **F**orecasting), different studies were performed to assess the general visibility of space debris in LEO regions. These studies have been undertaken both for the, currently under construction, DLR Space Debris Observatory in Stuttgart with the given hardware of this station as well as for more generalized hardware and locations. Results include both the characteristics of detected objects regarding their seizes, as well as variations of their amount over different viewing directions and seasons.
Following, a FORTRAN tool has been written to further analyze these detected objects regarding their use for tracking and orbit determination. These final analyses have been performed for different PROOF runs. Results here show that from the total number of detectable objects only a fraction can be used for further determinations.

Contents

Nomenclature

constants

G	gravitational constant	$6.67384 \frac{m^3}{kg \cdot s^2}$
μ	gravitational parameter (for Earth)	$398600.4418 \frac{km^3}{s^2}$

Latin symbols

A	effective surface	$[m^2]$
A	azimuth	$[rad]$ or $[deg]$
a	semi major axis	$[m]$ or $[km]$
B_c	ballistic coefficient	$[m^2/kg]$
c	coefficient	$[-]$
D	drag	$[N]$
E	eccentric anomaly	$[^\circ]$ or $[rad]$
e	eccentricity	$[-]$
$\vec{e}$	eccentricity vector	$[-]$
$\vec{e}$	unit vector	$[-]$
f, g	f and g functions	$[-]$
h	elevation	$[rad]$ or $[deg]$
i	inclination	$[^\circ]$ or $[rad]$
L	line of sight matrix	$[-]$
$\widehat{L}$	line of sight vector	$[-]$
M	mass	$[kg]$
M	mean anomaly	$[^\circ]$ or $[rad]$
$\widehat{P}, \widehat{Q}, \widehat{W}$	basis of perifocal system	$[-]$
p	semi latus rectum	$[m]$ or $[km]$
r	length of a vector	$[m]$ or $[km]$
$\vec{r}$	position vector	$[m]$ or $[km]$
$\vec{r}$	state vector	$[m, m/s]$ or $[km, km/s]$

S	area of an orbit section	$[m^2]$
t	time	$[s]$
u	argument of latitude	$[^\circ]$ or $[rad]$
V	velocity	$[m/s]$ or $[km/s]$
$\vec{W}$	Gaussian vector	$[-]$
z	zenith angle	$[rad]$

(Symbols that appear more than once are explained in more detail in the text)

Greek symbols

α	right ascension	$[^\circ]$ or $[rad]$
Δ	area of orbit triangle	$[m^2]$
Δ	indicates a difference between values	$[-]$
δ	declination	$[^\circ]$ or $[rad]$
ζ	zenith angle for refraction	$[rad]$
η	ratio of the areas of orbit triangle and section	$[-]$
Θ	phase angle	$[rad]$
λ	pixel scale	$[''/pixel]$
ν	true anomaly	$[^\circ]$ or $[rad]$
ρ	slant range	$[km]$
ρ	atmospheric density	$[kg/m^3]$
τ	time difference	$[s]$
Ω	right ascension of ascending node	$[^\circ]$ or $[rad]$
ω	argument of perigee	$[^\circ]$ or $[rad]$
ω_{ATM}	rotational velocity of atmosphere	$[m/s]$

(Symbols that appear more than once are explained in more detail in the text)

Indices

$\oplus$	earth
1, 2, 3	row of positions
AT	atmosphere
a	subscript for point A
b	subscript for point B
$ECEF$	ECEF coordinate system

ECI	ECI coordinate system
G	geopotential
i	subscript counter for iterative process
obs	observer
p	(per) pulse
pert	perturbations
SENS	sensor coordinate system
r	relative
u	subscript for unit vectors
vac	vacuum
x	coordinate axis x
y	coordinate axis y
z	coordinate axis z

Abbreviations

aop	argument of perigee
ATM	atmosphere
DLR	German Aerospace Center
DLR-TP	Institute of Technical Physics at DLR
ecc	eccentricity
ECEF	Earth Centered Earth Fixed
ECI	Earth Centered Intertial
ECSS	European Cooperation for Space Standardization
G	geopotential
GEO	Geostationary orbit
incl	inclination
IERS	International Earth Rotation and Reference System Service
LEO	Low Earth Orbit
LOS	Line of sight
LST	Local sidereal time
meanA	mean anomaly
MLI	multi layer insulation
NaK	sodium-potassium
OBJ	Object
OBS	Observer

ODE	ordinary differential equation
PROOF	Program for Radar and Optical Observation Forecasting
RAAN	right ascension of ascending node
ROT	Rotation by given angle around axis
SEZ	South, East, Zenith (topocentric observer coordinate system)
sma	semi major axis
SRM	solid rocket motor slag and dust
SSA	Space situational awareness
TEME	True Equator Mean Equinox
TLE	two line element
UTC	Universal Time Coordinated

Chapter 1

Introduction

1.1 Current situation in space debris observation

Latest since two crucial on orbit break-up events in 2007 and 2009, space debris is getting a growing concern to all satellite operators. As shown in figure 1.1 this problem especially affects highly inclined orbits, which have very useful characteristics for earth imaging or other remote sensing satellites. As technologies to remove space debris are still in development and wont be available in the near future, the only way to prevent spacecraft from colliding with space debris is to perform active avoidance maneuvers before collisions. To accomplish this, accurate orbits from as many space debris objects as possible are needed.

During mission design, ESA's MASTER-2009 (**M**eteroid **a**nd **S**pace Debris **T**errestrial **E**nvironment **R**eference) helps assessing the risk of space debris collisions on designated objects [2]. Due to its statistical approach it is very helpful for general risk assessment, during missions the operator must know the actual position of deterministic objects though.
For this purpose, space surveillance systems do exist. Tasks of these systems are to 'detect and track space objects, correlate them with launch events, determine their orbits, and characterize them with respect to physical properties' [3]. In general, different space surveillance systems exist at different state of completion: The US Space Surveillance Network (USSSN), the Russian Space Surveillance System (SSS), and the French GRAVES (**G**rand **R**éseau **A**dapté à la **VE**ille **S**patiale) system, which is still in experimental stage. Regarding the survey capabilities, the USSSN is by far the most comprehensive one. The data to feed these systems are determined with different measurement. In operational stage, a ground-based network of radar and optical sensors detects, tracks, correlates, and characterizes objects of sizes larger than 10 cm at alti-

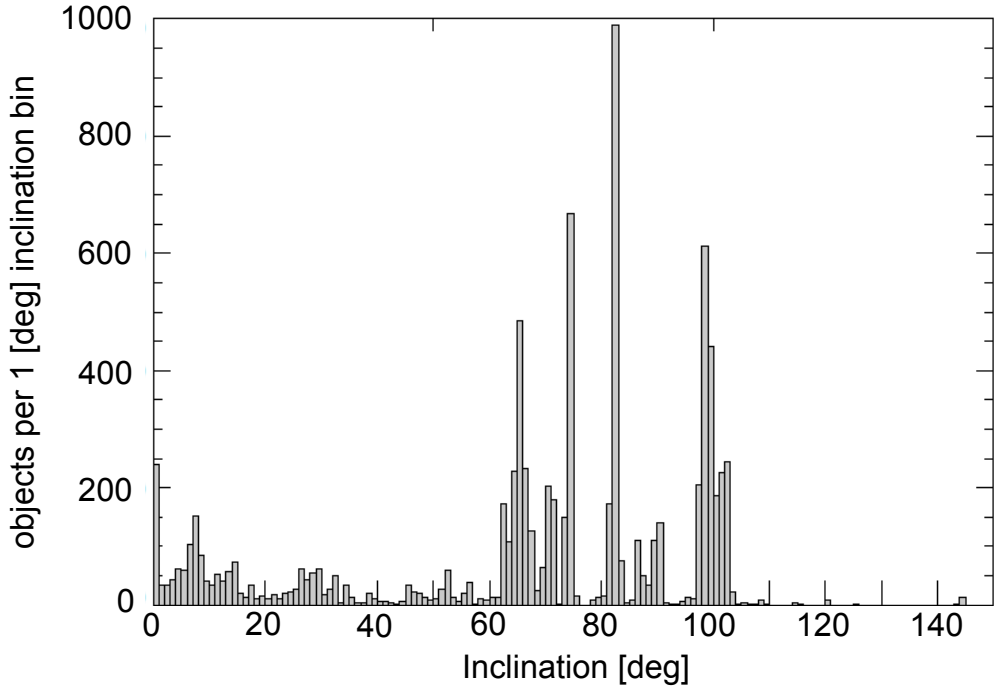

Figure 1.1: Distribution of cataloged objects over Inclination [1].

tudes up to GEO to maintain a catalog of about 15000 objects for open access (excluding military objects). Other methods are currently in an experimental development stage, which include mono- and bi-static radar beam park experiments, use of phased array radars and furthermore additional optical sensors, like the ESA's 1 m telescope for GEO and GTO observations.

From with the current technologies available capabilities arises the problem of being able to track only a certain amount of space debris with a certain accuracy. From the great number of space debris objects arises the problem of being able to track only a certain amount of space debris with a certain accuracy. The more accurate the data shall be, the less objects can be tracked (with the same number of sensors). One way to encounter this problem would be to extend the number of sensors. But as especially radars being very cost-intensive, this is very hard to enforce. So the Institute of Technical Physics of the German Aerospace Center (DLR) was looking for a new, less cost-intensive approach for both survey and accurate tracking: The idea is to complement the existing systems by a combined passive optical (survey) and laser ranging and tracking system for LEO objects. In here, a passive optical telescope would take over the part of detecting space debris objects to gain an initial orbit. From there, the laser tracking system would take over to gain a more accurate 3D positional data set employing laser ranging. Due to the high precision of orbit determination following this approach such system could furthermore help to keep the existing data much more

accurate at lower cost, or gain accurate data in case of collision warnings.

The present thesis is divided into three parts:
At first, a general assessment of initial orbit determination of the three different systems, which are radar measurements, passive optical angle-only measurements and combined laser ranging and tracking, is given in chapter 2. In the scope of that chapter, also some later on needed theoretical background about initial orbit determination and orbit propagation is presented.
In the second part (chapter 3) the DLR Space Debris Observatory in Stuttgart is described, and simulations with PROOF 2009 are performed. These simulations first assess the performance concerning the detectable objects of the station in Stuttgart, followed by simulations regarding the scaling and positioning of such a station.
In chapter 4, sightings of objects are analyzed regarding their re-detectability. For this, a written analysis tool is described and later used for analysis. As input for the analysis, results from prior simulations with PROOF are used.
But before going into the actual work, shortly both the DLR project for laser-based monitoring of space debris and the used software PROOF2009 are introduced.

1.2 Laser based space debris monitoring

To this point, space debris observation methods have been separated by basically using radar measurements for low earth orbits and passive optical observations for orbits up to GEO regions. This is reasoned by first the signal's decay during active measurements, and second by the difficult observational conditions for low earth objects regarding visibility, limited observation times etc.
The Institute of Technical Physics (DLR-TP) at the German Aerospace Center (DLR) in Stuttgart proposed another kind of measurements for low orbiting space debris, a laser-based method [4]. In this method, due to high precision ranging of the object by time-of-flight measurements with the laser, high accuracies can be achieved. The basic idea of this approach has been used and further developed over the last decades by the satellite laser ranging (SLR) community: In here, with time-of-flight measurements of short laser pulses directed towards retro reflector equipped satellites, accuracies down to few mm on 10000 km distances can be achieved [5]. As a space debris object is not comparable to a cooperative retro-reflector satellite, of course the laser's pulse energy would have to be adjusted, but the general components would be identical. Currently intended are a pulse energy of $E_p \approx 1$ J at a repetition rate of 1 kHz.
This approach could recently be demonstrated in cooperation with SLR station in Graz

[6]: During this measurement campaign, 85 passes of 13 different non cooperative targets could be successfully tracked, in distances between 600 and more than 2500 km, with radar cross sections from larger than 15 m down to 3 m. The used laser emits at a wavelength of 532 nm with a pulse energy of 25mJ, 10ns pulse length and a 1kHz repetition rate. For this campaign, only known objects for which predictions from TLE data strings could be calculated were tracked. So the next step is developing methods to passive optically detect and track low earth space debris objects. For this purpose, the DLR-TP is currently setting up a passive optical Space Debris Observatory at the Schwäbische Sternwarte[1] in Stuttgart. This station is described in more detail in chapter 3.1.1.

1.3 PROOF2009

PROOF[2] (**P**rogram for **R**adar and **O**ptical **O**bservation **F**orecasting) is a software for the simulation of radar- and telescope-based space debris observation. It has been developed by the Institute of Aerospace Systems at the Braunschweig University of Technology under ESA contract, together with MASTER. The software can be used for different purposes like:

- Validation of space debris models (i.e. MASTER),
- Analysis of measurement data,
- Planning of observation campaigns.

To conduct simulations, several modes are available. These include statistical, deterministic or hybrid modes, both for radar and optical wavelengths. Also, it can be chosen if the sensor is ground- or space-based, if it shall track objects along a predefined tracking line of sight and if the observation is mono- or bistatic (for radar). In the scope of this work, only statistical observations in a locally fixed staring mode with a ground-based optical telescope have been performed.
As objects, by default statistical MASTER populations are used, which come with the program for certain epochs. The objects for the statistical mode are grouped into the most common sources of space debris. These sources are TLE-objects, fragments, sodium-potassium droplets (NaK-droplets), solid rocket motor slag and dust (SRM), Westford needles and multi-layer insulation (MLI). For each of these object groups, the user can define an albedo with a certain range of a standard deviation. Furthermore, these objects are modeled either as spheres or as averaged randomly tumbling plates.

[1] www.sternwarte.de
[2] software available from www.master-model.de

All objects are modeled as gray objects.
The sensor is always assumed to be a square CCD, no overexposure is possible. The telescope itself is working in the range of visible light. Quantum efficiencies can be considered via an input file.
The model of background radiation considers a wide range of both deterministic and continuous sources. As deterministic, the sun, the moon and the stars up to a user defined magnitude are included. Continuous sources contain all fainter stars, galaxies, airglow, zodiacal light and atmospherically scattered light from all those sources. It has to be noted that no artificial light sources (e.q. light pollution) are modeled within PROOF.
The atmospheric influence on the received signal from an orbiting object is taken into account by the atmospheric transmission. It is considered to be both wavelength and elevation dependent. The wavelength dependency can be changed in a file to adjust it to the site's conditions. The effect of refraction is only realized for deterministic simulations, atmospheric turbulences are not implied at all. For the irradiation of objects by the sun, no atmospheric effects are considered. This seems fair enough, as there would be an effect only on very some very low orbiting objects.
This little overview only means to give a insight on the conditions for which the performed simulations are valid. For further information about PROOF2009, the reader can refer to [7].

Chapter 2

Comparing the space debris observation methods

To classify the field of application for the described laser based approach of space debris measuring, at first a comparison of the different measurement systems (radar, passive-optical and combined passive-optical/ laser ranging) will be given. Basis for the comparison is the possible accuracy to be reached by the different systems. At start, some needed theoretical background about preliminary orbit determination and propagation are presented. Subsequently a short description of the written analysis tool follows. Next, estimations for the accuracies of the different methods are made. With these and the written tool, the analysis is performed and the results are presented.

2.1 Theory of preliminary orbit determination

As introduction, some background about the theory of initial orbit determination is given. Aim of these methods is to get a first guess on the final orbit by a very reduced number of available measurements. All methods described below are implemented in the written tool `analyseMeasurements` and are used depending on the kind of measurement technique one uses. For a detailed description and a complete derivation of all methods, please refer to the works of [8], [9] and [10].

2.1.1 Gauss' method

The first method used determines an orbit from two position vectors in a given time interval and was established by Gauss himself. The procedure described here basically follows [10]. The approach is to find the semi latus rectum via the ratio of the sector and

the triangle, spanned by the orbit and the radius vectors at the given true anomalies (figure 2.1).

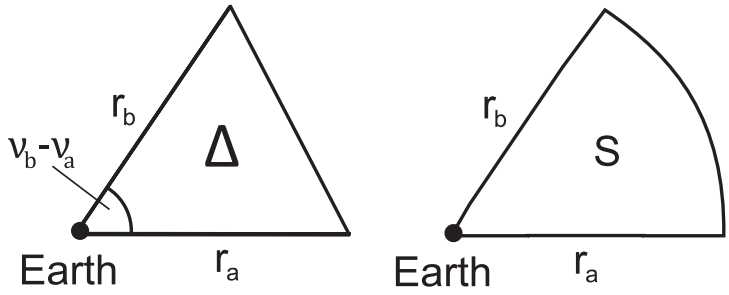

Figure 2.1: Sector and area.

Hereby, the area S of the section is described by the lengths of the two radius vectors r_a and r_b at the measurement times and the arc of the orbit. Referring to Kepler's second law, this area is proportional to the difference between the two times t_a and t_b

$$S = \frac{1}{2}\sqrt{GM_{\oplus}} \cdot \sqrt{a(1-e^2)} \cdot (t_b - t_a). \tag{2.1}$$

In here, a describes the semi major axis of the Kepler orbit and e its eccentricity. The area of the triangle is simply described by

$$\Delta = \frac{1}{2} r_a r_b \cdot \sin(\nu_b - \nu_a), \tag{2.2}$$

with ν_a and ν_b being the true anomalies at the given times. Building the ratio of these two areas, and substituting the semi latus rectum $p = a(1-e^2)$ one gets

$$\eta = \frac{S}{\Delta} = \frac{\sqrt{p} \cdot \tau}{r_a r_b \cdot \sin(\nu_b - \nu_a)}. \tag{2.3}$$

In here, τ is called the normalized time interval

$$\tau = \sqrt{GM_{\oplus}} \cdot (t_b - t_a). \tag{2.4}$$

From this basis, after several substitutions and replacements which are described in more details in [10] one finds the transcendental equation

$$\eta = 1 + \frac{m}{\eta^2} \cdot W\left(\frac{m}{\eta^2} - l\right), \tag{2.5}$$

with m and l being auxiliary variables

$$m = \frac{\tau^2}{\sqrt{2(r_a r_b + \vec{r_a} \cdot \vec{r_b})^3}}, \tag{2.6}$$

$$l = \frac{r_a + r_b}{2\sqrt{2(r_a r_b + \vec{r_a} \cdot \vec{r_b})}} - \frac{1}{2} \tag{2.7}$$

and W being a function defined by

$$W(w) = \frac{2g - \sin(2g)}{\sin^3(g)}, \text{with } g = 2\sin^{-1}\sqrt{w}. \tag{2.8}$$

With help of the secant procedure, one can now find the root of

$$f(x) = 1 - x + \frac{m}{x^2} \cdot W\left(\frac{m}{x^2} - l\right). \tag{2.9}$$

Appropriate starting values for solving $f(x)$ are given by the Hansen's approximation [11]. After calculating η with help of the described way, the semi latus rectum can be calculated with equation 2.10

$$p = \left(2\frac{\Delta\eta}{\tau}\right)^2. \tag{2.10}$$

For further calculations, one now uses the fact that the points $\vec{r_a}$ and $\vec{r_b}$ lie in one plane together with the center of Earth. So to derive the inclination i of this plane with respect to the equator of Earth and the right ascension of the ascending node Ω, one first needs the orthogonal unit vectors $\vec{e_a}$ and $\vec{e_b}$ on this plane

$$\vec{e_a} = \frac{\vec{r_a}}{|\vec{r_a}|}, \tag{2.11}$$

$$\vec{e_0} = \frac{\vec{r_0}}{|\vec{r_0}|}, \text{ where } \vec{r_0} = \vec{r_b} - (\vec{r_b} \cdot \vec{e_a})\vec{e_a}. \tag{2.12}$$

From now forming the cross product of these two vectors $\vec{W} = \vec{e_a} \times \vec{e_0}$ one yields the so called Gaussian vector, which is perpendicular to the orbital plane. With this vector, the inclination and the right ascension can be calculated directly

$$i = \arctan\left(\frac{\sqrt{W_x^2 + W_y^2}}{W_z}\right), \tag{2.13}$$

$$\Omega = \arctan\left(\frac{W_x}{-W_y}\right). \tag{2.14}$$

And furthermore the argument of latitude u_a as

$$u_a = \arctan\left(\frac{z_a}{-x_a W_y + y_a W_x}\right). \tag{2.15}$$

The eccentricity can be gotten from the conic section equation

$$\begin{aligned} e\cos(\nu_a) &= p/r_a - 1, \\ e\cos(\nu_b) &= p/r_b - 1. \end{aligned} \tag{2.16}$$

When accounting for

$$\cos(\nu_b) = \cos(\nu_a)\left(\frac{\vec{r_b}\cdot\vec{e_a}}{r_b}\right) - \sin(\nu_a)\left(\frac{r_0}{r_b}\right), \tag{2.17}$$

one gets two equations

$$e\,cos(\nu_a) = p/r_a - 1, \tag{2.18}$$

$$e\sin(\nu_a) = \left((p/r_a - 1)\left(\frac{\vec{r_b}\cdot\vec{e_a}}{r_b}\right) - (p/r_b - 1)\right) / \left(\frac{r_0}{r_b},\right) \tag{2.19}$$

which then can be solved for the eccentricity and the true anomaly at time t_a. The argument of perigee at that time can be calculated from the difference of latitude and true anomaly

$$\omega = u_a - \nu_a \tag{2.20}$$

and the semi major axis via

$$a = \frac{p}{1-e^2}. \tag{2.21}$$

The last missing Keplerian element, the mean anomaly, is obtained from Kepler's equation

$$M_a = E_a - e\cdot\sin(E_a). \tag{2.22}$$

For this, the eccentric anomaly E_a is calculated via

$$E_a = \arctan\left(\frac{\sqrt{1-e^2}\sin\nu_a}{\cos\nu_a + e}\right). \tag{2.23}$$

Now, all Keplerian orbital elements are determined from only two measurements and thus the orbit is complete. The described method has been implemented in the subroutine `getOrbitFromState()` of the tool `analyzeMeasurements`.

2.1.2 Gauss' angles only method

As the name suggests, Gauss' angles only method determines an orbit from angular measurements only. For this, three sets of measurements at different times are needed. Vallado [8] states this methods "works best for spacings between the measurements of less than about 60° and remarkably well for spacings less than 10°". The idea behind this approach is to find assumptions for the range to the object from the angular velocity.
First step is to calculate unit vectors from the measured angles and transform them into a usable coordinate frame. Furthermore, as a Keplerian orbit is assumed, these vectors lie in one plane, so one can express one of the vectors by a linear combination of the two other ones

$$c_1\vec{r_1} + c_2\vec{r_2} + c_3\vec{r_3} = \vec{0}. \tag{2.24}$$

From building the cross product of equation 2.24 with the first and third position vector, and furthermore assuming c_2 to be nonzero, one can apply f and g functions to form the position vectors from the second position and velocity

$$\vec{r_i} = f_i\vec{r_2} + g_i\vec{v_2},\ i = 1,3. \tag{2.25}$$

Using f and g functions is a classical formulation to use the fact that Keplerian orbits are always lying in one plane. Thus, every position and velocity vector can be expressed by a linear combination from other vectors (as already done in the beginning of this method). For a comprehensive overview of the theory and solution of the f and g functions, refer to pages 90 in [8] or [12].
In the next step, one assumes c_2 of equation 2.24 to be equal to -1, substitutes the values

with the f and g expressions and finds the coefficients to be

$$\begin{aligned} c_1 &= \frac{g_3}{f_1 g_3 - f_3 g_1}, \\ c_3 &= \frac{-g_1}{f_1 g_3 - f_3 g_1}. \end{aligned} \tag{2.26}$$

Due to the positions and velocities being unknown, one cannot determine values for f and g yet. So the next step is to use series expression for the functions. In here, the data times are defines as $\tau_i = t_i - t_2$ and the series coefficient u is defined as $u = \frac{\mu}{r_2^3}$. This yields for the coefficients

$$\begin{aligned} c_1 &\approx \frac{\tau_3}{\tau_3 - \tau_1} + \frac{u\tau_3((\tau_3 - \tau_1)^2 - \tau_3^2)}{6(\tau_3 - \tau_1)} = a_1 + a_{1u}u, \\ c_3 &\approx -\frac{\tau_1}{\tau_3 - \tau_1} - \frac{u\tau_1((\tau_3 - \tau_1)^2 - \tau_1^2)}{6(\tau_3 - \tau_1)} = a_3 + a_{3u}u. \end{aligned} \tag{2.27}$$

Now approximate expressions for the coefficients have been resolved. The problem is still that the positions themselves are missing. These can be expressed as the position of the site (which is usually known) plus the slant range from the site to the object on orbit ρ. Substituting this into equation 2.24 leads to

$$c_1(\vec{\rho}_1 + \vec{r}_{site_1}) + c_2(\vec{\rho}_2 + \vec{r}_{site_2}) + c_3(\vec{\rho}_3 + \vec{r}_{site_3}) = \vec{0}. \tag{2.28}$$

Furthermore, from the observations made, here expressed as topocentric declination and right ascension, one can determine line-of-sight unit vectors, pointing into the directions one is looking. Note that, unless for stellar observations, the difference between equatorial declination/right ascension and topocentric values can be enormous due to the low orbit height.

$$\widehat{L}_i = \begin{bmatrix} \cos(\delta_{ti})\cos(\alpha_{ti}) \\ \cos(\delta_{ti})\sin(\alpha_{ti}) \\ \sin(\delta_{ti}) \end{bmatrix}, i = 1,3. \tag{2.29}$$

With this line of sight matrix one can express the slant ranges from the site vectors and the line of site vectors together with the coefficients

$$\begin{bmatrix} c_1\rho_1 \\ c_2\rho_2 \\ c_3\rho_3 \end{bmatrix} = \mathbf{L}^{-1} \begin{bmatrix} \vec{r}_{site_1} \\ \vec{r}_{site_2} \\ \vec{r}_{site_3} \end{bmatrix}^{\mathbf{T}} \begin{bmatrix} -c_1 \\ -c_2 \\ -c_3 \end{bmatrix}. \tag{2.30}$$

Note that $\mathbf{L^{-1}}$ is the inverse of the line of sight matrix, which is described by $\mathbf{L} = \left[\widehat{\mathbf{L_1}}|\widehat{\mathbf{L_2}}|\widehat{\mathbf{L_3}}\right]$. From this equation, the slant ranges can be evaluated. The middle slant range thereby is expressed in equation 2.31. For terms of better overview, the $\mathbf{L^{-1}r_{site}}$ terms are expressed as matrix $\mathbf{M}$.

$$\rho_2 = M_{21}a_1 - M_{22} + M_{23}a_3 + (M_{21}a_{1u} + M_{23}a_{3u})u = d_1 + d_{2u}. \tag{2.31}$$

By substitution equation 2.31 into this expression

$$r = \sqrt{\rho^2 + 2\rho\widehat{L}\vec{r}_{site} + r_{site}^2} \tag{2.32}$$

for the satellite's distance, one gets an eighth order equation for r_2

$$r_2^8 - (d_1^2 + 2Cd_1 + r_{site}^2)r_6^2 - 2\mu(Cd_2 + d2d_1d_2)r_2^3 - \mu^2 d_2^2 = 0. \tag{2.33}$$

Note that the coefficients d_1, d_2 and C are substitutions for a better overview. d_1 and d_2 account for the time differences and the viewing direction from the site. C is the product of line of site and position of the sensor at the 2nd measurement: $C = \widehat{L_2} \cdot \vec{r}_{site_2}$. From this equation, one has to find the largest real positive root. As root solver, a Bairstow solver has been chosen. This method basically uses the Newton's method to adjust u and v in the standard quadratic polynomial $x^2 + ux + v$ until they are also roots of the to be solved polynomial. Following, the polynomial is divided by the newly found quadratic and the process is iterated until are roots are found [13]. With this, one now has a first solution for r_2 and can update the f and g series coefficient u. With the help of u one is able to furthermore get the coefficients c_i and with these find all three position vectors. So basically, one has three measurements of angles and ranges. At this step the later described Gibbs (2.1.3) or Herrick-Gibbs (2.1.4, depending on the spacing between the input vectors) are used to find the middle velocity $\vec{v}_2$. As the first guess, as calculated from the method described above, one iterates to refine the slant ranges. Now, an initial state vector (from $\vec{r}_2$ and $\vec{v}_2$) has been found to determine the orbital parameter, this time the real f and g functions can be used instead of their series expansion (note: in the computer routine, this is only done for the last iteration step for a faster processing; in the prior steps a series expansion of the f and g functions is used):

$$\begin{aligned} f_i &= 1 - \left(\frac{r_i}{p}\right)(1 - \cos(\Delta\nu_i)),\ i = 1,3, \\ g_i &= \frac{r_i r_2 \sin(\Delta\nu_i)}{\sqrt{\mu p}},\ i = 1,3. \end{aligned} \tag{2.34}$$

In here, p is the orbital parameter and $\Delta\nu$ describes the difference between the true anomalies during the measurements, thus the spacing between the position vectors. With these one again determines the coefficients c_i and from these the slant ranges can be determined. The iteration process is preceded until the slant ranges converge.

2.1.3 Gibbs Method

In difference to the prior described Gauss' angles only method, this method uses three sets of measurements of angles, ranges and times. The beginning of this method is actually very similar to the Gauss' angles only method. To find a solution, the input vectors have to meet following assumptions:
The vectors have to be

1. nonzero
2. coplanar
3. time-sequential.

In here it is of high importance to keep the time sequence. This is due to several cross products calculated during the calculation that depend on the correct order. For the vectors to be coplanar a certain tolerance has been implemented into the actual program. This is due to the fact that most measurements are not perfect, so deviations in the inclinations of the measured position vectors are quite normal. Furthermore, as the method is based on vector analysis, the measurements should not be too close together, because else numerical errors would appear. Vallado [8] recommends using the Gibbs method down to minimum spacing of the measurements of about 5°.
The basic aim of the procedure is to find the middle velocity vector which is common between each of the given vectors.
Due to the fact that all vectors are coplanar one vector is a linear combination of the two other ones. By this, one can find coefficients c to describe this linear combination

$$c_1\vec{r_1} + c_2\vec{r_2} + c_3\vec{r_3} = \vec{0}. \tag{2.35}$$

Now one has to isolate the coefficients to be able to determine them. The complete process for this can be found in [8], in here, only the most important steps are outlined. After transformation, one can express the cross product of equation 2.35 with $\vec{r_3}$ with the constant c_2 only

$$c_2\vec{r_2} \times \vec{r_3}(p - r_1) + c_2\vec{r_3} \times \vec{r_1}(p - r_2) + c_2\vec{r_1} \times \vec{r_2}(p - r_3) = \vec{0}. \tag{2.36}$$

Dividing this by c_2 leads to

$$p(\vec{r_1} \times \vec{r_2} + \vec{r_2} \times \vec{r_3} + \vec{r_3} \times \vec{r_1}) = r_1(\vec{r_2} \times \vec{r_3}) + r_2(\vec{r_3} \times \vec{r_1}) + r_3(\vec{r_1} \times \vec{r_2}). \tag{2.37}$$

By defining the right part of the equation as $\vec{N}$ and the vector part of the left side of the equation as $\vec{D}$ one yields following equation

$$\vec{N} = p\vec{D}. \tag{2.38}$$

Geometrically, $\vec{D}$ is a vector perpendicular to the plane spanned by the three input vectors, if those are coplanar, $\vec{N}$ also is perpendicular to this plane. In here, a simple check can be applied, by testing if

$$\vec{N} \cdot \vec{D} = ND. \tag{2.39}$$

If those two vectors do not point in the same direction, the calculation process won't work. The following process uses the perifocal coordinate system. In this system, $\widehat{P}$ is the vector pointing towards the periapsis, and $\widehat{W}$ is the vector pointed in the direction of the angular momentum (which is orthogonal to the orbit plane). With $\vec{N}$ also pointing in the direction of the angular momentum, one can write

$$\widehat{P} = \frac{\vec{e}}{|\vec{e}|} \qquad \widehat{W} = \frac{\vec{N}}{|\vec{N}|}. \tag{2.40}$$

In here, $\vec{e}$ is the eccentricity vector. With the perifocal system being orthogonal, the third vector can be determined via

$$\widehat{Q} = \widehat{W} \times \widehat{P} = \frac{\vec{N} \times \vec{e}}{|\vec{N}||\vec{e}|}. \tag{2.41}$$

After again some more transformations, one yields equation 2.42

$$Ne\widehat{Q} = p\left[(r_2 - r_3)\vec{r_1} + (r_3 - r_1)\vec{r_2} + (r_1 - r_2)\vec{r_3}\right] = p\vec{S}. \tag{2.42}$$

In here it is important that $\widehat{Q}$ and $\vec{S}$ have to point into the same direction. From these values, one can get the eccentricity

$$e = \frac{S}{D}, \tag{2.43}$$

so that basically the orbit can be described, as the eccentricity e and the semiparameter (semi latus rectum) p are determined. But the aim of the computational process is to

directly determine the middle velocity vector from the vectors $\vec{D}$, $\vec{S}$ and $\vec{N}$.
Beginning with the basic equation for the velocity vector at point 2

$$\dot{\vec{r_2}} \times \vec{h} = \mu \left(\frac{\vec{r_2}}{r_2} + \vec{e} \right) \tag{2.44}$$

and with the help of $\vec{h} = h\widehat{W}$ (the specific angular momentum) and $\vec{e} = e\widehat{P}$ one yields for v_2

$$\vec{v_2} = \frac{\mu}{h} \left(\frac{\widehat{W} \times \vec{r_2}}{r_2} + e\widehat{W} \times \widehat{P} \right) = \frac{\mu}{h}. \left(\frac{\widehat{W} \times \vec{r_2}}{r_2} + e\widehat{Q} \right) \tag{2.45}$$

From this equation, it is yet not possible to get v_2 directly. First, some further substitutions have to be performed:

$$h = \sqrt{\frac{N\mu}{D}}, \tag{2.46}$$

$$\vec{B} = \vec{D} \times \vec{r_2}, \tag{2.47}$$

and

$$L_g = \sqrt{\frac{\mu}{ND}}. \tag{2.48}$$

With these, one finally can express $\vec{v_2}$ as

$$\vec{v_2} = \frac{L_g}{r_2}\vec{B} + L_g\vec{S}. \tag{2.49}$$

With this equation, the Gibbs method is as its final. As this method is best for angular spacing between the measurement vectors larger than at least 5°, for angular spacing below these five degrees, the Herrick-Gibbs method is used.

2.1.4 Herrick-Gibbs Method

With many measurements there is the problem that the spacing between them is too low. For this, the Herrick-Gibbs method can be used. This is a variation of the prior described Gibbs method, which tries to find the middle velocity from three given sequential position vectors and their observation times. The method is based on developing a Taylor series expansion around the middle position. Due to this approximate series expansion, this method is more limited in application, and does not give reasonable

results for a vector spacing over 10°. The description of this method once more follows the one given in [8].
The first step is the Taylor series expansion of the two position vectors r_1 and r_3 around the middle time t_2

$$\vec{r_1} = \vec{r_2} + \dot{\vec{r}_2}\Delta t_{12} + \frac{\ddot{\vec{r}_2}\Delta t_{12}^2}{2!} + \frac{\dddot{\vec{r}_2}\Delta t_{12}^3}{3!} + \dots , \tag{2.50}$$

$$\vec{r_3} = \vec{r_2} + \dot{\vec{r}_2}\Delta t_{32} + \frac{\ddot{\vec{r}_2}\Delta t_{32}^2}{2!} + \frac{\dddot{\vec{r}_2}\Delta t_{32}^3}{3!} + \dots . \tag{2.51}$$

In order to find the middle velocity vector, one first ignores all terms higher than fourth order. Next step is to find expressions for the second to fourth order. Multiplying equation 2.50 by $-\Delta t_{32}^2$ and adding it to equation 2.51 multiplied by Δt_{12}^2 gives

$$\begin{aligned} -\vec{r_1}\Delta t_{32}^2 + \vec{r_3}\Delta t_{12}^2 = \vec{r_2}(-\Delta t_{32}^2 + \Delta t_{12}^2) + \dot{\vec{r}_2}(-\Delta t_{32}^2\Delta t_{12} + \Delta t_{12}^2\Delta t_{32}) \\ + \frac{\dddot{\vec{r}}}{6}(-\Delta t_{32}^2\Delta t_{12}^3 + \Delta t_{12}^2\Delta t_{32}^3) + \frac{\ddddot{\vec{r}_2}}{24}(-\Delta t_{32}^2\Delta t_{12}^4 + \Delta t_{12}^2\Delta t_{32}^4). \end{aligned} \tag{2.52}$$

After some more simplifications one gets an impression for the middle velocity vector

$$\begin{aligned} \dot{\vec{r}_2}(\Delta t_{12}\Delta t_{32}\Delta t_{31}) = \vec{r_1}\Delta t_{32}^2 + \vec{r_2}(-\Delta t_{32}^2 + \Delta t_{12}^2) - \vec{r_3}\Delta t_{12}^2 \\ + \frac{\dddot{\vec{r}_2}}{6}(\Delta t_{12}^2\Delta t_{32}^2\Delta t_{31}) + \frac{\ddddot{\vec{r}_2}}{24}(\Delta t_{12}^2\Delta t_{32}^2\Delta t_{31}\left[\Delta t_{32} + \Delta t_{12}\right]). \end{aligned} \tag{2.53}$$

Now the next step is to find expressions for the third and fourth derivatives. This is done by differentiating equations 2.50 and 2.51 twice to provide a starting point. After some further reductions and transformations one yields

$$\ddddot{\vec{r}_2} = \frac{2}{\Delta t_{12}\Delta t_{32}\Delta t_{31}}\left(\ddot{\vec{r}_1}\Delta t_{32} + \ddot{\vec{r}_2}\Delta t_{31} + \ddot{\vec{r}_3}\Delta t_{12}\right). \tag{2.54}$$

for the forth derivative. Similar to this one obtains the third derivative which leads to

$$\dddot{\vec{r}_2} = \frac{1}{\Delta t_{12}\Delta t_{32}\Delta t_{31}}\left(-\ddot{\vec{r}_1}\Delta t_{32}^2 + \ddot{\vec{r}_2}\left(\Delta t_{31}\left(\Delta t_{32} + \Delta t_{12}\right)\right) + \ddot{\vec{r}_3}\Delta t_{12}^2\right). \tag{2.55}$$

Substituting these into 2.53 and dividing by $(\Delta t_{12}\Delta t_{32}\Delta t_{31})$ gives after some simplifica-

tions

$$\dot{\vec{r}}_2 = \frac{\vec{r}_1\Delta t_{32}}{\Delta t_{12}\Delta t_{31}} - \frac{\vec{r}_2(\Delta t_{32}+\Delta t_{12})}{\Delta t_{12}\Delta t_{32}} - \frac{\vec{r}_3\Delta t_{12}}{\Delta t_{32}\Delta t_{31}} + \ddot{\vec{r}}_1\left(\frac{\Delta t_{32}\left(2\Delta t_{32}-\Delta t_{32}-\Delta t_{12}\right)}{12\Delta t_{31}}\right) + \ddot{\vec{r}}_2\left(\frac{-\Delta t_{31}\left(\Delta t_{32}+\Delta t_{12}\right)}{12\Delta t_{31}}\right) + \ddot{\vec{r}}_3\left(\Delta t_{12}\frac{-2\Delta t_{12}+\Delta t_{32}+\Delta t_{12}}{12\Delta t_{31}}\right). \tag{2.56}$$

Remembering that two body motion has been applied one can eliminate the acceleration with

$$\ddot{\vec{r}} = -\frac{\mu}{r^3}\vec{r}. \tag{2.57}$$

Doing this and further simplifying the equation given above, one gets a final expression for the middle velocity as

$$\vec{v}_2 = -\Delta t_{32}\left(\frac{1}{\Delta t_{21}\Delta t_{31}} + \frac{\mu}{12r_1^3}\right)\vec{r}_1 + (\Delta t_{32}-\Delta t_{21})\left(\frac{1}{\Delta t_{21}\Delta t_{32}} + \frac{\mu}{12r_2^3}\right)\vec{r}_2 + \Delta t_{21}\left(\frac{1}{\Delta t_{32}\Delta t_{31}} + \frac{\mu}{12r_3^3}\right)\vec{r}_3. \tag{2.58}$$

With this expression, the middle velocity is found, and together with the prior determined position (either directly from measurements or with help of Gauss' angles only method), one now has a complete state vector for the second position.
In the tool `analyseMeasurement`, the decision between the Gibbs or Herrick-Gibbs method happens automatically, depending on the spacing between the measurements.

2.2 Orbit propagation

The tool `analyseMeasurements` contains a small orbit propagator. An overview of the basic structure of this propagator is given in figure 2.2 below.

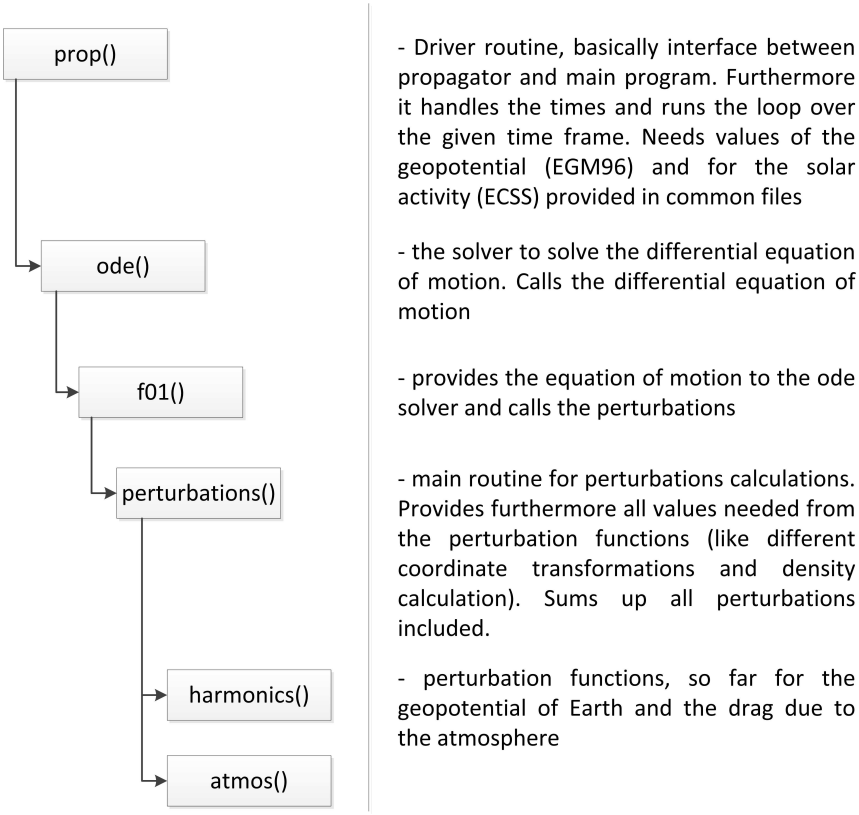

Figure 2.2: Basic structure of the propagator.

For orbit propagation, in general three basic methods do exist: One can use analytical equations describing the perturbations, a numerical integration of the equation of motion or so called semi-numerical methods, which means that one uses analytical equations for a certain time step and afterwards restarts the propagation with the newly gained values. All methods have their pros and contras. In general, numerical methods are considered to be most accurate, but need long computation times, analytical methods are less accurate but very fast in processing. The semi-analytical methods combine both advantages in being nearly as fast as pure analytical methods, but, especially over longer propagation times, much more accurate. The problem with both the analytical approaches is that they often do not cover short-periodical deviations of the orbit. As this propagator is to be used mostly for short term propagations (at maximum several days), short periodical perturbations are essential, why the numerical propagation method was chosen. Furthermore, by this the advantage of the higher accuracy can be used.

2.2.1 Numerical integration of the equation of motion

The aim of any orbit propagator is to solve the disturbed equation of motion for a two body problem [14]

$$\ddot{\vec{r}} = \frac{\mu}{r^3} \cdot \vec{r} + \vec{f}_{pert}. \tag{2.59}$$

The chosen approach at this point is the direct numerical integration equation 2.59. For this, the equation is expressed in Cartesian coordinates

$$\begin{bmatrix} \ddot{x} \\ \ddot{y} \\ \ddot{z} \end{bmatrix} = \frac{\mu}{r^3} \begin{bmatrix} x \\ y \\ z \end{bmatrix} + \frac{1}{m} \begin{bmatrix} f_x(\underline{r},\underline{\dot{r}}) \\ f_y(\underline{r},\underline{\dot{r}}) \\ f_z(\underline{r},\underline{\dot{r}}) \end{bmatrix}. \tag{2.60}$$

As the used ODE-solver, a Shampine-Gordon solver [15], needs a set of first order differential equations, the equation has to be transferred in such a system by substituting

$$\begin{aligned} [y_i] &= [x\ y\ z]^T, \text{ for } i = 1,3 \\ [y_i] &= [\dot{x}\ \dot{y}\ \dot{z}]^T, \text{ for } i = 4,6. \end{aligned} \tag{2.61}$$

With this, one can set up a system of six first-order differential equation that can be solved

$$\begin{bmatrix} \dot{y_1} \\ \dot{y_2} \\ \dot{y_3} \\ \dot{y_4} \\ \dot{y_5} \\ \dot{y_6} \end{bmatrix} = \begin{bmatrix} y_4 \\ y_5 \\ y_6 \\ c \cdot y_1 \\ c \cdot y_2 \\ c \cdot y_3 \end{bmatrix} + \begin{bmatrix} 0 \\ 0 \\ 0 \\ B_{x,G} + B_{x,ATM} \\ B_{y,G} + B_{y,ATM} \\ B_{z,G} + B_{z,ATM} \end{bmatrix}. \tag{2.62}$$

with $c = \frac{-\mu}{r^3}$, $B_{i,G}$ being the perturbations induced by Earth's geopotential and $B_{i,ATM}$ the perturbations due to the atmospheric drag.

2.2.2 Perturbations

At this point the perturbations considered shall be described. As this tool will be used for preliminary and short term analyses, it was decided to only use the main acting perturbations in low-earth orbits. These are by far the Earth's geopotential and, depending on the actual solar activity, for orbits up to heights of about 700km the atmospheric drag (referring to [10], page 55). Thus, only those two shall be described at this

point.

Geopotential

The geopotential is the driving force acting on an object in orbit, as it keeps it on track. The perturbing forces induced by the gravitational field of any spherical central body could easily be described using the spherical potential function U_0

$$U_0(r) = \frac{\mu}{r}. \tag{2.63}$$

But as Earth is not a sphere, but rather some kind of ellipsoid, the potential is dependent on the position of Earth, thus

$$U = U(r, \beta, \lambda). \tag{2.64}$$

A rather complex development which is very well documented in the literature, leads to a description of the potential function for the central-body effects, separated into zonal and tesseral parts

$$\begin{aligned} U = \frac{\mu}{r}\Bigg[1 - \sum_{l=2}^{\infty} J_l \left(\frac{R_\oplus}{r}\right)^l P_l\left[\sin\left(\phi_{gc_{sat}}\right)\right], \\ + \sum_{l=2}^{\infty}\sum_{m=1}^{l}\left(\frac{R_\oplus}{r}\right)^l P_{l,m}\left[\sin\left(\phi_{gc_{sat}}\right)\right]\left[C_{l,m}\cos\left(m\lambda_{sat}\right) + S_{l,m}\sin\left(m\lambda_{sat}\right)\right]\Bigg]. \end{aligned} \tag{2.65}$$

In here, $P_{l,m}$ are associated Legendre functions with the general form of

$$P_{l,m}[\gamma] = \left(1-\gamma^2\right)^{m/2}\frac{d^m}{d\gamma^m}P_l[\gamma] \tag{2.66}$$

and C and S being the zonal and tesseral gravitational coefficients, which are determined empirically, and $J_l = -C_{l,0}$. To obtain the accelerations on the orbiting object due to the geopotential, the gradient (or the partial derivatives) of the potential function is needed. Furthermore note, while before the potential function was written in spherical coordinates, it is now changed to Cartesian coordinates to allow an easier computational processing.

$$\vec{a} = \frac{\partial U}{\partial r}\left(\frac{\partial r}{\partial \vec{r}}\right)^T + \frac{\partial U}{\partial \phi_{gc_{sat}}}\left(\frac{\partial \phi_{gc_{sat}}}{\partial \vec{r}}\right)^T + \frac{\partial U}{\partial \lambda_{sat}}\left(\frac{\partial \lambda_{sat}}{\partial \vec{r}}\right)^T. \tag{2.67}$$

Finally, equation 2.67 can be split up into individual parts, giving the accelerations in all directions of an I,J,K - frame

$$
\begin{aligned}
a_I &= \left[\frac{1}{r}\frac{\partial U}{\partial r} - \frac{r_K}{r^2\sqrt{r_I^2+r_J^2}}\frac{\partial U}{\partial \phi_{gc_{sat}}}\right] r_I - \left[\frac{1}{r_I^2+r_J^2}\frac{\partial U}{\partial \lambda_{sat}}\right] r_J, \\
a_J &= \left[\frac{1}{r}\frac{\partial U}{\partial r} - \frac{r_K}{r^2\sqrt{r_I^2+r_J^2}}\frac{\partial U}{\partial \phi_{gc_{sat}}}\right] r_J + \left[\frac{1}{r_I^2+r_J^2}\frac{\partial U}{\partial \lambda_{sat}}\right] r_I, \\
a_K &= \frac{1}{r}\frac{\partial U}{\partial r} r_K + \frac{\sqrt{r_I^2+r_J^2}}{r^2}\frac{\partial U}{\partial \phi_{gc_{sat}}}.
\end{aligned}
\tag{2.68}
$$

A comprehensive deduction of these equations is described in [8], a short overview is shown in [12].

Atmospheric drag

On every object that is passing through the atmosphere, the friction between the satellite and the air induces a drag that depends on the current atmospheric density and the geometry of the satellite. Referring to [9], the atmospheric drag can be determined via

$$D = \frac{1}{2}\cdot C_D \cdot \rho \cdot A \cdot V_r^3, \tag{2.69}$$

with D being the drag, C_D the drag coefficient, ρ the density, A the object's effective surface and V_r the relative speed between the atmosphere and the satellite. The relative speed is determined with equation 2.70

$$\underline{V_r} = \underline{\dot{r}} + \underline{r}x\omega_{ATM} = \begin{bmatrix} \dot{x} + \omega_{ATM}\cdot y \\ \dot{y} - \omega_{ATM}\cdot x \\ \dot{z} \end{bmatrix}, \tag{2.70}$$

with ω_{ATM} being the rotational velocity of the atmosphere. From this relative speed the unit vector for the relative velocity is formed

$$\vec{V_u} = \frac{\vec{V_r}}{|V_r|}, \text{ with } |\vec{V_r}| = \sqrt{V_{rx}^2 + V_{ry}^2 + V_{rz}^2}. \tag{2.71}$$

From the unit vector $\vec{V_u}$ and the drag force D and the mass of the object on orbit one can now determine the acceleration acting on the satellite

$$B_{ATM} = -D \cdot \frac{\vec{V_u}}{m} \tag{2.72}$$

or vectorized for the single components as

$$\begin{bmatrix} B_{ATM,x} \\ B_{ATM,y} \\ B_{ATM,z} \end{bmatrix} = -\rho \cdot B_c \cdot \begin{bmatrix} V_{r,x} \cdot |V_r| \\ V_{r,y} \cdot |V_r| \\ V_{r,z} \cdot |V_r| \end{bmatrix}, \tag{2.73}$$

where $B_c = \frac{C_D}{2} \cdot \frac{A}{m}$ is the so called ballistic coefficient.
The current density of the atmosphere ρ is determined with the JB-06 (Jacchia-Bowmann 2006) atmospheric density model [16]. As this model is highly dependent on solar and magnetic activity, one furthermore needs to provide inputs for these values. In here, values from the ECSS standards are provided, the solar activity can be chosen by the user [17]. As the orbital propagator is only meant for short time propagations, the values for solar and magnetic activity are kept constant during the propagation.

2.3 Analyzing the accuracies in regard to orbit determination

To estimate the preliminary orbit determination capabilities of the different systems, a tool has been written to perform the needed calculations. At this point, first an overview over the tool shall be given. For the overall process, the user has to run two programs: The first one to simulate the sightings of a given object, which is described in paragraph 2.3.1. After finding a suitable sighting, this one can be analyzed with the tool `anaylseMeasurements`, described in 2.3.2.

2.3.1 Simulating sightings

Before one is able to determine orbit measurements, first measurements to work with are needed. For this purpose the tool `getSightings` has been written. In here, one enters a TLE data string, valid for the epoch to evaluate, the site's position and the epoch (usually one should only look at a single day or some days, for more accurate coordinate transformation). As output one gets a file containing all possible sightings (azimuth, elevation and range, as well as ECI(TEME) coordinates) of the object during the defined epoch. A sighting is assumed possible as long as the elevation angle is positive.
The tool itself is based on a tool provided by David A. Vallado in [8]. This tool calculates the ECI(TEME) positions of TLE objects at wanted times using the SGP4/SDP4 orbit propagators. This program has been modified and complimented with coordinate transformations to be able to give the outputs in the local horizontal coordinate system. This basically works by rotating the ECI(TEME) coordinate system into the ECEF(ITRF) system (which is basically identical to the WGS-84)

$$\vec{v}_{ITRF} = \mathrm{ROT}_z\left(\Theta_{GMST,1982}\right) \cdot \mathrm{ROT}_x\left(-y_p\right) \cdot \mathrm{ROT}_y\left(-x_p\right), \tag{2.74}$$

with Θ_{GMST} being the Greenwich mean sidereal time, and x_p and y_p the displacements of the pole. After this rotation, the current position of the state has to be expressed in ECEF(ITRF/WGS-84) Cartesian coordinates, and the slant range (or line of sight) between the object and the station has to be calculated

$$\rho_{ECEF} = \vec{v}_{Object,ECEF} - \vec{v}_{Station,ECEF}. \tag{2.75}$$

Now one has the general direction from the station to the object, but given in reference to the Greenwich meridian. Thus, now a change to a local system, here referenced to as SEZ system, which has the origin at the observer, with its axes pointing to the South,

East and Zenith. For this, two further rotations are needed, one around longitude, to get the offset to the Greenwich meridian, and a second one around the latitude, to account for the offset to the equator

$$\overrightarrow{rho}_{SEZ} = \mathrm{ROT}_3(\lambda) \cdot \mathrm{ROT}_2\left(\frac{\pi}{2} - \phi\right) \cdot \overrightarrow{rho}_{ECEF}. \tag{2.76}$$

From this, the range is gotten by the magnitude of the slant range, azimuth and elevation by simple trigonometry.

$$\begin{aligned} \rho &= \sqrt{\rho_{SEZ,1}^2 + \rho_{SEZ,2}^2 + \rho_{SEZ,3}^2}, \\ h &= \sin\left(\frac{\rho_{SEZ,3}}{\rho}\right), \\ A &= \mathrm{atan2}\left(\frac{\rho_{SEZ,1}}{\rho_{SEZ,2}}\right) + \frac{\pi}{2}. \end{aligned} \tag{2.77}$$

Note that the elevation has a range of -90° ... 90° (whereas negative values denote that the satellite is below the local horizon), the azimuth goes from 0° ... 360°. The addition of $\frac{\pi}{2}$ accounts for measuring the azimuth from North positive to the East.
A definition of the used coordinate systems is given in the appendix in section B.
Figure 2.3, gives an overview of the program.

To proof the accuracy of the written tool, a comparison with data from the measurement campaign in Graz [6] has been performed. The data from Graz was used as prediction for laser ranging experiments performed in cooperation with the Institute of Technical Physics at the DLR in Stuttgart. The test has been performed on January the 25th, with TLE-object 28222 (CZ-C2 rocket body). As result, the differences in the angular coordinates are shown in figure 2.4. The remaining differences lie all in the 10^{-3° range. This is acceptable, as it is unknown, which TLE epoch has been used for the reference values, as well as no details about their accuracy referring to coordinate transformation and state vector determination is available. Furthermore, the accuracy of the site's position is unknown.

2.3.2 Analyzing Measurements

The aim of the tool `analyseMeasurements` is to determine the impact of deviations in the measurement with regard to the true orbit position. At this point, a short description of the general work of this tool shall be given. For a first impression of the

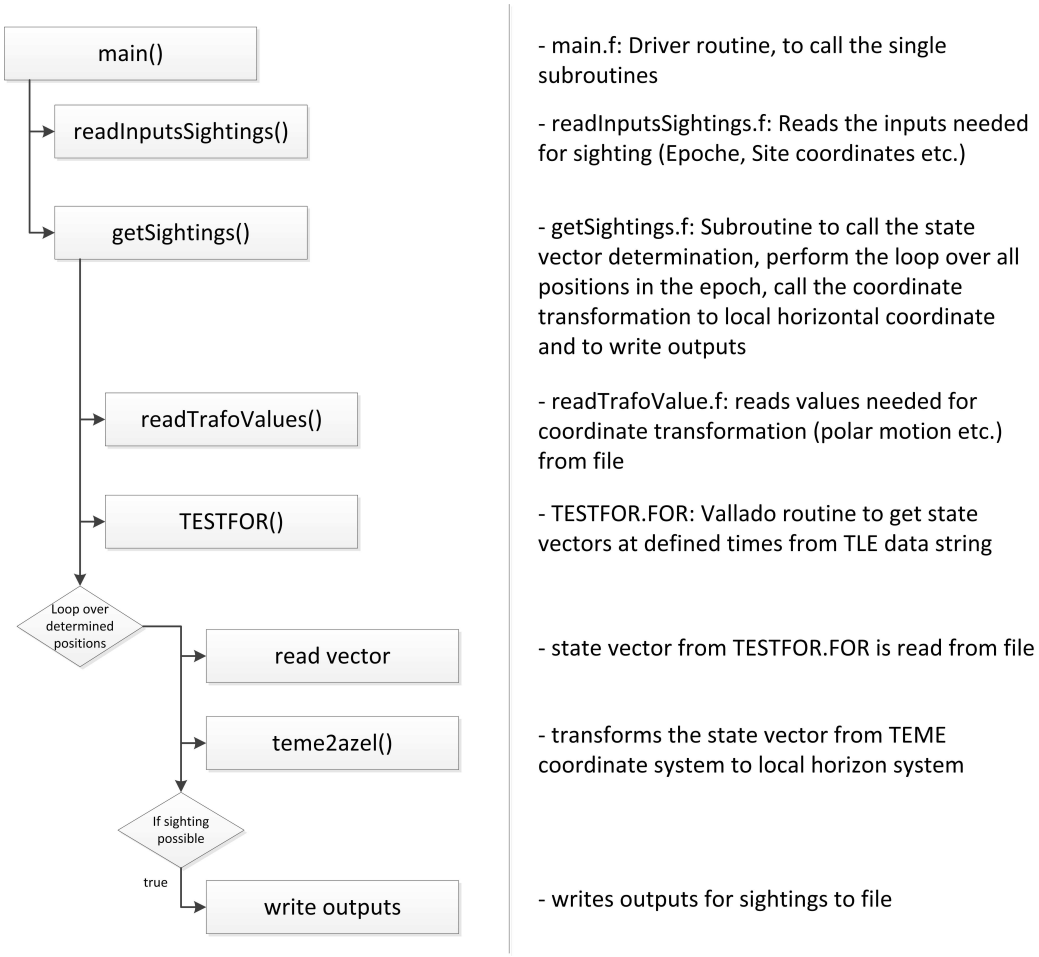

Figure 2.3: Flow chart over simulation of sightings.

tool, figure 2.5 gives an overview of its sequence. Note that this chart is by far not complete and is only meant to explain the structure.
Following, the main stages of the program will be described.

Driver routine

The main routine, saved in `analyseMeasurements.f`, is the driver of the program that takes care of handling all input and output, necessary data reading, running the loops over the deviations and calling the subroutines for orbit determination and propagation.
At first, the inputs are read. These are saved in the file `input.inp` in the folder `/input`. This is done in an external subroutine. To get an overview of the possible inputs, the input file is stated below.

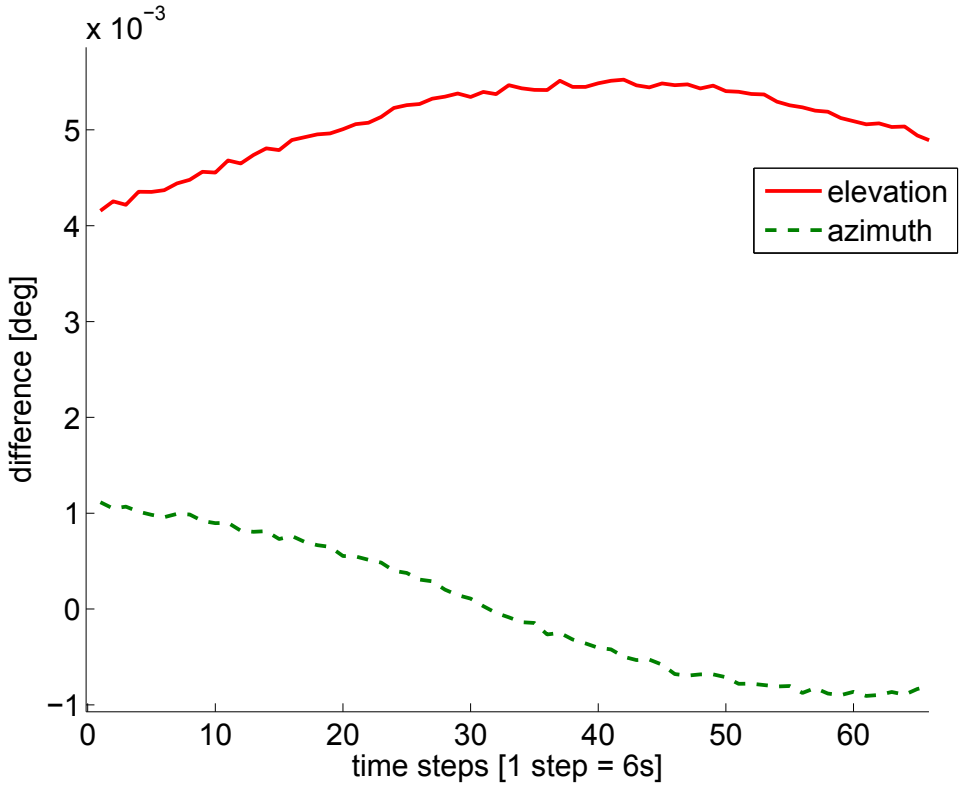

Figure 2.4: Difference in sighting calculations between own data and data used in Graz as reference.

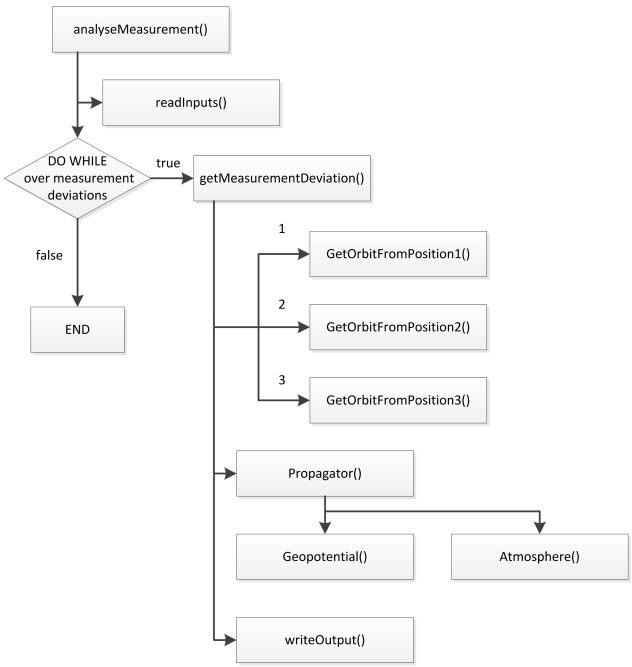

Figure 2.5: Overview: `analyseMeasurements`.

```
#############################################################################
#                                                                           #
#                              INPUT-FILE                                   #
#                                                                           #
#############################################################################
# Define in here all inputs needed for the measurement analysis             #
# Please keep all the inputs in the lines they were. Do not delete any#
# of the #!!!! Further note: All DOUBLE PRECISION values have to be   #
# entered in Fortran style, using the xx.xxd0 Format!!!! THE d0 at the#
# end is more than highly important! Else it comes to data type       #
# confusions and results WILL be wrong! (the d indicates double       #
# precision values, and is substituter for e in single precision value#
# s: Example: Single: 1.0e0, double: 1.0d0,normal: 1x10^0             #
# Measurement data. Note, the orbit determined for this measurement   #
# counts as the correct orbit. Deviations are defined below           #
# Choose, which method to be used for orbit determination:            #
# 1 = Radar/Laser with Gauss (two measurements, Range and Angles)     #
# 2 = Radar/Laser with Gibbs/HerrickGibbs (three measurements, Range  #
#     and angles)                                                     #
# 3 = Passive Optical, with Gauss (Three measurements, angles only)   #
3 intMethodeChooser
# Measurement 1
320.71240d0      Azimuth, DP, [°]
 1.188084d0      Elevation, DP, [°]
2690649.659796d0 Range, DP, [m]
2012             year, INT, [yyyy]
06               month, INT, [mm]
15               day, INT, [dd]
23               hour, INT, [hh]
29               minute, INT, [mm]
06               second, INT, [ss]
# Measurement 2                                                           #
326.70981473d0   Azimuth, DP, [°]
 34.93743401d0   Elevation, DP, [°]
958984.81859d0   Range, DP, [m]
2012             year, INT, [yyyy]
06               month, INT, [mm]
15               day, INT, [dd]
23               hour, INT, [hh]
33               minute, INT, [mm]d
36               second, INT, [ss]
# Measurement 3: Is ignored, if not needed for analysis!                  #
123.59557466d0   Azimuth, DP, [°]
 60.4062769d0    Elevation, DP, [°]
670673.19185d0   Range, DP, [m]
2012             year, INT, [yyyy]
06               month, INT, [mm]
15               day, INT, [dd]
23               hour, INT, [hh]
36               minute, INT, [mm]d
06               second, INT, [ss]
# Ground Station data                                                     #
351.0d0          geodetic height of sensor, WGS84, DP, [m]
48.7834d0        geodetic latitude of sensor, WGS84, DP, [°]
9.1975d0         geodetic longitude of sensor, WGS84, DP, [°]
# Analysis data !!! NOTE THE FLAGS BELOW THIS!!!                          #
# In case of three measurements being used, only the first and the        #
# will be deviated! This is for avoiding too complex outputs!             #
 0.0d0           Deviation for Range (+/-), DP, [m]
 0.0d0           Deviation step size for Range (+/-), DP, [m]
0.00026d0        Deviation for Elevation (+/-), DP, [RAD]
0.00002d0        Step size for Elevation analysis, DP, [RAD]
0.00026d0        Deviation for Azimuth (+/-), DP, [RAD]
0.00002d0        Step size for Azimuth analysis, DP, [RAD]
0                Flag for Range One Deviation [-]
0                Flag for range Two Deviation [-]
1                Flag for Azimuth One Deviation [-]
0                Flag for Azimuth Two Deviation [-]
0                Flag for Elevation One Deviation [-]
0                Flag for Elevation Two Deviation [-]
# Propagation inputs:
10.d0            propagation duration [s]
2.d0             propagation time step [s]
1                flag for using the atmosphere (set 1 to use it)
medium           medium for the solar activity ('low','medium','shortHigh','longHigh')
40               size of gravity field [0-70]
1.d-10           relative tolerance of ode solver [-]
1.d-10           absolute tolerance of ode solver [-]
300.0d0          mass of objects [kg]
0.7854d0         effective surface of object [m**2]
2.2d0            cd of object [-]
# coordinate transformation data:
34.0d0           dpDeltaTai # NOTE: It is 35 from July 2012!
#############################################################################
#                                                                           #
#                          END OF INPUTS                                    #
#############################################################################
```

After the inputs, values needed for coordinate transformations, Earth's gravity field and solar activity are read. For this, also dedicated subroutines were written. The coordinate transformation values are saved in the `finals.sdm` (for IAU2000 reductions, they are saved in `finals2000A.sdm`) file that is provided by IERS (International Earth Rotation and Reference System Service) and can by received via www.iers.org.

The values for the Earth gravity field are saved in `egm96_to360.ascii`.
At last, the solar activity values are read. These are corresponding to the recommendations of the ECSS (European Cooperation for Space Standardization) [17]. By this recommendation, for pre-flight analyses one can choose between different options of solar activity, which are 'low', 'medium', 'high long term' and 'high short term'. After all data is read, the output file is created and prepared.
Following, the core orbit determination process is started. At first, the reference orbit is calculated, which is the orbit determined without any measurement deviations. Depending on the choice of the user, one of the methods described in 2.1, is used. Regarding to the method, range inputs or inputs for the third measurement are ignored. After determining and propagating the reference orbit, all other calculations are performed during several loops. In this loops, the measurements are deviated referring to the inputs. Again, depending on the method chosen, the range deviations are ignored. If the method uses two sets of measurements, it is possible to deviate both of them. If the method uses three sets of measurements, only the first and second measurements are deviated, the third one is kept constant. This is basically to avoid too complex outputs and calculation times due to too many deviations. Furthermore, also deviating two measurements gives a reasonable impression of the capabilities of the systems used. After a successful determination and propagation, the results are written to the output file.

Routines for orbit determination and propagation

For every type of orbit determination, different subroutines do exist. In all of them, first the Julian Date is calculated, as well as the position of the sensor in inertial Cartesian coordinates. Afterwards, the orbit determination methods as already described in section 2.1 are called. Depending on the method, further coordinate transformations have to be performed, especially for changes between the observer systems and the propagation (ECI) and inertial systems. The current version of this tool performs all transformations between ECI and ECEF coordinate frames with help of the SOFA library (IAU2000A reductions) [18], while the results shown here have been calculated with self-written subroutines (FK-5/IAU75 reductions). After a successful orbit determination, the orbit is propagated as described in section 2.2. Note that when using the angles only orbit determination sometimes slant ranges do not converge. In this case an output is presented on the screen. Usually, the determined orbit is still valid, just the set accuracy for converging was not reached. But still, the corresponding output should be handled with care. After the propagation, the subroutine returns to the main

routine, where the outputs are written.

Comparing the different routines

To get an impression of the precision of the different orbit determination methods, a test case has been run. For this, a Genesis II sighting over Stuttgart Uhlandshöhe on the 14th of June 2012, around 18.30 UT has been simulated. The results of the orbit determination for this case a summarized in table 2.1. Furthermore, the actual values from the used TLE file are stated. Note that the TLE data has not been propagated to the time of detection. This explains the deviation in right ascension of ascending node. The mean anomaly is not shown for this reason.

As one can see all the results give reasonable orbits. The deviations in the semi-major

Table 2.1: Results from different orbit determination methods

Parameter	Gauss'	Gibbs	Herrick-Gibbs	Angles only	TLE
sma [km]	6918.467	6931.789	6920.322	6919.339	6927.575
ecc [-]	0.005348	0.00382	0.005003	0.006394	0.005318
incl [°]	64.551	64.55	64.554	64.53	64.508
RAAN [°]	125.728	125.718	125.735	125.75	122.113
AoP [°]	285.323	300.77	285.443	292.556	291.197

axis are all in the range of some kilometers, the Gibbs-method comes even closer. For eccentricity, the Gauss and Herrick-Gibbs method yield best results. The inclination fits very well with all methods, same as the right ascension of ascending node. In here, all methods agree about the value, so probably it changed since the epoch of the TLE string. The argument of perigee deviates with the methods. This can be explained by the orbit being a near-circular one and the methods calculating different semi major axes and eccentricities. Because of the higher accuracy, for later analyses, the combined Gibbs/Herrick-Gibbs method was chosen for analyzing radar and laser measurements.

2.4 The accuracy of optical space debris measurements

At this point, the different optical methods for space debris measurements shall be analyzed shortly regarding their accuracy. First, the precision in the measurements itself (thus angular and range deviations) shall be assessed. Note that the aim of the assessment is only to get the magnitude of the different methods to perform reasonable simulations later on. A more comprehensive analysis of the accuracies would be far too complex at this point.

2.4.1 Determining the accuracy of radar measurement

A comprehensive analysis of radar accuracy would definitely go behind the scope of this work. Furthermore, the accuracy varies depending on many variables and is basically scalable depending on the money one is able and willing to spend. To get reasonable values, basic radar equations shall be used and be applied for a standard radar which is used to observe space debris (namely: EISCAT).
The theory used for this analysis is according to [19]. The base for the computations is the basic radar range equation. This one gives the ratio of the signal power received from the target to the background noise, received both from the environment and the noise added in the radar

$$\frac{S}{N} = \frac{P_P \tau G_T \sigma A_r}{(4\pi)^2 R^4 k T_s L} \tag{2.78}$$

where

$\frac{S}{N}$ = radar signal-to-noise ratio (power ratio)
P_P = radar transmitted peak RF power [W]
τ = radar pulse duration [s]
G_T = radar transmit antenna gain (power ratio)
σ = target radar cross section (RCS, in [m^2])
A_R = radar receive antenna effective aperture area [m^2]
R = range from the radar to the target [m]
k = Boltzmann's constant (1.38e-23 [J/K])
T_S = radar system noise temperature [K]
L = radar system losses (power ratio)

It is quite common to express the power-ratio in decibels. For this, one just has to convert all S/N,G_T and L to decibels. Furthermore, the target RCS is commonly expressed

in dBsm. The transformation is done via

$$RCS(m^2) = 10^{(dBsm/10)}. \tag{2.79}$$

In here the most critical quantity to get to calculate the signal to noise ratio are the losses. These are a combination of many different kinds, like for example the transmit microwave loss L_{MT}, the two way propagation loss L_P, the received microwave loss L_{MR} or signal processing losses L_{SP}. Problem with these is that they are in general not easy to find for real radars, but at least some of them can be estimated generally.
With help of the signal to noise ratio from equation 2.78 one can know estimate the rms errors of a radar measurement. These are the angular measurement accuracy σ_A and the range measurement accuracy σ_R. The geometry for this is shown in figure 2.6.

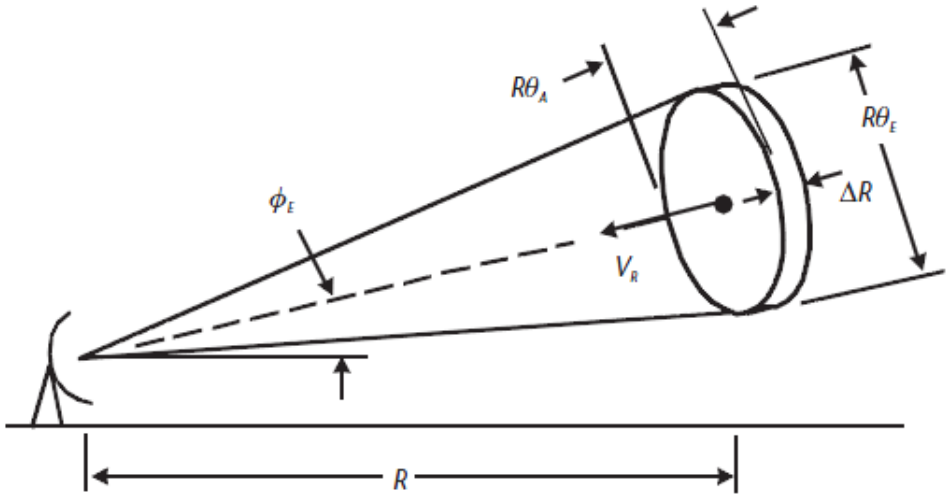

Figure 2.6: Geometry for radar measurement and target resolution [19].

Angular measurement accuracy

The angular-measurement accuracy σ_A is characterized by the rms measurement error, given by the root-sum-square (rss) of three error components.

$$\sigma_A = (\sigma_{AN}^2 + \sigma_{AF}^2 + \sigma_{AB}^2)^{(1/2)}, \tag{2.80}$$

where

σ_{AN} =S/N -dependent random angular measurement error
σ_{AF} =angular fixed random error; the rss of the radar fixed random angle error and the random angle error from propagation

σ_{AB} = angle bias error; the rss of the radar angle bias error and the angle bias error from propagation

Thereby, the σ_{AN} error is in general the by far dominating one, why at this point the other errors will be neglected. It is random, with a standard deviation for monopulse radar given by

$$\sigma_{AN} = \frac{\Theta}{k_M \sqrt{2(S/N)}}. \tag{2.81}$$

In here, Θ describes the radar beamwidth in the angular coordinate of the measurement and k_M is the monopulse pattern difference slope. While Θ is a system value, k_M is typically about 1.6, measured by the ratio of sum and difference channel voltages divided by the normalized angle off beam center. The 2 in under the root comes from the use of a σ_1 value. The total limit (for $\frac{S}{N}$) would be set by the integration time. At last, another look has to be taken on the signal-to-noise ratio. In here, one must differ between single-pulse S/N or integrated S/N, whereas the integrated S/N furthermore is split up into coherent and incoherent integration. For single-pulse measurements, equation 2.78 can be used.
Integration of radar pulses is used to increase radar sensitivity by adding the return signals from several transmitted radar pulses. Coherent integration means that the adding occurs when the signals returns are added prior to the envelope detection process in the radar receiver. Non-coherent integration means that the signal returns are added after the demodulation. As this is not the topic of this thesis, one can say in general that coherent integration is more efficient, but also by far more complex to realize, while non coherent integration is quite easy to realize, but less efficient, especially when integrating large numbers of pulses (e.g. several hundreds). As the later viewed EISCAT radar uses coherent integration, only the formula needed for this case will be given. In here, it is quite easy: One has just to multiply the $\frac{S}{N}$ from a single return pulse by the number of pulses one wants to integrate

$$\left(\frac{S}{N}\right)_{CI} = n \cdot \frac{S}{N}. \tag{2.82}$$

Of course this is just the theoretical value. In here, further losses will add up, like losses in the integration process L_{SPI}. These occur when the signal processing is not optimum, or when the signal returns do not maintain the expected phase relationship. This can happen for several reasons (like an unstable target, an unstable propagation path etc.) and shall not be considered at this point. With this signal-to-noise ratio, equation 2.81

can be used to geth the σ_1 error from signal-to-noise in angle measurements. The other errors (σ_{AF} and σ_{AB}) are system related values and shall not be further discussed in here.

Range measurement accuracy

The calculation of the range measurement deviation is done similar to the angular measurement deviation. Again, the rms measurement error, σ_R, is given by the root-sum-square (rss) of three error components

σ_{RN} =S/N -dependent random range measurement error
σ_{RF} =range fixed random error, the rss of the radar fixed random range error and the random range error from propagation
σ_{RB} =range bias error, the rss of the radar range bias error and the range bias error from propagation

Again, σ_{RN} is the dominating error, the others will be neglected. It can be described as

$$\sigma_{RN} = \frac{\Delta R}{\sqrt{2(S/N)}} = \frac{c}{2B\sqrt{2(S/N)}}. \tag{2.83}$$

In here, the signal-to-noise ratio is calculated as in formula 2.78, with the same extension for coherent integration as described in paragraph 2.4.1. As with the angular measurement, the 2 under the root takes in account the statistical approach. ΔR describes the range resolution, which can be calculated as

$$\Delta R = \frac{c\tau_R}{2} = \frac{c}{2B}. \tag{2.84}$$

Again, τ_R is the radar pulse length in [s], c is the propagation time of the beam through the medium in $[fracms]$. A limit for accuracy (for $\frac{S}{N} = 1$) would again be given by the integration time directly. The other σ are also system properties, and will not be considered in here.

Calculations for EISCAT-Radar

With the equations described before, an estimation for radar measurement accuracy has been undertaken for the *EISCAT* (***E**uropean **I**ncoherent **SCAT**ter*) UHF radar at Tromsø, Norway. For the calculations, a small matlab tool has been written, which is shown in the appendix (C.1). The used inputs are summarized in table 2.2, and are

basically from [20]. Due to the lack of data, some inputs, especially system dependent losses, are estimations (when mentioned), but the results should still lie in a realistic range, sufficient for the purpose of use. The number of coherent integrations is calculated from a maximum integration time of 300 ms and a typical interpulse period for EISCAT from about 10 ms [20] and [21].

Table 2.2: Inputs for measurement accuracy estimation, EISCAT UHF radar

Input	Value
peak power P_P	1.5 [MW]
pulse duration τ	$2.e-6$ [s]
gain of transmitter G_T	64565 [factor]
receiving area A_R	3216.033998 [m^2]
radar cross section of object σ	0...10 [m]
range R	800 [km]
system noise temperature T_s	100 [K]
overall losses L	75 (estimated)
coherent integrations n	30
radar beamwidth Θ	0.5 [°]

With these inputs one yields the results as shown in figure 2.7 and 2.8 below. Both the results for single pulse and coherent integration are shown. As seen, the accuracy

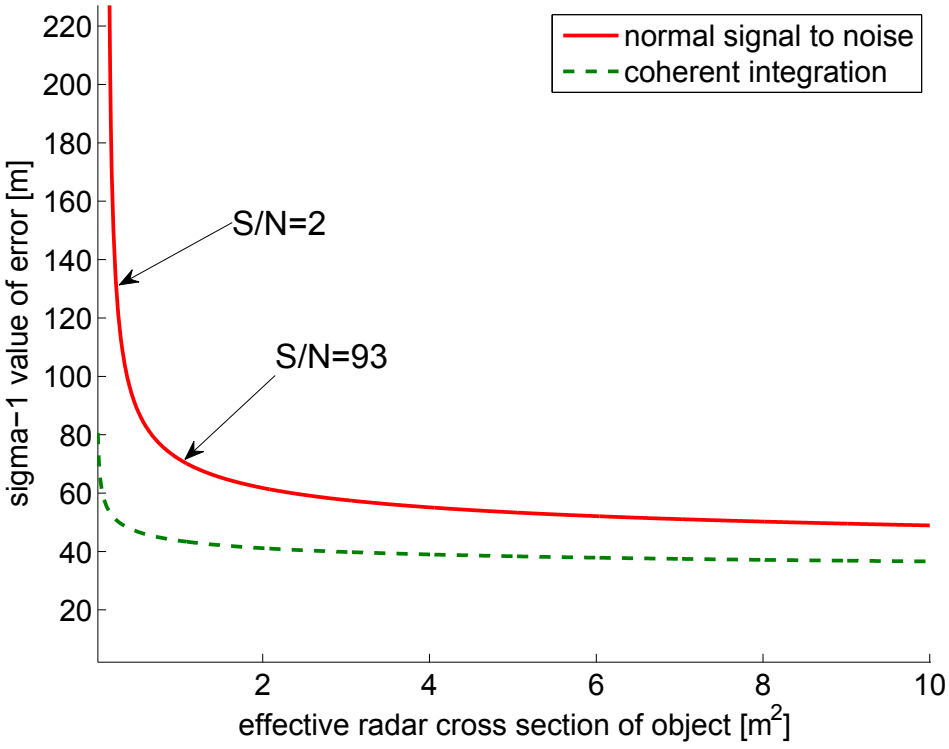

Figure 2.7: Range error for coherent and single shot radar measurements.

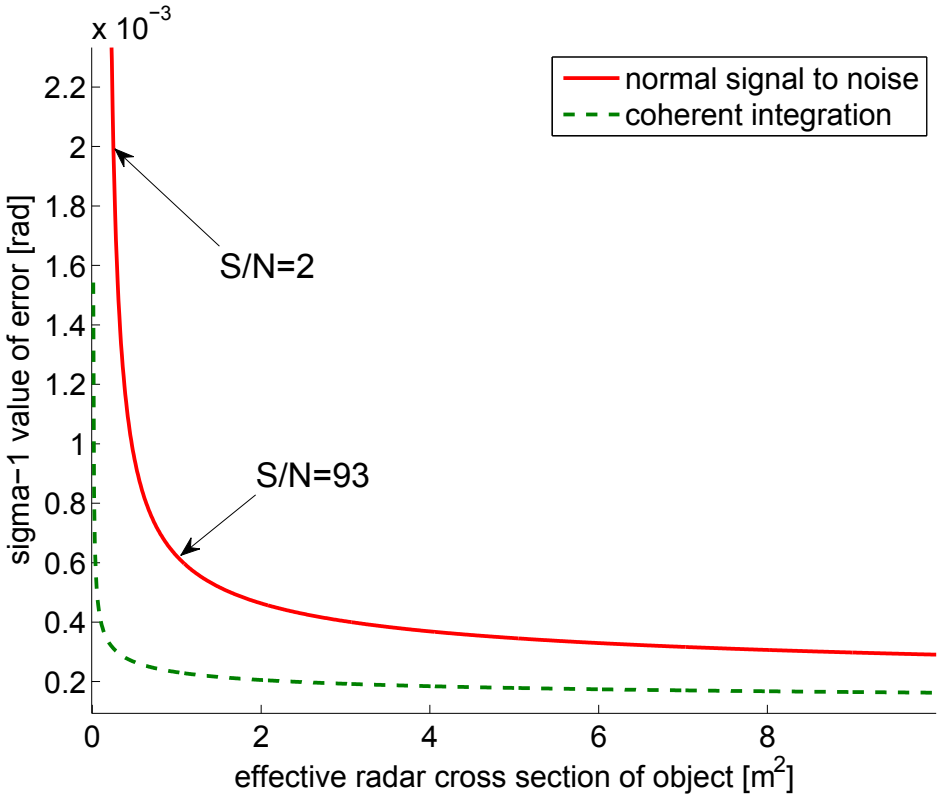

Figure 2.8: Angular error for coherent and single shot radar measurements.

decays rapidly with decreasing object size. This is critical, as with space debris observations, objects with sizes below 10 cm are of very high interest. For further analysis, the values for coherent and single shot measurement for objects with a size of 10 cm and 1 m have been taken.

2.4.2 Determining the accuracy of laser measurements

For the laser measurement accuracy, only a short estimation on the measurement accuracy shall be given. The DLR sets as the border for detectability a signal-to-noise ration of 4 (which corresponds to a needed received power from the ranging laser of 4nW of an object at 600 km distance). The laser analyzed at this point shall have a pulse energy of $E_P = 1$ J and a pulse duration of $\tau_p = 10$ ns. For more details on these values, please refer to [4].

The pulse duration is also the driving force for the range accuracy determination, which is set by the distance the light travels during this time. By the fact that the light travels back and forth, this number further has to be divided by two. For a pulse

duration of 10 ns one yields

$$\tau_p \cdot c = \frac{10\text{ns}}{2} \cdot 299792458\frac{m}{s} \approx 1.5m, \tag{2.85}$$

with c being the speed of light in vacuum.
This value is only valid if the object is smaller than the distance the laser travels during the pulse duration, because it is unclear from where at the illuminated objects the photon was reflected. Thus, for larger objects, the object size would define the accuracy. To also account for uncertainties that appear in the detector or during computer processing, the range error is doubled and set to 3 m.
For the angular measurement, basically the seeing conditions, mounting accuracy and the beam divergence of the laser are the critical values. [22] gives seeing conditions of 2″ for typical nights, which lead to an angular deviation of about $\Delta seeing \approx 10\ \mu$rad. Newest hight tech telescope mounts yield similar values for pointing accuracies of down to 1″ in both azimuth and elevation (for example the Air Force Maui Optical Station (AMOS)). The Astelco NTM 500 mount, used by the DLR at the Uhlandshöhe test station, yields values below 5″ across the entire sky [23]. This leads to an angular deviation of $\Delta_{mount} = 24.2\ \mu$rad.
The laser beam divergence can be calculated via the BPP (beam parameter product) equation

$$BPP \approx \frac{d \cdot \Theta}{4} = M^2\frac{\lambda}{\pi}, \tag{2.86}$$

with d being the waist of the laser (in this case the diameter of the sending aperture), Θ the divergence angle, M^2 the ratio of the divergence of the real laser beam and a Gaussian beam and λ the wavelength. In this case, $d = 0.1$ m, $M^2 = 1$, as a Gaussian beam is assumed at this point, and $\lambda = 1030$ nm. With these values one yields $\Theta = 1.3114e-5\text{rad} = 13.114\mu\text{rad}$.
Those values are combined to get the root mean square value for the laser measurement deviation

$$\Delta_{angle_{RMS}} = \sqrt{\Theta^2 + \Delta^2_{mount} + \Delta^2_{seeing}} = 29.2851\ \mu rad. \tag{2.87}$$

Note that both the values for range deviation and angular deviation would grow in practice due to other environmental influence and noises. But as at this point it is only the aim to get the magnitude of the deviations, these assumptions are considered to be good enough.

2.4.3 Determining the accuracy of passive optical measurements

For the passive optical measurements, which are measurements that use the sun only for illumination of the object, only angular deviations have to be considered as now range measurement is performed. Hence, the dominating error sources are the seeing and the mount positioning errors. The seeing conditions are again set to 2″, the mount accuracies to 5″. This sums up to

$$\Delta_{angleRMS} = \sqrt{\Delta_{mount}^2 + \Delta_{seeing}^2} = 26.1847\ \mu\text{rad}. \tag{2.88}$$

This seems to be a very good value. But one has to take into account that usually further deviations add up, for example due to the angle read out of the mount.

2.5 Results

The tool `analyseMeasurements` was used to determine the accuracy of preliminary orbit determination from passive optical, radar and laser measurements. The general process of the performed analyses is as following: At first, a reference orbit is calculated. This reference orbit is defined as the orbit determined with no errors in the measurements. As determination method, that method that is also used for the analysis is applied. For the accuracy of the determination method itself, please refer to section 2.3.2. Afterwards, the program `analyseMeasurements` is used to deduct the influence of measurement deviations on the orbit both directly after measurements and afer propagation of the orbits for one day.
To begin with, the inputs shall be described.

2.5.1 Inputs

At first, a valid sighting has to be determined. This is done with the tool described in section 2.3.1. This tool needs as inputs coordinates of a site, a time frame in which sightings shall to be searched and a valid TLE data set for this time frame. As site, Stuttgart Uhlandshöhe, and as time frame mid June 2012 were chosen. As TLE data, a set from the private American Genesis II space habitat was chosen. The TLE set is shown below.

```
1 31789U 07028A   12167.96009037 +.00002516 +00000-0 +18075-3 0 03875
2 31789 064.5075 122.1127 0053176 291.1966 068.3474 15.05673112272755
```

For comparisons, the orbital parameters calculated directly from the TLE file were already shown in table 2.1.

The tool `getSightings` yields a set of several sightings, from which one was chosen for the analysis. The three measurements used later on are shown in table 2.3. Note that for angles only orbit determination, the range values are ignored. Next the deviations

Table 2.3: Sightings used for analysis.

Parameter	Sighting 1	Sighting 2	Sighting 3
date	15 Jun 12 23:29:06	15 Jun 12 23:33:36	15 Jun 12 23:36:06
range [m]	2690649.66	958984.82	670673.19
azimuth [DEG]	320.71	326.71	123.6
elevation [DEG]	1.19	34.94	60.41

assumed for the measurements had to be determined. This was already described in

sections 2.4.1, 2.4.2 and 2.4.3. The inputs are summarized in table 2.4. As the accuracy for radar measurements highly depends on the diameter of the object to observe, there are two different runs made for radar measurements, one for a 10 cm sphere, and one for a 1 m sphere.

Table 2.4: Deviations used for analysis.

Deviation	passive optical	laser	radar, 10 cm	radar, 1 m
range deviation [m]	-	3	57.62	45
angular deviation [μrad]	26.1847	29.2851	402.9	231.6

At last, several other inputs are needed. These include the propagator options, such as time step, propagation time and tolerances, and characteristics of the object to be propagated. As objects, a sphere of a 1 m diameter has been used, for the radar as mentioned before, additionally a 10 cm sphere has been simulated. To calculate the mass of the objects, density values for typical space debris objects referring to [24] have been used (, as drag coefficient the standard value of 2.2 was chosen. The flags and deviations, and deviation steps are changed depending on the run. These inputs are summarized in table 2.5.

Table 2.5: Further inputs for calculations.

Parameter	Value	Alternative value
geod. height of sensor [m]	351.1	-
geod. latitude of sensor [DEG]	48.7834	-
geod. longitude of sensor [DEG]	9.1975	-
propagation time [s]	86400	-
propagation time step [s]	2	-
solar activity	medium	-
size of gravity field	18	-
relative tolerance of ode solver	1.e-9	-
absolute tolerance of ode solver	1.e-9	-
mass of object [kg]	300	0.733 [1]
eff. surface of object [m^2]	0.7854	0.0079 [1]
C_D of object	2.2	-
time difference TAI $\rightarrow$ UTC	34.0	-

[1] radar 10 cm object

2.5.2 Radar measurements

At first, the results for Radar measurements shall be presented. For both 10 cm and 1 m spheres, four different runs have been performed. During the first three ones, always one measurement has been deviated, each time the second range, azimuth and elevation measurement. This was done, to get an impression of the influence of the single measurements. In the fourth run, all deviations have been changed to get the maximum errors in orbit determination due to the measurement deviations. The calculated reference orbits (after propagation) are shown in table 2.6. Reference orbits are defined as those orbits that are determined with no errors in the measurements.

Comparing this to the input orbit from table 2.1 shows a good result for the reference orbit. Note that the stated input orbit is valid for the current TLE epoch and has not been propagated to the time of the measurements, which explains the deviation in the mean anomaly. Due to the spacing of the measurement being all over 5°, only the Gibbs method was applied.

Table 2.6: Reference orbits for radar calculations.

Parameter	Value 1 m	Value 10 cm
semi major axis [km]	6930.74	6930.71
eccentricity [-]	0.00396	0.00396
inclination [DEG]	64.5578	64.5578
RAAN [DEG]	121.845	121.845
argument of perigee [DEG]	299.89	299.89
mean anomaly [DEG]	193.318	193.339

Now, the influence of single deviations in the measurements shall be shown. As error indicator, the absolute error of the position after one day of propagation has been chosen. This is due to the importance of the position after a certain time for re-detecting an object. The figures 2.9 to 2.11 show the influence of one deviated measurement (either second azimuth, second elevation or second range) on the initial state vector at second position on the left hand side, and on the right hand side the propagated position vector after one day.

In here it is clearly visible that the largest influence on the orbit accuracy is due to the errors in elevation measurements, followed by the range error and finally the azimuth error.

On the first look, one might assume that due to similar absolute errors in the position vector before propagation the errors after propagation should be also in a similar range. But when taking into account the initial orbits before propagation one sees that

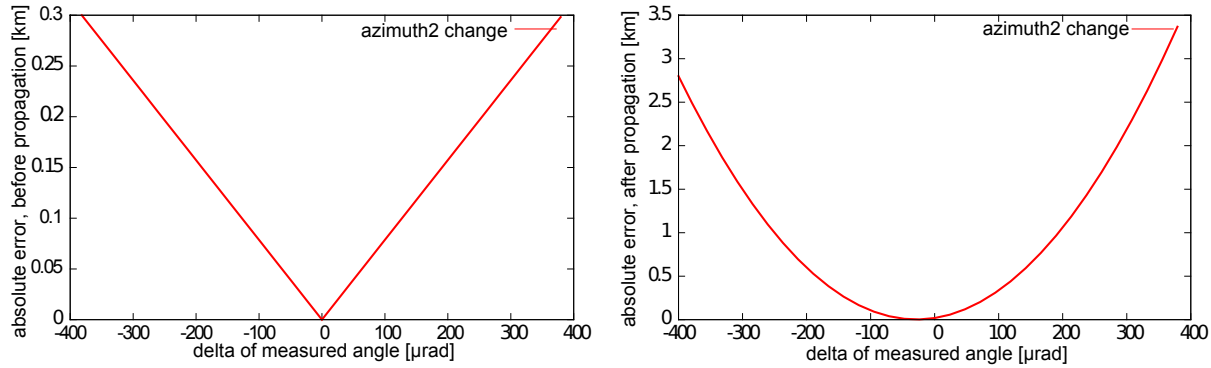

(a) Before propagation (b) After propagation

Figure 2.9: Influence of azimuth measurement deviation on orbit, for radar measurement of 10 cm sphere.

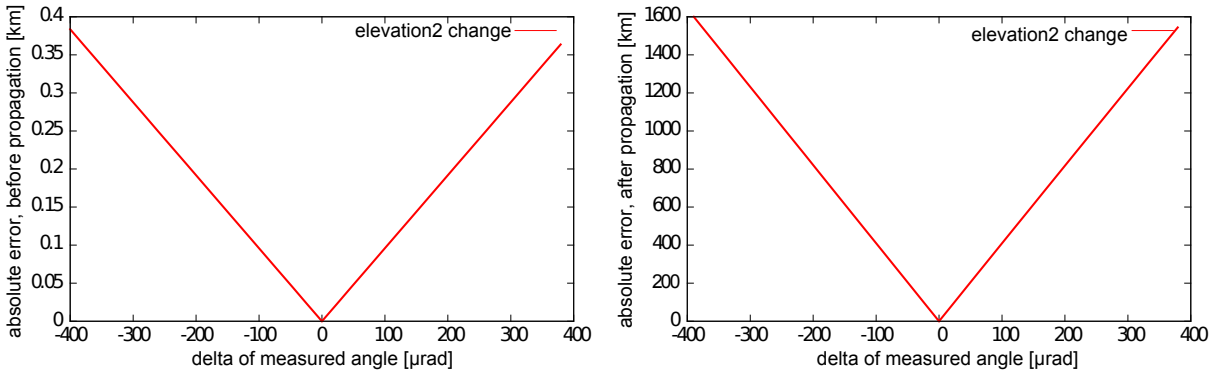

(a) Before propagation (b) After propagation

Figure 2.10: Influence of elevation measurement deviation on orbit, for radar measurement of 10 cm sphere. For extreme absolute errors, please refer to the text.

the elevation error leads to completely different orbits, where the azimuth deviation affects the position, but not as much the velocities and thus not as much the final orbit. To point this out, the initial orbit parameters (before propagation) for maximum elevation and azimuth deviation are shown in table 2.7. The much larger effect of the elevation on the results can be explained by its influence of the elevation in the calculation of the slant ranges from the site's position to the object.

For the next simulation, errors for all angular and range measurements were assumed for both the first and second measurement. This leads to a wide combination of different deviated measurements. The results are shown in figures 2.12 and 2.13 for the radar 10 cm sphere simulation and in figures 2.14 and 2.15 for the radar 1 m sphere simulation.
This shows that although the absolute errors before the propagation are quite low, the

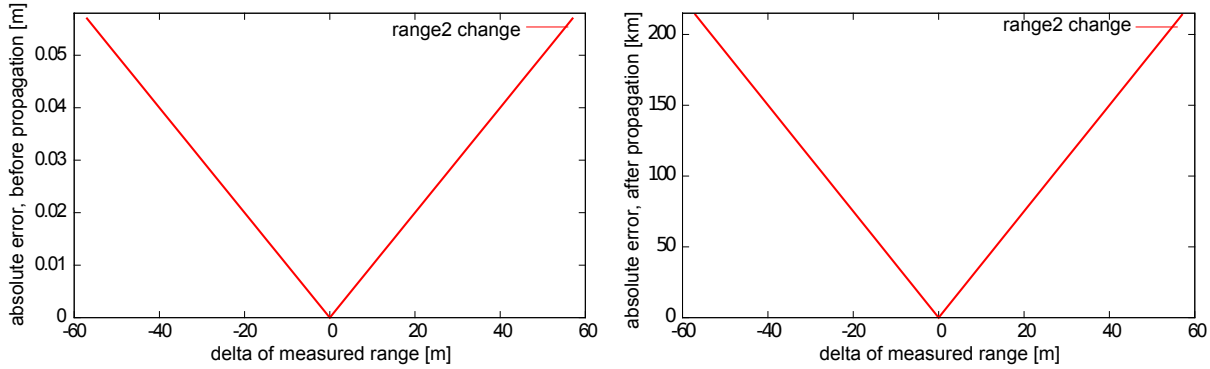

(a) Before propagation (b) After propagation

Figure 2.11: Influence of range measurement deviation on orbit, for radar measurement of 10 cm sphere. For extreme absolute errors, please refer to the text.

Table 2.7: Initial orbits with maximum derivations for radar measurement of 10 cm sphere.

Parameter	max. range dev.	max. azimuth dev.	max. elevation dev.
semi major axis [km]	6932.27	6930.73	6942.52
eccentricity [-]	0.00374	0.00396	0.00234
inclination [DEG]	64.5577	64.5524	64.5585
RAAN [DEG]	121.845	121.851	121.884
arg. of perigee [DEG]	300.32	299.882	305.445
mean anomaly [DEG]	176.18	176.617	171.042

errors after the propagation get enormous. Again the high influence of the error in elevation measurement is clearly visible: The groups of similar results are always runs with a constant elevation. In here it is interesting that the largest errors in the orbit after propagation do not necessarily occur for maximum errors in the measurements (where range and both angles are deviated to the maximum), but depend on the combination of the errors. This is quite clear, as an orbit with all measurements deviated towards one direction still is a very similar orbit, just slightly shifted. It shows that worst cases appear, when angular errors in the measurements with opposite signs appear. To get an overview of this effect, the orbital elements for some of the calculations (radar 1 m sphere) are shown in table 2.8. As also visible from the figures for radar 1 m sphere, the results only differ in the magnitude of the results.

Note that here mostly the maximum errors are considered, and furthermore the results only apply to initial orbit determination.

Table 2.8: Determined initial orbits with different measurement errors for radar measurement of 10 cm sphere.

Parameter	Orbit 1	Orbit 188
Δ_{range}, 1st [m]	-58.0	-58.0
Δ_{range}, 2nd [m]	-58.0	58.0
$\Delta_{elevation}$, 1st [rad]	-4.03e-4	-4.03e-4
$\Delta_{elevation}$, 2nd [rad]	-4.03e-4	4.03e-4
$\Delta_{azimuth}$, 1st [rad]	-4.03e-4	4.03e-4
$\Delta_{azimuth}$, 2nd [rad]	-4.03e-4	-4.03e-4
sma [km]	6928.92	6902.47
ecc [-]	0.00421	0.00812
incl[DEG]	64.5815	64.5568
RAAN [DEG]	121.861	121.84
aop [DEG]	303.892	298.517
meanA [DEG]	172.565	177.982
absolute error, before prop.[km]	0.5031	0.50308
absolute error, after prop.[km]	257.431	3918.6

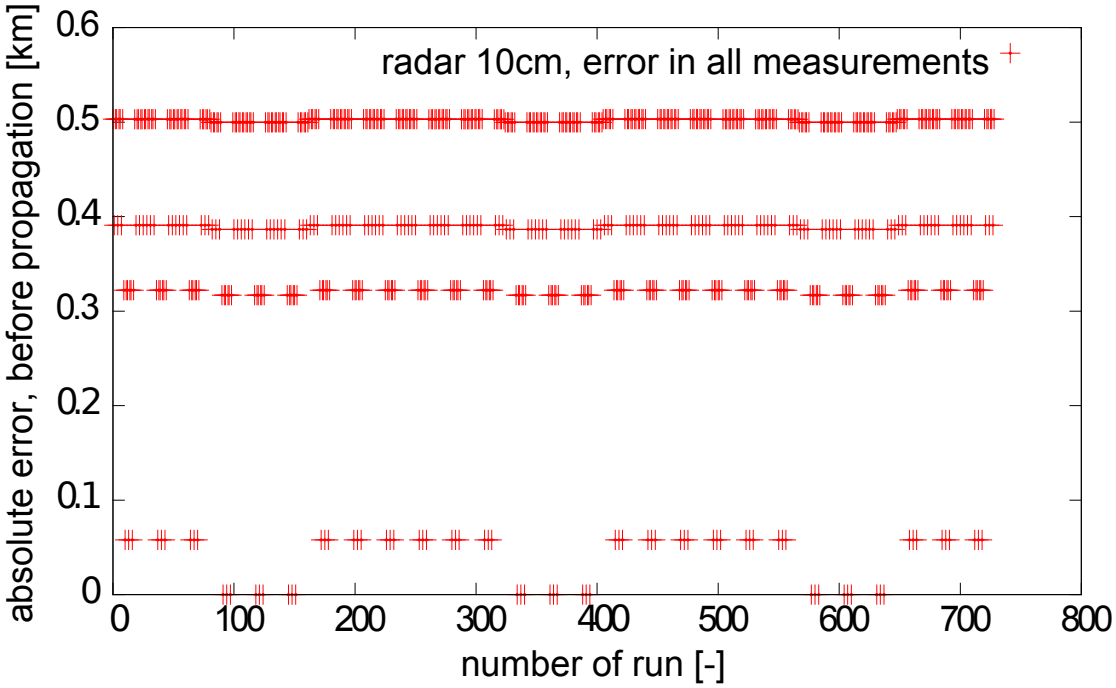

Figure 2.12: Measurement deviations for errors in both angle and range measurements, before propagation, for radar measurements of 10 cm sphere.

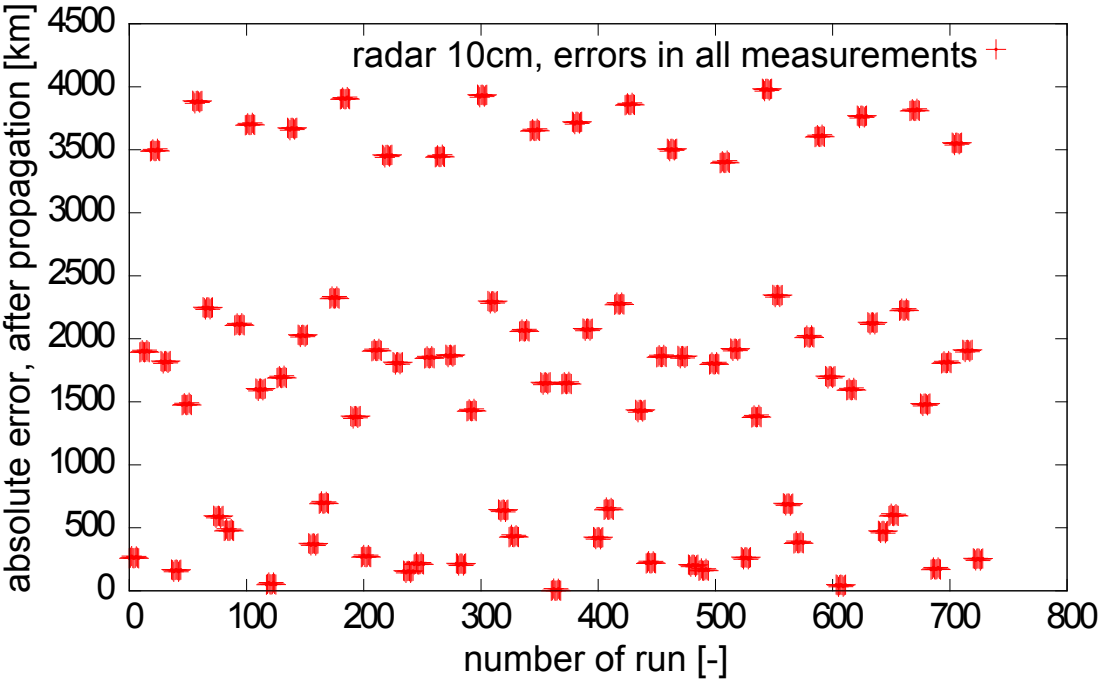

Figure 2.13: Measurement deviations for errors in both angle and range measurements, after propagation, for radar measurements of 10 cm sphere. For extreme absolute errors, please refer to text.

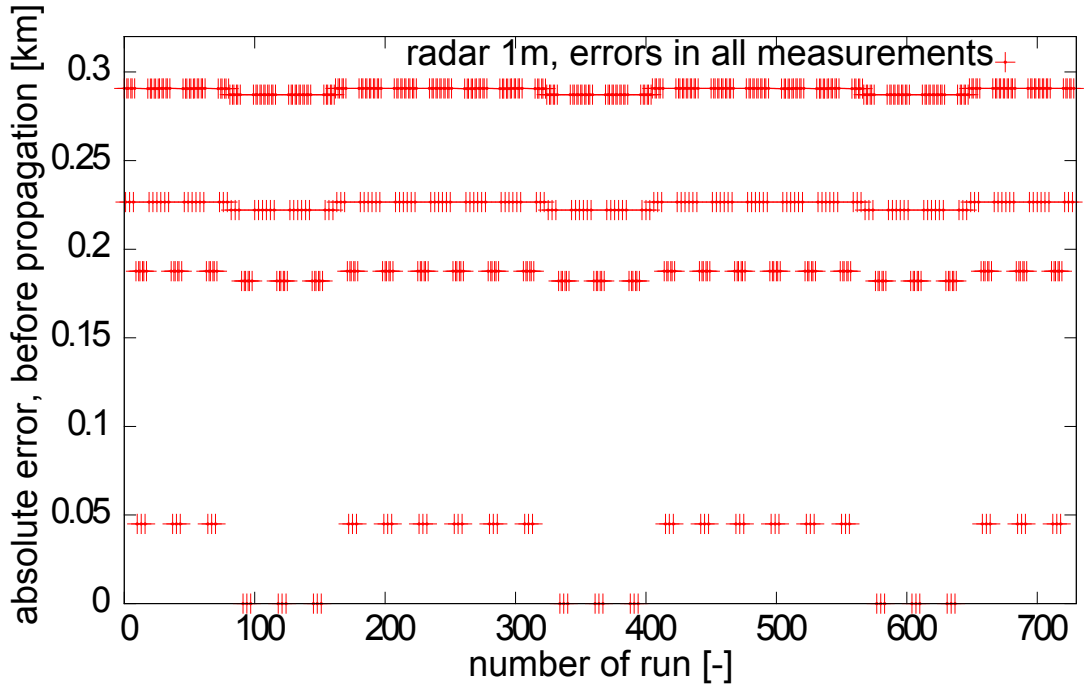

Figure 2.14: Measurement deviations for errors in both angle and range measurements, before propagation, for radar measurements of 1 cm sphere.

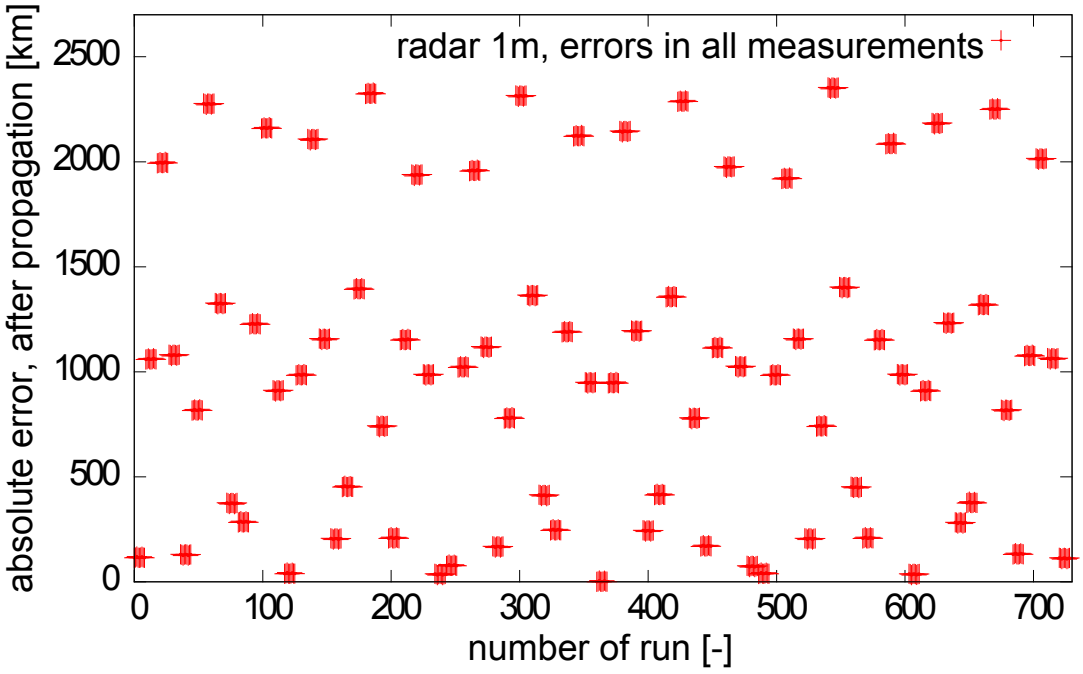

Figure 2.15: Measurement deviations for errors in both angle and range measurements, after propagation, for radar measurements of 1 m sphere. For extreme absolute errors, please refer to text.

2.5.3 Passive Optical Measurements

Secondly, the results yielded for passive optical measurements shall be shown. Again, first the calculated reference orbit shall be presented (table 2.9). Again, the reference orbit is that orbit that could be determined when no errors in the measurements were assumed.

Table 2.9: Reference orbit for passive optical calculations

Parameter	Value (1 m)
semi major axis [km]	6867.0651
eccentricity [-]	0.001306
inclination [DEG]	64.49204
RAAN [DEG]	301.928236
argument of perigee [DEG]	252.9364
mean anomaly [DEG]	277.08579

Comparing these results to the input orbit from table 2.1 shows that orbit determination from angles only does not always give good results. This is due to the missing range measurements which have to be computed from the angles. Still the influence of the measured deviations on the final propagated orbit shall be investigated.
When first looking at the single deviations (figures 2.16 and 2.17), one sees that this time the influence on the orbit from both the measurements elevation and azimuth changes are much closer together than for radar measurements. In fact, azimuth deviations have a higher influence than elevation errors. The misalignment of the elevation simulation can be explained by reoccurring float operations in the process: As visible the minimum of the absolute error before propagation is not aligned with the minimum error of the delta of measured angle. This happens because the overall deviations in this range are below the accuracy of the whole process. When changing to larger deviations, this effect becomes more and more negligible.

Secondly, the results for deviations of both angles in the first and second measurement shall be presented. Figures 2.18 and 2.19 present the outputs. Note that in here, only the angular measurements of the first and second measurement have been deviated. The range is not considered in this method. Due to the other method used for orbit determination, the distributions of the resulting absolute errors are very different to those achieved for the radar simulations: Instead of grouping around deviations for one kind of measurements (like elevation measurements for radar) a quite equal distribution is visible. As stated already before, the error in the azimuth measurement is

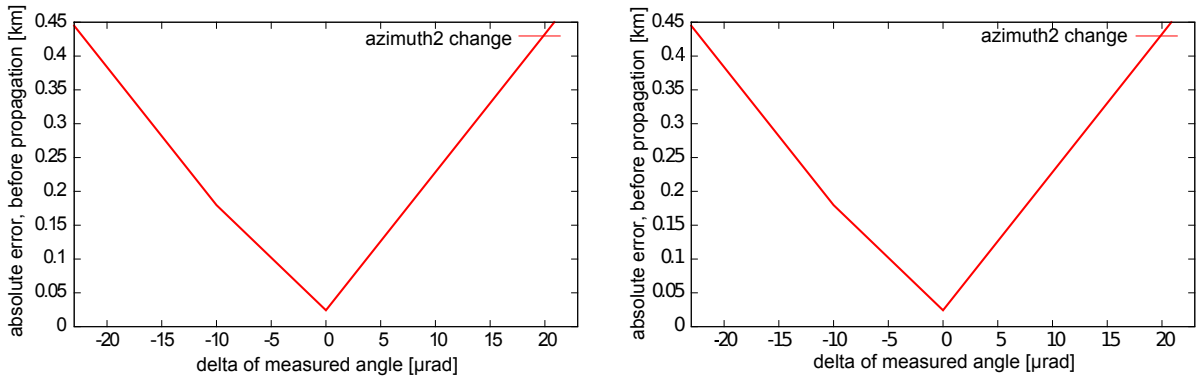

(a) Before propagation (b) After propagation

Figure 2.16: Influence of azimuth measurement deviation on orbit, for telescope measurement of 1 m sphere.

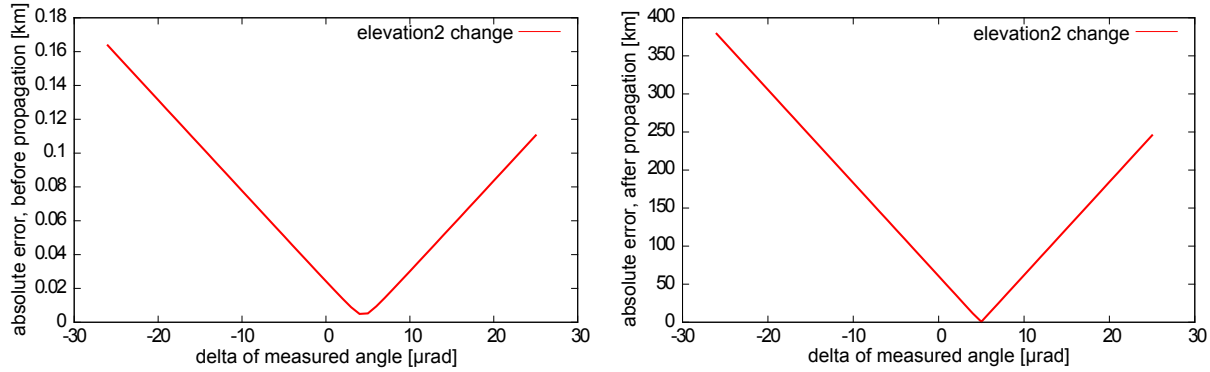

(a) Before propagation (b) After propagation

Figure 2.17: Influence of elevation measurement deviation on orbit, for telescope measurement of 1 m sphere. For extreme absolute errors please refer to text.

by far more influencing than for the Gibbs method. By this, the deviations rise over on loop of azimuth change (which means: All values but the second azimuth change stay constant. With a rising difference of the second azimuth to the first azimuth, the absolute error gets larger. For this, also refer to table 2.10). Again, the largest deviations do not necessarily lead to the largest errors in the orbit, the same effect as for radar measurements can be observed: The combination is crucial for the final error. Furthermore, this method shows a much clearer correlation of the absolute error before propagation, the determined and thus the absolute error after propagation. This is reasoned by the method: In here, not only the velocities have to be calculated, but also the range and from this the position of the object. Thus, an error in the determined position leads to a further variance in the calculated velocities, and this to a possible larger error in the final orbit. To show these effects (the combinations of errors and the correlation between absolute error before and after determination), again some exemplary orbits are

given in table 2.10. Please note that all results shown here are referring to the reference orbit calculated with that same method, not the actual orbit.

Table 2.10: Determined initial orbits with different measurement errors for telescope measurement of 1 m sphere.

Parameter	Orbit 1	Orbit 2	Orbit 3	Orbit 122
$\Delta_{elevation}$, 1st [rad]	-2.6e-5	-2.6e-5	-2.6e-5	-2.6e-5
$\Delta_{elevation}$, 2nd [rad]	-2.6e-5	-2.6e-5	-2.6e-5	2.6e-5
$\Delta_{azimuth}$, 1st [rad]	-2.6e-5	-2.6e-5	-2.6e-5	2.6e-5
$\Delta_{azimuth}$, 2nd [rad]	-2.6e-5	-1.3e-5	0	-2.6e-5
sma [km]	6871.84	6876.35	6880.86	6844.74
ecc [-]	0.01272	0.01209	0.01146	0.01655
incl[DEG]	64.4918	64.4923	64.49276	64.4904
RAAN [DEG]	121.928	121.928	121.928	121.927
aop [DEG]	287.085	286.655	286.179	289.072
meanA [DEG]	189.68	190.106	190.579	187.711
absolute error, before prop.[km]	0.17644	0.43955	0.704554	1.43757
absolute error, after prop.[km]	462.976	1111.39	1756.17	3484.86

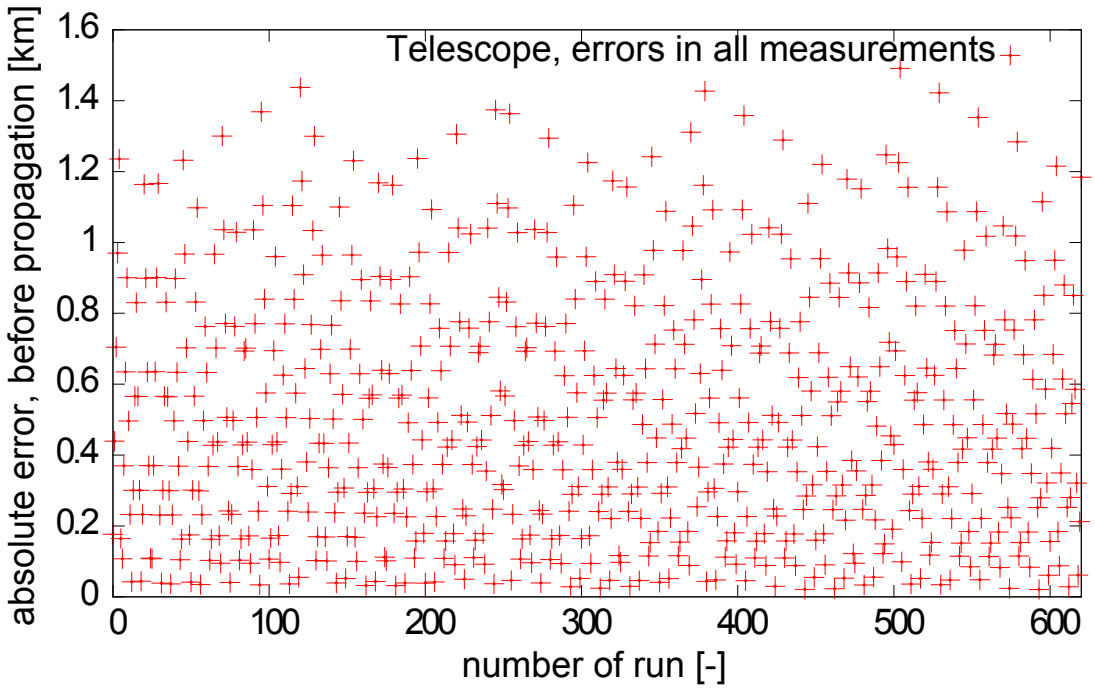

Figure 2.18: Measurement deviations for errors in both angle measurements, before propagation, for telescope measurements of 1 cm sphere.

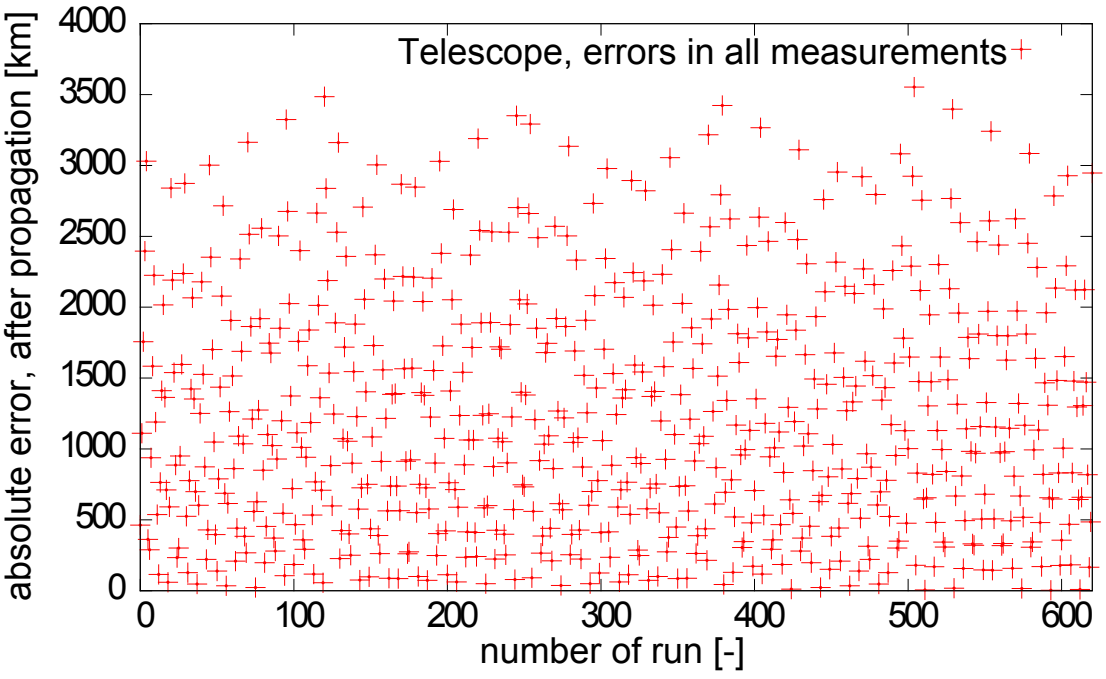

Figure 2.19: Measurement deviations for errors in both angle measurements, after propagation, for telescope measurements of 1 cm sphere.

2.5.4 Laser Measurements

Last, the results yielded with laser measurements shall be shown. The inputs were as defined in section 2.5.1. Just as for radar, four runs have been performed: Three runs with changing the first of each measurement, and a fourth one changing all measurements. The calculated reference orbit (after propagation) is shown in table 2.11.

Table 2.11: Reference orbit for laser measurements.

Parameter	Value
semi major axis [km]	6930.74017
eccentricity [-]	0.00396
inclination [DEG]	64.55784
RAAN [DEG]	121.84501
argument of perigee [DEG]	299.89025
mean anomaly [DEG]	193.31844

As the method used for this calculation is identical to the one used for radar calculations, the reference orbits are identical. Also, due to the same method used, the results are qualitatively very similar to those achieved for radar measurements. For this reason, the figures for single measurements will be skipped; just an overview of the initial orbits for maximum measurement deviations will be given in table 2.12.

Table 2.12: Initial orbits with maximum deviations for laser measurements of 1 m sphere.

Parameter	max. range dev.	max. azimuth dev.	max. elevation dev.
semi major axis [km]	6930.83	6930.75	6931.62
eccentricity [-]	0.00395	0.00396	0.00383
inclination [DEG]	64.5578	64.55774	64.5579
RAAN [DEG]	121.845	121.845	121.845
arg. of perigee [DEG]	299.912	299.89	300.131
mean anomaly [DEG]	176.59	176.611	176.369

The results for deviations over both angular and range of the first and second measurement also lead to a qualitatively similar result as for radar measurements. Of course, due the lower errors in measurements, the absolute errors of the orbit are much lower. Table 2.13 gives an overview of the influence of different combinations of measurement errors on the initial orbit.

Table 2.13: Initial orbits with different measurement errors for laser measurement of 1 m

Parameter	Orbit 1	Orbit 542
Δ_{range}, 1st [m]	-3	3
Δ_{range}, 2nd [m]	-3	-3
$\Delta_{elevation}$, 1st [rad]	3.e-5	
$\Delta_{elevation}$, 2nd [rad]	-3.e-5	
$\Delta_{azimuth}$, 1st [rad]	-3.e-5	
$\Delta_{azimuth}$, 2nd [rad]	-3.e-5	
sma [km]	6930.59	6932.82
ecc [-]	0.00398	0.00366
incl[DEG]	64.5571	64.5571
RAAN [DEG]	121.846	121.846
aop [DEG]	300.195	300.107
meanA [DEG]	176.303	176.395
absolute error, before prop.[km]	0.03732	0.03732
absolute error, after prop.[km]	22.9817	291.603

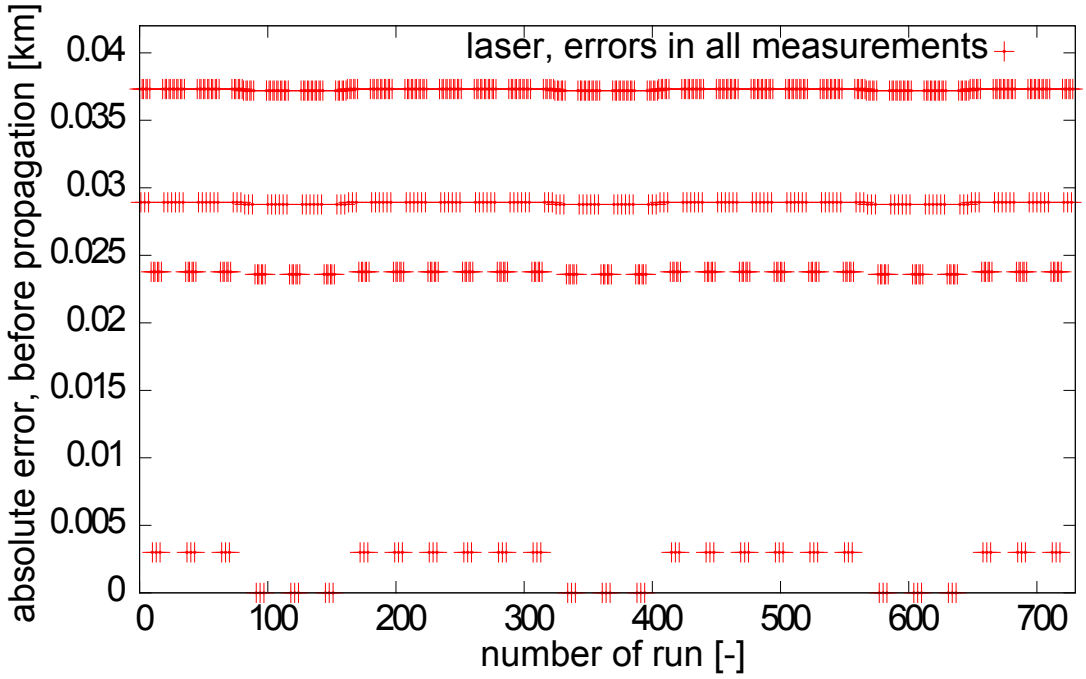

Figure 2.20: Measurement deviations for errors in both angle and range measurements, before propagation, for laser measurements of 1 cm sphere.

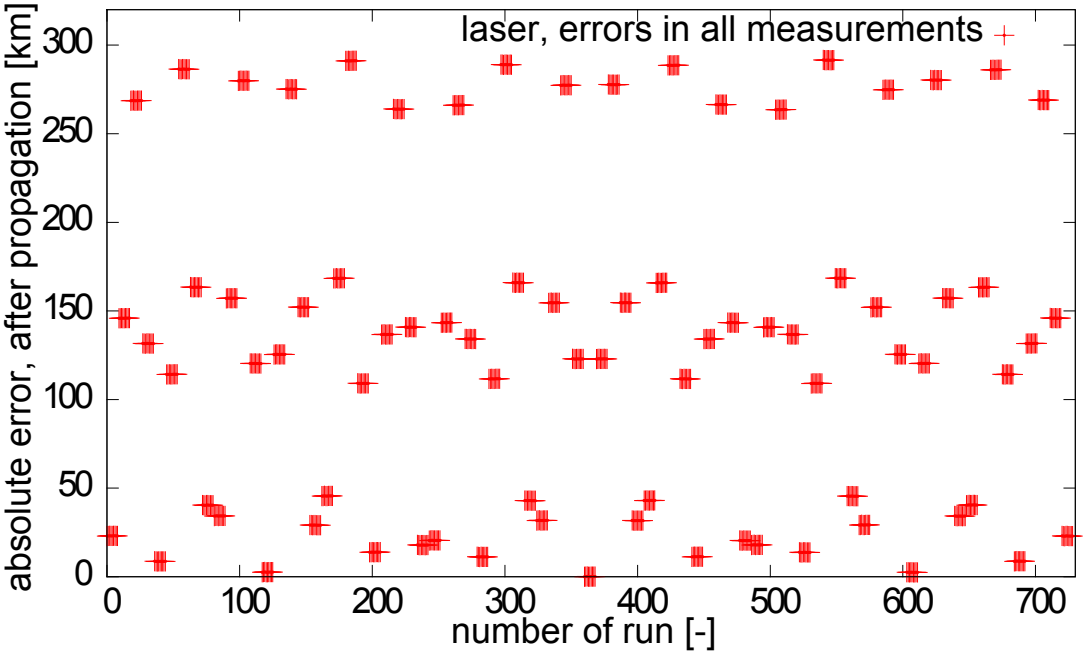

Figure 2.21: Measurement deviations for errors in both angle and range measurements, after propagation, for laser measurements of 1 cm sphere.

2.5.5 Summary

In this section, a short summary of the results shall be given. It has been shown, both with radar and laser measurements, that the distance information helps getting a much better initial orbit determination when comparing the determined orbit with the true orbit, as calculated from TLE data. Furthermore it was shown that the absolute error, crucial for a re-detection of an object, is by far best for laser measurement due to the lowest deviations to be expected. Also it was shown that the propagated results for passive optical measurements are, depending on the size of the object, worse than those from radar measurements, although the used deviations for telescopes were the lowest. As a summarizing overview, table 2.14 shows the mean and maximum deviations for the different orbits.

Table 2.14: Maximum and mean absolute errors, all methods, after propagation

method	maximum absolute error [km]	mean absolute error [km]
radar, 10 cm	3984.916	1575.069
radar, 1 m	2353.713	1017.615
telescope	3552.739	1242.82
laser	291.603	131.302

2.6 Conclusion: Comparing space debris observation systems

In the prior sections, an analysis regarding the accuracies for initial orbit determination with different space debris methods have been undertaken. This conclusion shall now use the results stated in section 2.5 and put them into context for the different use of the space debris observation methods.

When only referring to the accuracies for initial orbit determination achieved with the different space debris observation methods, laser measurements gain the best results. The problem with this method is though, to first find an object. Unless for example passive optical measurements, the field of view is reduced by the laser beamwidth to very few μrad. Furthermore, for a valid distance determination, a reasonable prediction is needed. This is because one needs an approximate time-of-flight of the light to fit the range gate of the detector to the current measurement and match the detected photons to the correct time of sending. Thus, laser measurements only make sense in combination with other measurement systems. As TLE data is usually not accurate enough to re-find this with a laser only, the method of choice would be to first get predictions from TLE data, allocate these predicted objects with a passive-optical system and finally apply the laser measurement, to get best results. This method already has been applied and proofed working in the scope of the DLR project at the Sternwarte Lustbuehel in Graz ([6]). This system makes the combination of passive- and active-optical measurements ideal to determine high-precision orbits for already detected objects. A completely new detection is restricted by the capabilities of the passive-optical method. First, initial guesses are very inaccurate, thus re-finding the object and identifying it as the same object would be critical. Furthermore, the detection of objects in LEO with passive optical telescopes is already a big problem. This is analyzed in more detail in chapter 3.
Radar measurements have shown less accuracy than laser measurements. But as Weigel has shown in [25] after a certain number of sightings, the accuracies of laser and radar measurements do converge. But because of different initial accuracies, radars in general need more sightings for this. Furthermore radar systems, or rather phased-array radar systems, have the capability of tracking several objects at one time. This makes them perfect for the maintenance of space debris catalogs [1].
In the following, the focus of this work shall be on the combination of passive-optical and laser measurements. For this, first the problem of acquisition and detection of LEO objects with passive optical systems shall be analyzed. Later on, bringing those systems together will be examined.

Chapter 3

Simulations with PROOF2009

In this chapter, the results of the simulations performed with PROOF 2009 are presented. A short introduction to PROOF has already been given in 1.3. For more detailed intormations, please refer to [7] and [26]. At first, the DLR Space Debris Observatory under construction in Stuttgart is introduced and several sets of simulations to estimate the possible performance of this station are undertaken. To get a better insight into the general possibilities of such a station, in the following simulations for a scaled station and stations dispersed on the globe are performed and the results presented. At last, an overview of the yielded results are given.
Note that at this point, for all the results only the general visibility of the objects is considered.

3.1 Simulations for Stuttgart passive optical observatory

The first sets of simulations were conducted to determine the possible performance of the passive optical space debris station at Stuttgart Uhlandshöhe. In the following, the basic parameters of this station are given, followed by the yielded results and a discussion of those.

3.1.1 The DLR Space Debris Observatory

The observatory is based at the Schwäbische Sternwarte in Stuttgart Uhlandshöhe [1]. The actual position in geodetic coordinates (WGS-84) is shown in table 3.1.

[1] www.sternwarte.de

Table 3.1: Geodetic position of the DLR Space Debris Observatory at Stuttgart Uhlandshöhe.

Parameter	Value
geodetic latitude β [°]	48.7834
geodetic longitude λ [°]	9.1917
height [m]	351.1

Telescope As telescope, the PlaneWave CDK17 was chosen. This telescope is a corrected Dall-Kirkham type. The beampath of such a system is shown in figure 3.1 below. A big advantage of these is the near diffraction limited spot size and coma free image available over a large image plane. Using an additional available focal reducer[2], a focal ratio up to f/4.49 provides a large field of view at reasonable costs. Basic characteristics of the telescope are given in table 3.1.1, both for the standard setting as well as for a setting with the focal reducer. Note that the reducer can be used for different set-ups, shown is the set-up used later for the simulations.

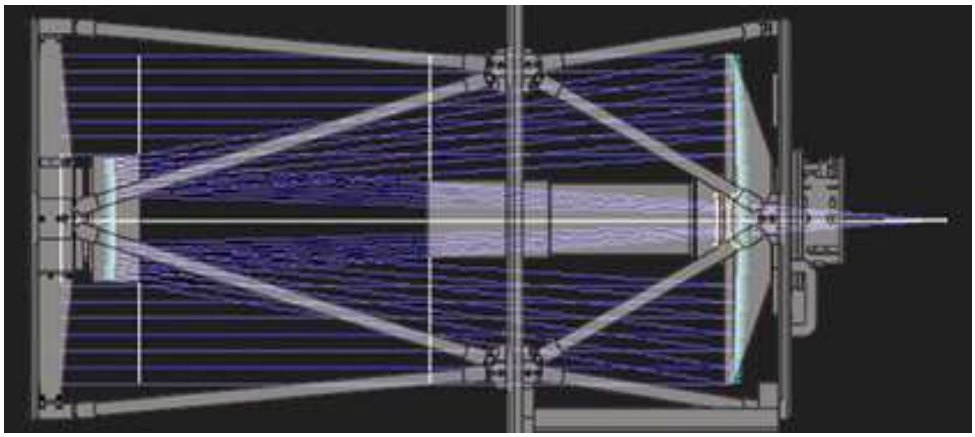

Figure 3.1: Beam path in a corrected Dall-Kirkham telescope [27].

[2]A focal reducer reduces the focal length of an optical system and thus enlarges the field of view

Table 3.2: Optical performance of CDK 17 telescope [27].

Parameter	**standard**	**with focal reducer**
aperture (incl. obstruction) $[mm]$	432	
aperture (corrected) $[mm]$	395.6	
focal plane, $\varnothing[mm]$	52	
focal length $[mm]$	2939	1939.68
focal ratio $[-]$	$f/6.8$	$f/4.49$
optical performance	6.5 μm, 21 mm off-axis	7.3 μm
	9.6 μm, 26 mm off-axis	

Cameras The second simulated piece of hardware is the camera. This has been done for three different ones: The Finger Lake Instrumental Pro Line 16803 (from now referred to as FLI camera), the ANDOR DU 897 Ultra (Andor camera) and an assumed 'perfect' camera. The first two are available at the DLR in Stuttgart, the latter one is used as a reference for comparison. The technical values for all three cameras are given in the paragraphs below.
The needed inputs for simulating a camera in PROOF are summarized in table 3.3.

Table 3.3: Inputs needed by PROOF2009 to simulate a camera.

Input	short description
field of view [°]	describes the solid angle visible on the chip. Depends on the telescope and the size of camera sensor
number of pixels per row [−]	the number of pixels per row. PROOF always assumes square chips
pixel size [μm]	edge size of a pixel
scale [$arcsec/pix$]	the field of view for every single pixel
FWHM [pix]	the resolution of the telescope on the chip. Value from telescope has to be adopted for actual pixel size
integration time [s]	time, the chip is exposed to light
gap time [s]	time between two images, where no illumination takes place (i.e. read out times ...)
CCD read out noise [e^-/pix]	Number of erroneously read electrons per pixel during read out
dark noise [$e^-/pix/s$]	Dark noise electrons per pixel per second. Basically happen due to thermal influence on the sensor
Quantum efficiency [−]	Describes the efficiency of the chip to detect photons at certain wavelengths. Input is done via *.ccd file

FLI PL 16803 camera The FLI camera is a standard interline CCD camera, commonly used in the astrophotographic community. At this point, no further description of the basic working of CCD cameras shall be given. This camera has been chosen because of two reasons: First, it offers a perfect chip size for the to be used telescope. The chip itself has exactly the size of the inner square of the focal plane of the telescope, thus it can cover a large field of view. The second reason is the pixel size: With a spot size (or resolution) of the telescope being $6.5\mu m$ at the outer border of the chip (compare table 3.1.1), the telescope's spot fits completely on one pixel (under perfect conditions). A disadvantage of this camera, as with most astronomical cameras, is the long read out time, which comes both from the high resolution and the suppression of read out noise. Due to this high read out time, during long time observations high gap times

will have to be accepted.
Some of the inputs first have to be calculated, because they depend on the combination of the chip and the camera. The field of view for the chip can be determined via

$$FOV = \frac{S \cdot 57.3^\circ}{f}, \tag{3.1}$$

where S is the length of a side of the chip, f is the focal length of the telescope, and 57.3 accounts for conversion in degrees. From this, the pixel scale, the field of view per pixel, can be determined, which is straightforward:

$$\lambda = \frac{FOV[arcsec]}{n[pix]} \tag{3.2}$$

with n being the number of pixels per edge. All other inputs are basically given by the manufacturer. Note that some of them change depending on the case to be simulated.

Table 3.4: Basic inputs for FLI camera [28].

input	**standard**	**/w focal reducer**
field of view [°]	0.7018	1.089
number of pixels per row [−]	4096	
pixel size [μm]	9	
scale [$arcsec/pix$]	0.6323479	0.9571
FWHM [pix]	1.06667	0.8111
integration time [s]	0.02 [1]	
gap time[s]	2.097 [2]	
CCD read out noise [e^-/pix]	9	
dark noise [$e^-/pix/s$]	3	

[1] minimum exposure time, maximum resolution
[2] minimum read out time, maximum resolution

As last input, the quantum efficiency is needed. The quantum efficiency describes the ability of the chip to detect protons at certain wavelength. This one in shown together with the quantum efficiency of the Andor camera in figure 3.2.

Andor iXon DU 897 Ultra camera The second chosen camera is the Andor camera. This camera is an electron multiplying CCD camera. These cameras are combinations

of low noise interline CCD with an inherent gain register to amplify the photoelectrons before the read out circuit. Due to this amplification, single photon detection can be reached. But together with this process, an additional noise factor is created. This is why the optimal field of use of these kind of cameras is found for very low photon fluxes in combination with high frame rates. The additional noise factor can also be interpreted as a QE loss compared to other digital imaging techniques. The original QE of > 90 % will be reduced to an equivalent QE of about 45%. The high orignal quantum efficiency is yielded by using back illumination technology for the chip. The pixelsize of this camera is larger compared to the FLI camera. This leads on the one hand to a worse ratio of spot size to pixel size, on the other hand it extends the flyover time of a single object per pixel. A current disadvantage of this chip-technology is the very small chip, leading to a small field of view and hence less particles crossing it during an observation campaign. Current developments gain to extent these, but are not available yet [29]. Most inputs again are given by the manufacturer, or have to be calculated as shown in paragraph 3.1.1. Just, the equivalent values have to be determined to account for the effects of the amplification:

$$eN_{read} = \frac{N_{read}}{M} \tag{3.3}$$

with M being the gain which is 255 for the used camera, and

$$eQE = \frac{QE}{F^2} \tag{3.4}$$

with F being the noise factor, which is typically $F = 1.4$ for emCCD cameras. This leads to the general inputs values stated in table 3.5. The low gap time is due to the possibility of the camera to first switch the read image to a secondary slot and then read it from there.

Table 3.5: Basic inputs for Andor camera [30].

input	**standard**	**/w focal reducer**
field of view [°]	0.15986	0.2421
number of pixels per row [−]	512	
pixel size [μm]	16	
scale [$arcsec/pix$]	1.1242	1.7023
FWHM [pix]	0.40625	0.4563
integration time [s]	0.01 [1]	
gap time[s]	~ 0	
CCD read out noise [e^-/pix]	0.3843 [2]	
dark noise [$e^-/pix/s$]	0.006	

[1] minimum exposure time, maximum resolution

[2] equivalent value

The quantum efficiencies, both equivalent and 'normal' are shown in figure 3.2.

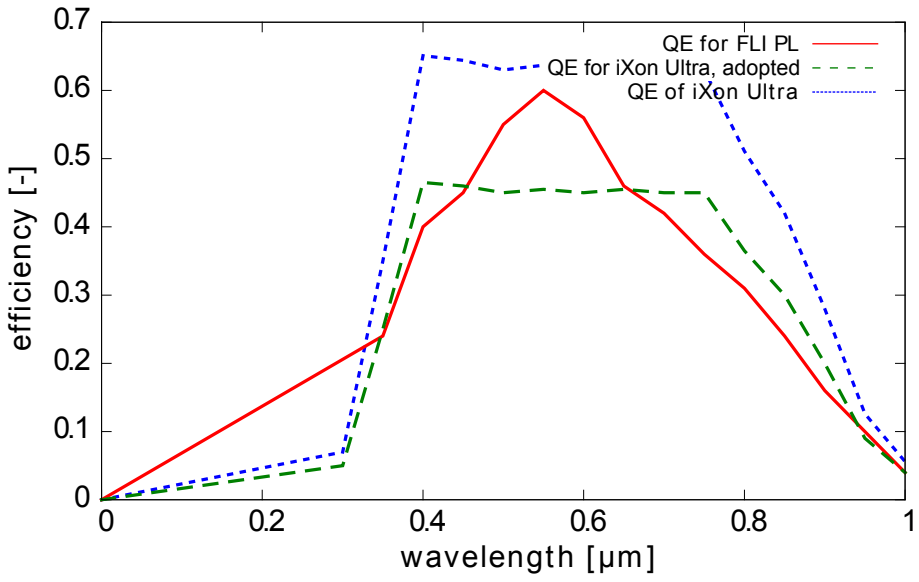

Figure 3.2: Quantum efficiencies for FLI and Andor cameras. For Andor camera, effective values have been used.

Perfect camera The term perfect camera refers at this point to a camera with a large chip, adequate large single pixels and no noises. This camera is only theoretical and to be used as a reference to put the results in a reasonable overall context. Furthermore,

the quantum efficiency is set to 1 over all wavelengths. The inputs are stated as before in table 3.6

Table 3.6: Basic inputs for the perfect camera.

input	**value, standard**	**value, focal reducer**
field of view [°]	0.7806	1.1816
number of pixels per row [−]	2500	
pixel size [μm]	16	
scale [$arcsec/pix$]	1.12417	1.7016
FWHM [pix]	0.40625	0.4563
integration time [s]	0.01	
gap time[s]	0	
CCD read out noise [e^-/pix]	0	
dark noise [$e^-/pix/s$]	0	

3.1.2 Inputs

For the DLR Space Debris Observatory, all simulations have been performed with the same basic inputs. As a reference day, May the 1^{st} has been chosen. For this day, the newest MASTER population is available and thus propagation times during processing can be kept to a minimum. Simulations at other days have used the population files corresponding to their epoch. For clearer analysis of the results, the resolution of single objects is enabled within the software. Additionally, all runs have been performed with 15 Monte Carlo runs, to smoothen statistical artifacts. The hardware was simulated as described in section 3.1.1. In most simulations, all three described cameras (Andor, FLI and perfect) were simulated. While most of the inputs are defined by the given hardware, the integration time (exposure time), has to be chosen to fit to the purpose.

Integration times To gain an optimal signal-to-noise-ratio (SNR), one would always integrate as long as one objects is over one single pixel. During further exposure time, only noise from background and other sources would be collected. The driving factor for the time over a single pixel is the current angular velocity of the object. This angular velocity depends on the linear orbital velocity of the passing object and the distance of

the objects to the observer. It can be calculated via:

$$\omega = \frac{v}{\rho}. \tag{3.5}$$

In here, ω is the angular velocity, v is the linear orbital speed of the object and ρ is the distance, or slant range, from the observer to the object. The linear speed can be calculated with basic orbit mechanics, the slant range depends on the actual viewing direction of the observer. When staying in the orbital plane, thus examining this problem as a 2-dimensional one, it is described by

$$\rho = \sqrt{r_{sat}^2 - r_{\oplus}^2 cos^2(h)} - r_{\oplus} sin(h), \tag{3.6}$$

with ρ being the slant range, r_{sat} the geocentric radius of the satellite, $r_{\oplus}$ the Earth's radius and h the elevation angle. This simple approach has been applied to determine the pixel illumination times for all three cameras for an object on a circular orbit with 1000 km radius. The illumination times can now be calculated from the angular velocities and the field of views per pixel. The result of this is shown in figure 3.3. In there, the single illumination times for the different cameras with and without focal reducer are shown. The perfect camera is not shown because the results for this one are nearly the same as for the Andor camera (due to the same pixel size).

The results lie in here between 4 ms for the Andor camera with focal reducer at very low elevation angles and 0.5 ms for the FLI camera without focal reducer. These values are below the minimum integration times (which are 10 ms or 20 ms), so for the simulations the integration times are set to the minimum.

3.1.3 Determining the performance of the DLR Space Debris Observatory

In this section, the performance and expectations achievable with the Stuttgart based station shall be described. For this, several simulations have been performed with the inputs as described above. Furthermore, the system has been changed using the focal reducer. Most interesting values at this time of analysis are the minimum size of detectable objects, as well as the number of particles, the influence of the observation time during the year, and the times in the night when observations are possible. Step by step, the results shall be shown.

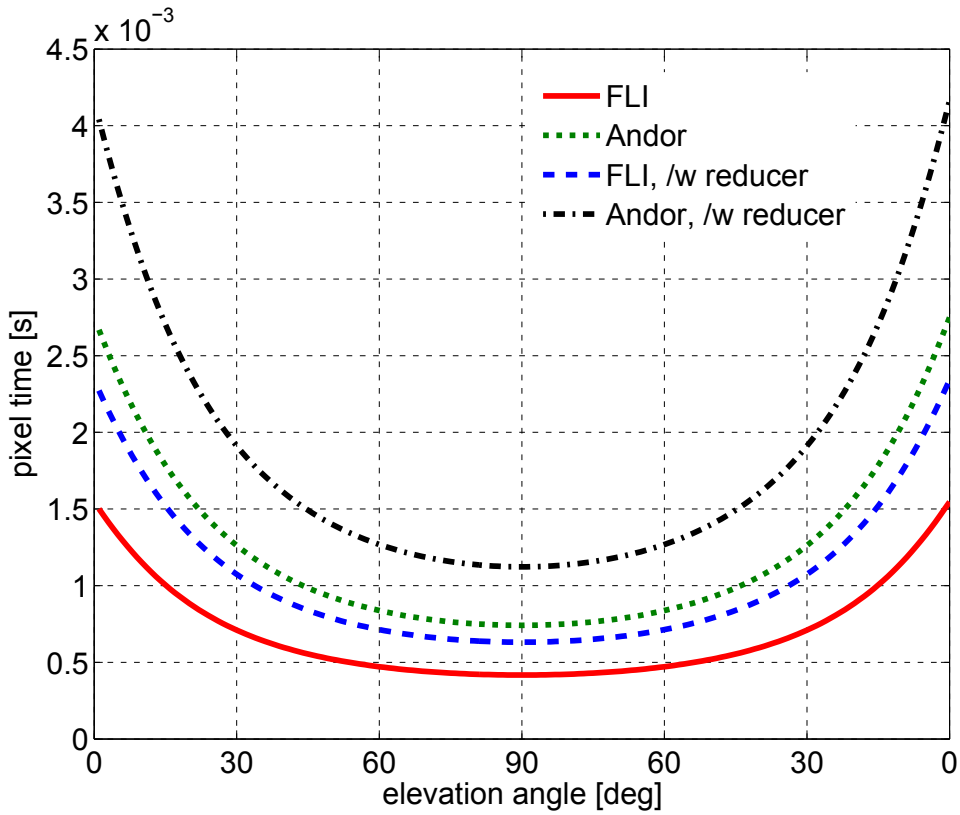

Figure 3.3: Pixel illumination times, object on 1000 km circular orbit.

Minimum size of detectable objects

The first important value is the size of the minimum particle that is visible from the site. For this, several simulations of one night with all cameras have been performed. This value is also important for running following simulations, as the minimum particle recognized during simulations strongly influences the computation time.
The simulations have been run with the basic inputs as described in section 3.1.1, both for the telescope with and without focal reducer and for several different dates. Furthermore, the integration time has been changed in all simulations to get an impression of the influence of integration time on the minimum particle size.
As results, the sizes of detected particles compared to all crossing particles for different integration times for the Andor camera are shown in the figure 3.4 below, results for other cameras are given in the appendix in D.1 and D.2. Because of very similar results, only those yielded for the reference day and the telescope without focal reducer are shown.

For a better overview, the final results, regarding the smallest detected particle, are summarized in table 3.7.
The results lie in the expected range: Due to its high sensitivity, the Andor camera

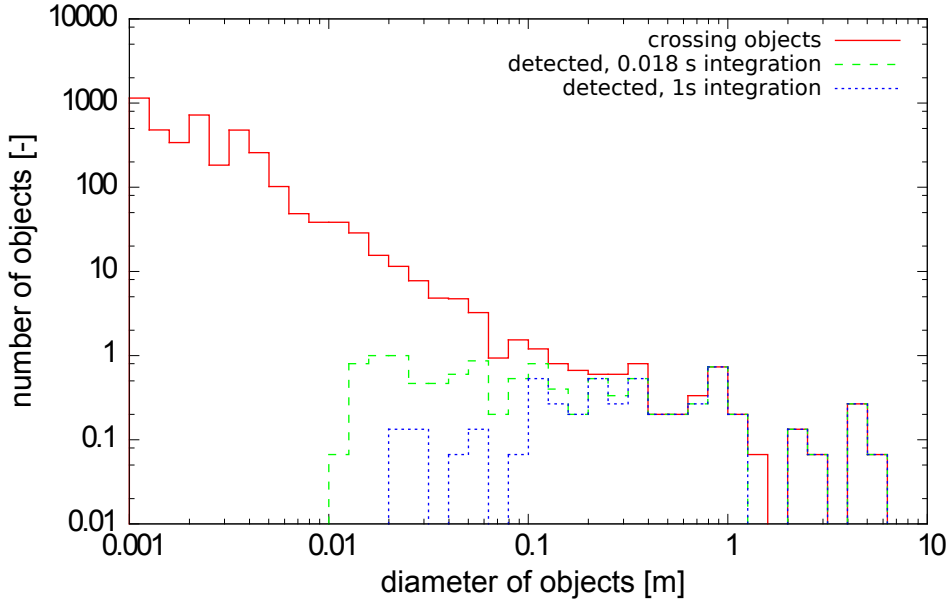

Figure 3.4: Detected particles versus size for Andor camera without focal reducer at Stuttgart site on 1st of May 2009; simulation over one night.

Table 3.7: Results: Minimum size of detected particle for different cameras without focal reducer at Stuttgart site on 1st of May 2009; simulation over one night.

	diameter of detected particle [m]	
camera	**standard**	**/w focal reducer**
Andor [$t_i = 0.01$ s]	0.01870	0.0103
FLI [$t_i = 0.02$ s]	0.21600	0.143
perfect [$t_i = 0.01$ s]	0.00814	0.008

can detect particles down to the near centimeter range. The FLI camera detects objects down to one magnitude larger than the Andor. Also, due to the low sensitivity, with this camera changing the integration time does not change as much as for the other cameras, with one second integration time even slightly smaller objects are detected. The perfect camera detects smallest particles down to sizes of less than one centimeter. As mentioned before, the changing of the minimum detected objects with the integration time can be explained with a changing SNR. With increasing integration time (exposure), the chip collects more background and other noises and thus, the SNR decreases. In the given results, it seems like the camera with focal reducer detects smaller particles than without. This effect is only achieved by more crossing particles and thus also more detectable particles passing the field of view. When looking at all the yielded results, no difference is seen.

To drastically reduce the computation times, from now the recognized particle size in the simulations is set to the achieved results here (compare 3.7).

Number of detectable particles

Another very important aspect for a space debris surveillance station is the number of particles one can discover passive optically. Again, as basic set ups, the inputs described in section 3.1.1 were taken. Deviations from these are stated with every run. As the number of detected particles depends highly on the viewing direction and the season the observation is performed, the simulations have been split up into these two different topics. The results shown are valid for one day, thus two twilights (once in the morning, once in the evening).

Number of detected particles depending on the line of sight This analysis has been performed by changing the azimuth and elevation in every single run; the elevation is always changed in steps of 10° from 10° to 90°, the azimuth was changed in steps of 30° from 0° to 330°. This leads to a total amount of 108 runs. Furthermore, the simulations have been performed for all three camera set ups, with and without the use of the focal reducer. An exemplary result of this is shown in figure 3.5. For this figure, data from five simulations in the beginning of May 2009 has been averaged.

Looking at these results, one clearly sees a dependency of the number of detected particles on the viewing direction. Simulations with the FLI and the perfect camera show similar results, just that with these cameras the total number of detected particles is greater. Maximum, minimum and average values are summarized in table 3.8. The results for FLI and perfect camera are shown in the appendix. Please note that due to the very high procession time of FLI and perfect camera (due to the large fields of view) these simulations only have been performed for single days and are not averaged. But because of the resolution sampling of objects and the high amount of Monte Carlo runs, these results are still statistically relevant.
The same simulations have been performed using the focal reducer. The results are very similar to those achieved without focal reducer, but because of the wider field of view, the total number of particles is much higher. The results for the preferable lines of sight for each simulation set are shown in table 3.8, figures are given in the appendix for all cameras. (figures D.5 to D.7)

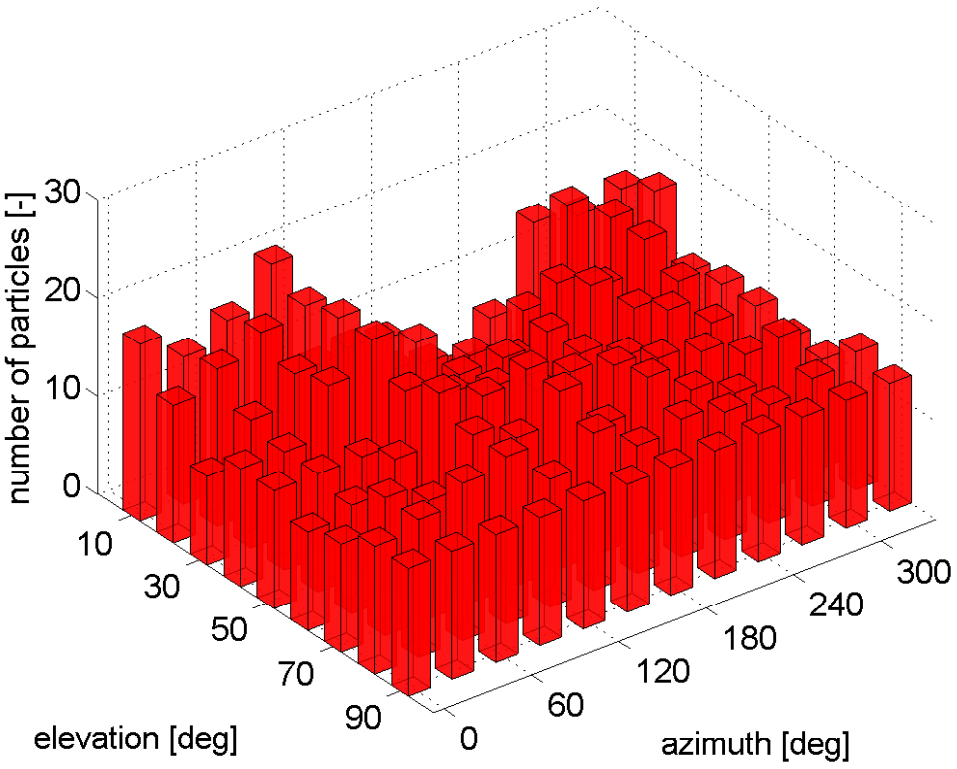

Figure 3.5: Number of detected particles over direction for Andor camera without focal reducer at Stuttgart site, averaged over 5 nights in beginning of May 2009; each simulation over one night.

Table 3.8: Results: Maximum, mean and average number of detected particles for different cameras with and without focal reducer at Stuttgart site on 1st of May 2009; simulation over one night

camera	max. number particles	min. number of particles	average
Andor [1]	20.8	2.8	12.713
FLI	28	3	11.5926
perfect	57	5	36.5278
Andor /w focal reducer	37	3	23.62
FLI /w focal reducer	50	6	24.18
perfect /w focal reducer	104	13	73.8

[1] averaged over five days in beginning of May

Before analyzing these results in more detail, first the change of the detectable particles over the seasons is shown.

Number of particles depending on season For this analysis, the same simulations as already in the paragraph before have been performed, but this time for different dates. As dates the 1st of February 2009, 1st of November 2008 and 1st of August 2008 have been chosen. This is because of population files from MASTER being available for these dates and thus propagation times can be reduced. Looking at the results of these simulations, it can be seen that basically two different distributions are achieved: One for the summer (which are May and August), and one for the winter (which are November and February). The summer-distribution was already shown in figure 3.5. For winter, figure 3.6 gives the results yielded with the Andor camera during February 2009. Results for the other months and cameras are again given in the appendix (figures D.8 to D.15).

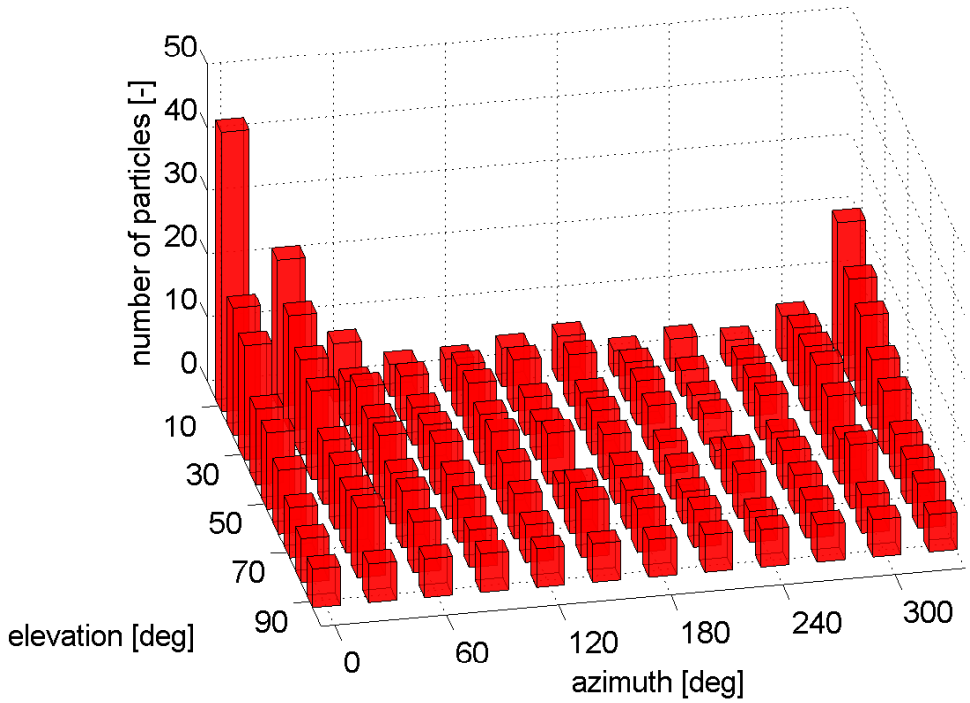

Figure 3.6: Number of detected particles versus viewing direction for Andor camera without focal reducer at Stuttgart site on 1st of February 2009; simulation over one night.

Looking at the figures, it clearly can be seen that that line of sight, where the maximum number of particles is detected, changes over the year. To sum up, the these lines of sight at different seasons are given in table 3.9.Their change throughout the year is reasoned by the changing position of the sun over the seasons.
Furthermore, also the total numbers of detected particles differ a lot over the seasons. The results for maximum, minimum and mean number of detected particles during

Table 3.9: Results: Preferable viewing directions for different cameras without focal reducer at Stuttgart site at different dates; each simulation over one night.

camera	date	elevation [°]	azimuth [°]
Andor	May '09	10	90
	February '09	10	0
	November '08	10	0
	August '08	10	270
FLI	May '09	10	90
	February '09	10	0
	November '08	10	0
	August '08	10	270
perfect	May '09	10	90
	February '09	10	0
	November '08	10	0
	August '08	30	270

Table 3.10: Numbers of detected particles for different cameras without focal reducer at Stuttgart site at different dates; each simulation over one night

Simulation	max. number particles	min. number particles	average
Andor, Feb 09	44	3	8.3
FLI, Feb 09	57	4	8.65
perfect, Feb 09	57	5	36.5278
Andor, Nov 08	47	4	9.3
FLI, Nov 08	61	3	8.85
perfect, Nov 08	101	9	38.66
Andor, Aug 08	30	1	13.94
FLI, Aug 08	29	2	10.81
perfect, Aug 08	155	2	69.19

one observation night are given in the appendix in table 3.10. A further discussion of the different amounts of particles over the season is given in section 3.1.4.

Detection times depending on viewing direction A last dependency that was analyzed is the detection time of the first and the last particle during a night. From the results yielded so far one might assume that changing the viewing direction in staring mode also changes the time, when the first or last particle is visible, due to the different illumination. Using this, one could extend the observation time by first looking east (when the sun has just set in the west) and then later turning into west, when the sun is too low to illuminate objects on the eastern sky. Figure 3.7 shows the results of the analysis of such an approach. It can be seen that the viewing direction does not clearly extend the observation time for the simulations conditions in any detectable way. This

is reasoned by the very little section of night sky observable from one site. Due to this, the times of first and last light on objects change only a little. The small amount of objects further amplifies the impact of this effect. Results for other simulation are shown in the appendix. (figures D.16 to D.29).

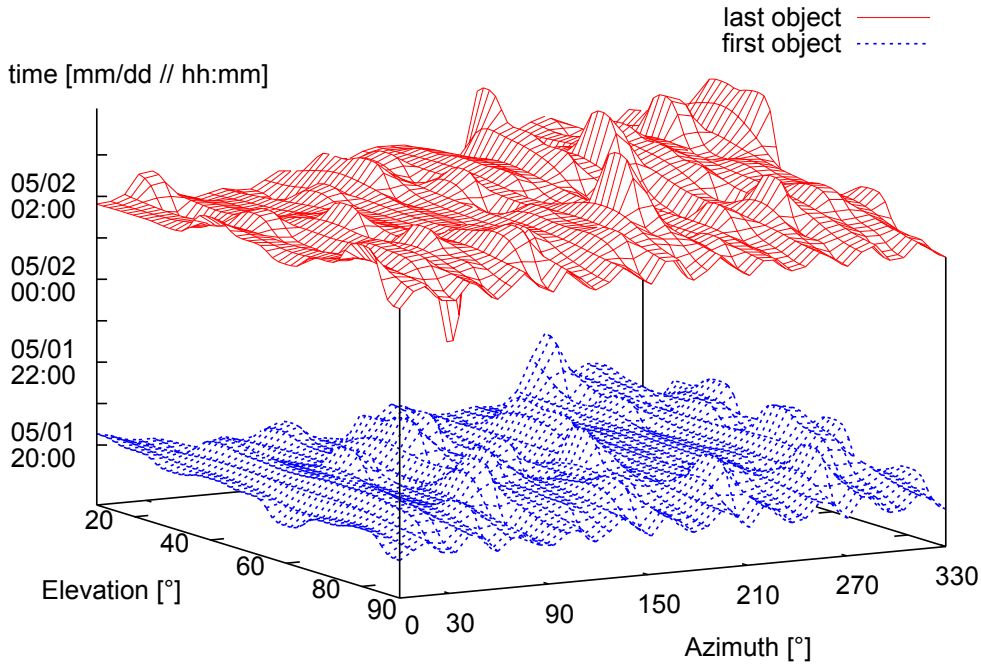

Figure 3.7: Detection times of first object versus viewing direction for perfect camera without focal reducer at Stuttgart site on 1st of May 2009; simulation over one night.

3.1.4 Discussion of the results for Stuttgart station

Above, the results for the performance of the Stuttgart Space Debris Observatory were given. Next step now is to discuss their physical characteristics. For the minimum sized objects this is quite clear, a short but sufficient explanation was given already in section 3.1.3. So the next question is to look behind the numbers of detected particles. The process will be carried out on the results yielded for the reference day (May 1st). Basically, four different factors were made out to be crucial for the results as seen:

- the total number of objects crossing the field of view,
- the range of the single objects during the sighting,
- the phase angle between sun, object and observer,
- the illumination conditions of the object.

These four factor are discussed below. From those, the initial condition to see an object is that there must be one. Thus, the total number of objects crossing is the absolute driving factor.

The total number of objects crossing

The first step towards an explanation is the total number of objects passing through the field of view of a telescope at a given line of sight. Figure 3.8 shows the total number of crossing objects for the Andor camera on the 1st of May 2009, without focal reducer, with sizes over 0.01m, which is set as limit during the simulation (for details about minimum sizes of detectable objects refer to section 3.1.3).

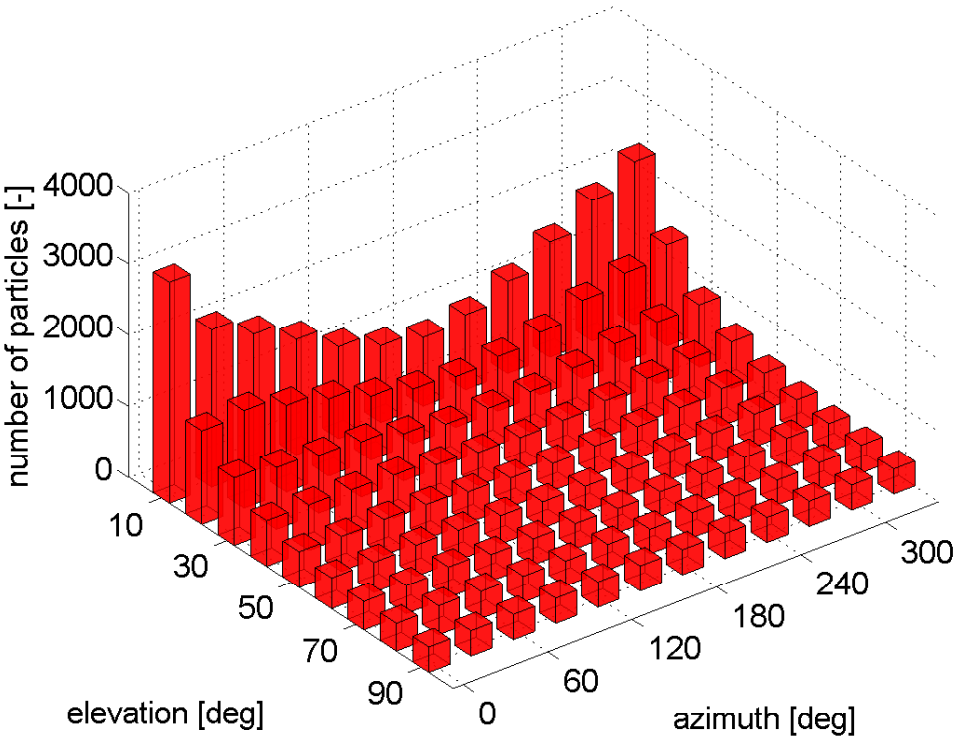

Figure 3.8: Total number of crossing objects versus viewing direction for Andor camera without focal reducer at Stuttgart site on 1st of May 2009; simulation over one night.

It can be seen that in this simulation most objects pass by at low elevations with a total maximum when facing north. Hereby, the rise towards low elevations is reasoned by the larger arc of the field of view for orbits with same heights. This is shown in figure 3.9. Thus, there is a higher chance for an object to be located inside the field of view at lower elevations than at high ones. The rise towards north (or azimuth angles around zero degree) is explainable by the higher spatial density of orbits when facing

there. This is basically due to the large amount of high inclination orbits (i.e. sun-synchronous orbits), which come together close to the poles.

Qualitatively, this output fits to the result as shown in figure 3.5: In general, more

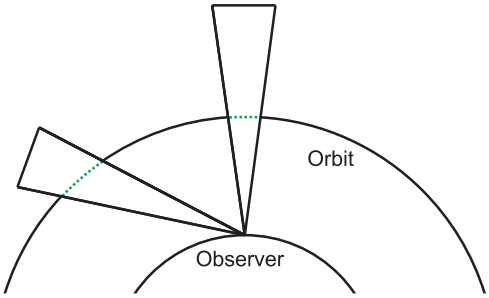

Figure 3.9: Different arcs of the field of view at different object ranges.

objects are detected when staring at low elevations. Quantitatively though, the differences between maximum and minimum detected objects and maximum and minimum numbers of crossing objects do not fit. Furthermore, local maxima and minima of detected objects at certain directions can be observed, which cannot be explained by the number of crossing objects only.

For the next step, figure 3.10 shows the ratio of detected and crossing objects for the same conditions as figure 3.8. Note that in here the perspective is changed to allow a clear overview.

It can be observered that the percentage of the detected objects is conversely to the number of objects passing; the performance regarding the probability to detect an object rises with the elevation. When now assuming that the types of objects is roughly the same over all directions (which should be the case, given the total number of objects), the reason for this must lie within the change of observational conditions changing over the viewing direction. During the following process, this ratio as shown in figure 3.10 will be explained.

To find reasons, below the general detection equation as applied in PROOF is stated. Next to some general constraints, like the Moon or the Sun being in the field of view, the signal of the passing object has to reach a certain threshold. The threshold is described as:

$$T = S_{back} + a\sigma_{S_{back}}. \tag{3.7}$$

In here, T is the threshold signal to be reached, S_{back} is the signal of the background, $\sigma_{S_{back}}$ is the standard deviation of the background signal (as Poisson statistics are applied, $\sigma_{S_{back}} = \sqrt{S_{back}}$) and a a threshold factor, chosen by the user as PROOF input. This means first, the higher the background noise, the less probable is a detection, and second, the higher the signal of the object, the higher the probability to detect the object.

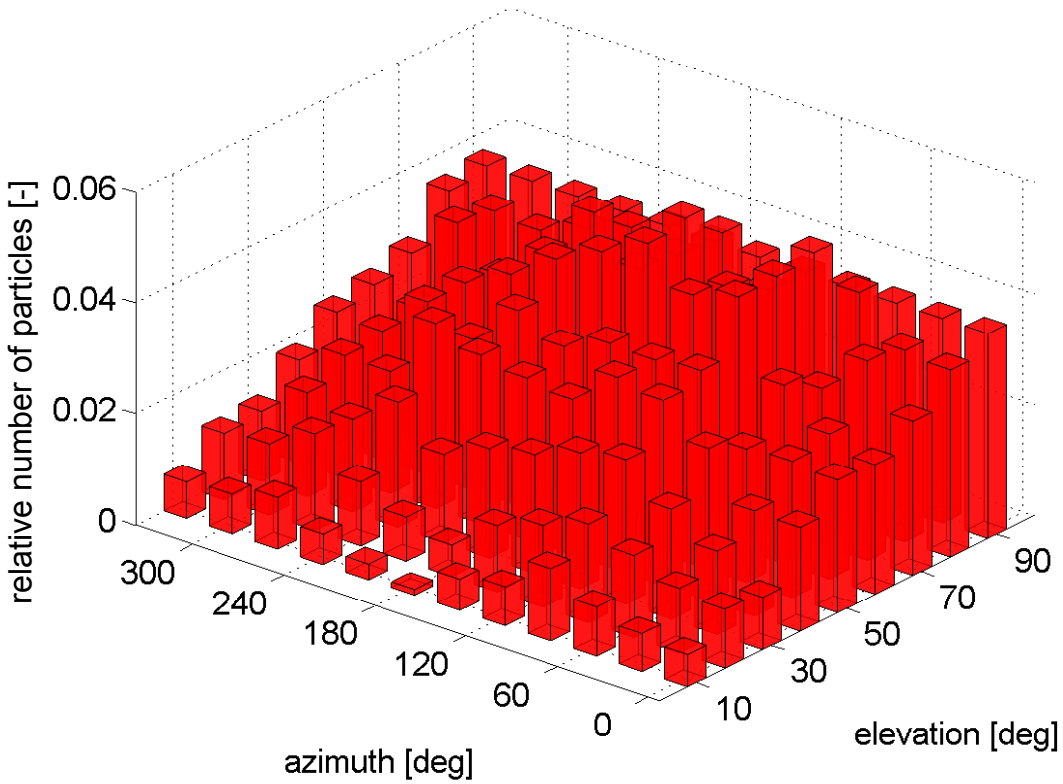

Figure 3.10: Relative number of detected objects versus crossing objects for Andor camera without focal reducer at Stuttgart site on 1^{st} of May 2009; simulation over one night.

Thus, the detection depends both on the signal, received on the objects as well as on the background magnitude. The average background noise is nearly constant over all deducted runs. So this should not be the driving factor. If the noise is not the problem it is probably the signal itself. In PROOF, the radiation H_T received by the telescope is described by:

$$H_T = \frac{E_{rec}\pi r_s^2}{R^2 \cdot 4\pi}\rho_A p(\Theta). \tag{3.8}$$

In here, E_{rec} is the radiation the particles itself achieves from the sun, r_s is the radius of the (debris) object, R the distance between object and observer, ρ_A the reflection coefficient and $p(\Theta)$ the phase function, accounting for the influence of the angle between the object, the observer and the sun. All these factors have a influence on the number of particles one sees in a certain direction. Due to the square influence of the range, it should make largest contribution to the overall signal.

The range of crossing objects

The range R from an observer to a satellite highly depends on the viewing direction, as already could be seen in figure 3.9. It can be described by:

$$R = \sqrt{R_{\oplus}^2 + R_{sat}^2 - R_{\oplus}^2 \cdot cos(h)^2} - R_{\oplus} \cdot sin(h). \tag{3.9}$$

In here, $R_{\oplus}$ is the radius of Earth, R_{sat} is the current height of the satellite above Earth and h is the elevation of the observer. The output of this formula is shown for a circular satellite with an orbit height of $R_{sat} = 1000$ km during a zenith pass of an observer in figure 3.11. This shows that the range rises by the factor of up to 3.5 when going to

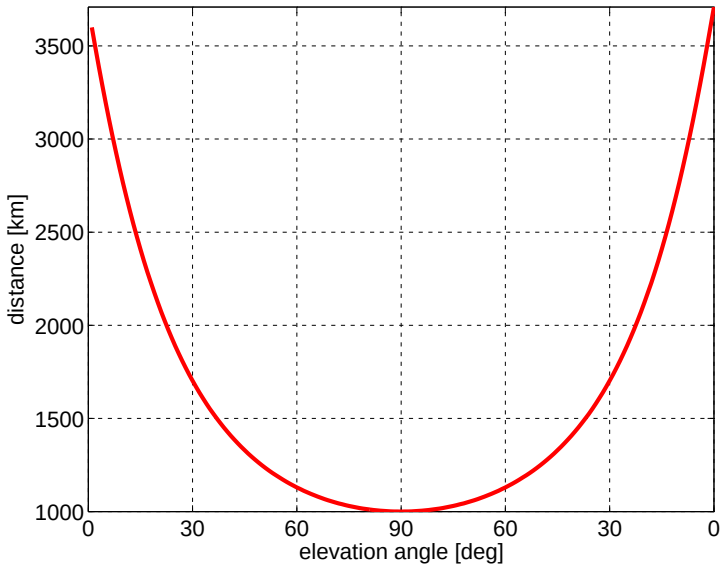

Figure 3.11: Distance versus elevation for a satellite on a circular orbit during a zenith pass.

low elevations. Looking at the results yielded with PROOF, this is also clearly visible (figure 3.12) in those: the average range of crossing objects moves in regions of a bit below 2500 km at low elevations, to a bit above 1000 km at high elevations, what fits very well to the assumption.

The change of the range could explain the finding that the fraction of detected particles is highest towards high elevations: They simply are closer. When now looking back at figure 3.5 one sees that there there is still another function superimposed, leading to certain local maxima and minima. This leads to the last two points, the impact of the direction to the Sun and the illumination by it.

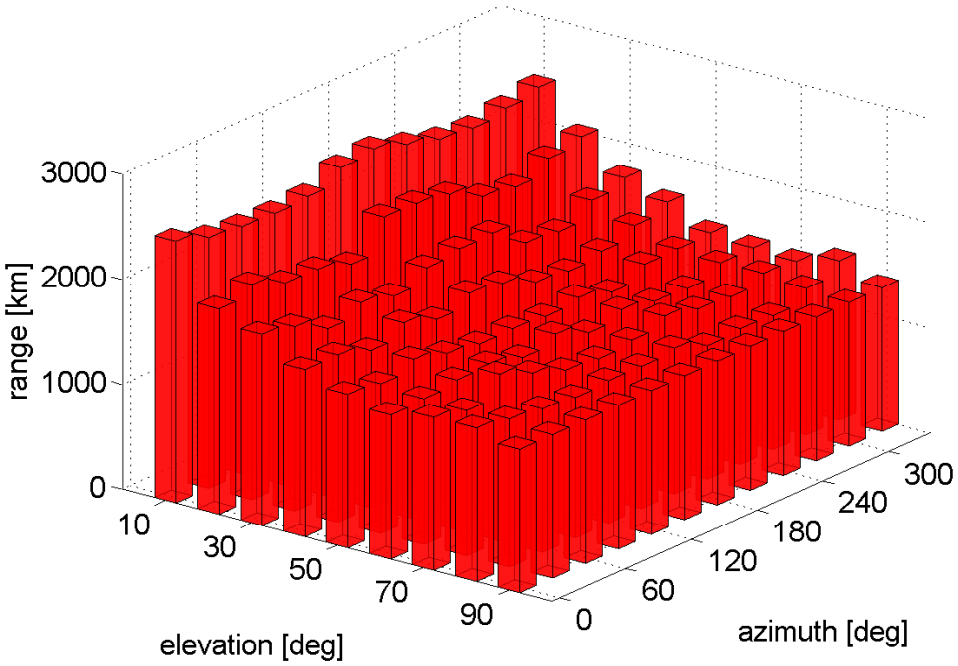

Figure 3.12: Average range of all crossing objects versus viewing direction for Andor camera without focal reducer at Stuttgart site on 1^{st} of May 2009; simulation over one night.

The objects' phase angle and illumination

The maxima in the fraction of detected objects (for the simulations on May the 1^{st}) at middle azimuths (from 90° to 270°) and elevations (from 60° to 80°) do not completely fit to the explanations so far. As will be discussed now they could be explained by the combined influence of the phase angle and the illumination of the object by the sun. The phase angle describes the geocentric inertial orientation of the straight line between the observer and the object. The geometry for this is given in figure 3.13. It can be seen that best conditions are given for low phase angles, giving a 'full object' condition at phase angles of 0°.

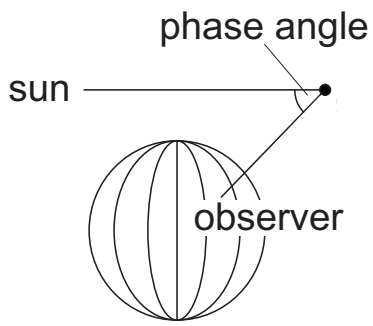

Figure 3.13: Geometry for phase angle definition.

Thus, the phase angle attains best values when it is on the opposite side to the sun, seen from the observer. When the sun is in the north (as during night), best viewing direction, regarding to the phase angle only, would be towards south. Figure 3.10 shows the phase angle of crossing objects for May 1st, where it is clearly to see that southern directions (i.e. azimuth of 180°) lead to smallest phase angles.

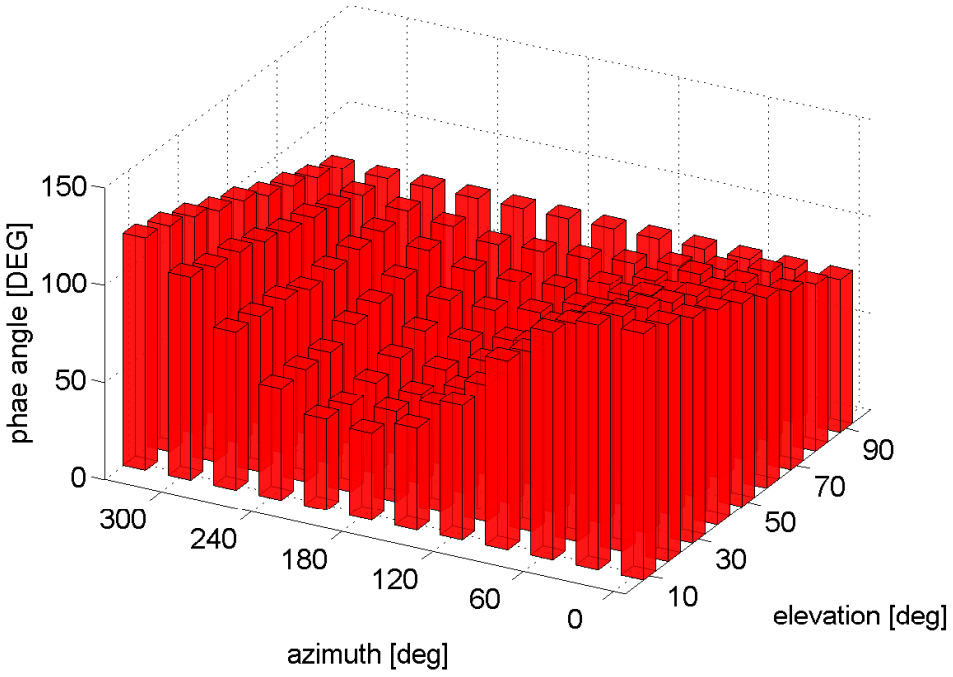

Figure 3.14: Average phase angle of all crossing objects versus viewing direction for Andor camera without focal reducer at Stuttgart site on May 1st of 2009; simulation over one night

The change of the phase angle over viewing direction could explain the rising fraction of particles detected when looking at high elevations and/or middle azimuths, which fits to the maxima. Furthermore, this could be a reason for a higher fraction of detected objects towards east (azimuth = 90°) and west (azimuth = 270°) than towards north, as in those directions the phase angle has lower values.

At last, it has to be described why facing directly south (with low elevation and an azimuth of 180°) yields worst results. This is again to be explained by the position of the sun. While the phase angle gets better, the illumination gets worse when the sun travels on the opposite site of the object. When now looking towards south, with the sun traveling along towards the north during astronomical twilights, objects immerse into Earth's shadow much earlier than for other viewing directions.

Now looking at the results from PROOF for the illumination conditions during the campaign on May the 1st, on sees a severe fall of the illumination on all crossing ob-

jects towards south. This is shown in figure 3.15.

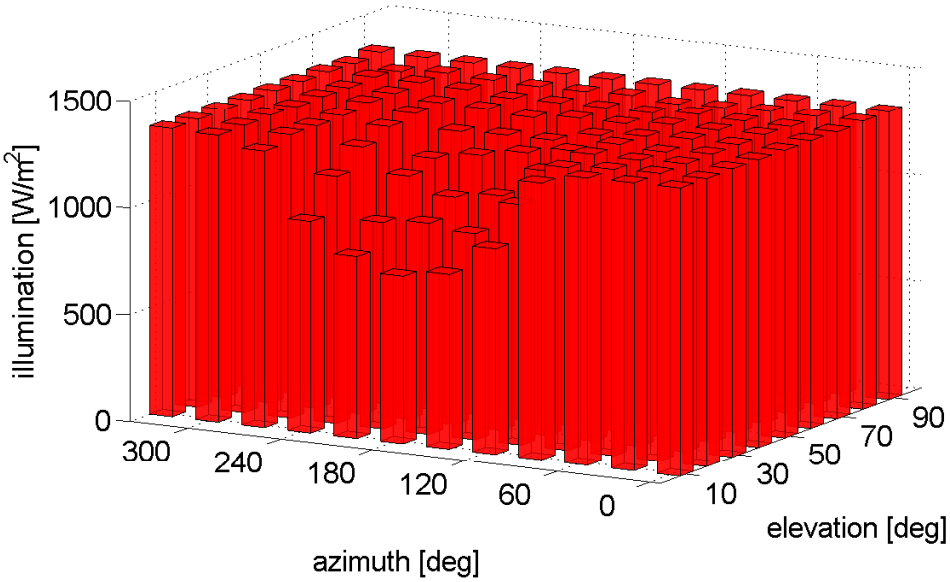

Figure 3.15: Average illumination of all crossing particles versus viewing direction for Andor camera without focal reducer at Stuttgart site on 1^{st} of May 2009; simulation over one night.

Overlaying all the described influences yield the results as seen: First, the number of passing objects is crucial. The fraction of the objects detected from all crossing objects is then determined by observational conditions like the range to the object, the phase angle and the illumination by the sun. To validate this approach, the considered influences have been used to reproduce the irradiation of the objects. During this process, all constants in the irradiation equation as given in equation 3.8 have been set to one. As phase function that one applied in PROOF for spherical objects has been used, which is described by:

$$p(\Theta) = \left(\frac{8}{3\pi} sin(\Theta) + (\pi - \Theta) \cdot cos(\Theta) \right). \tag{3.10}$$

To now also account for the number of total crossing objects, this irradiation distribution was multiplied with the total number of crossing objects. The result of this is shown in figure 3.16.
Comparing this with the distribution of all detected objects (given in figure 3.5) shows a qualitatively good accordance. From these figures one might conduct that with the described approach the main influences have been recognized. Further effects are of course present, like the changing influence of the atmosphere over elevation or camera

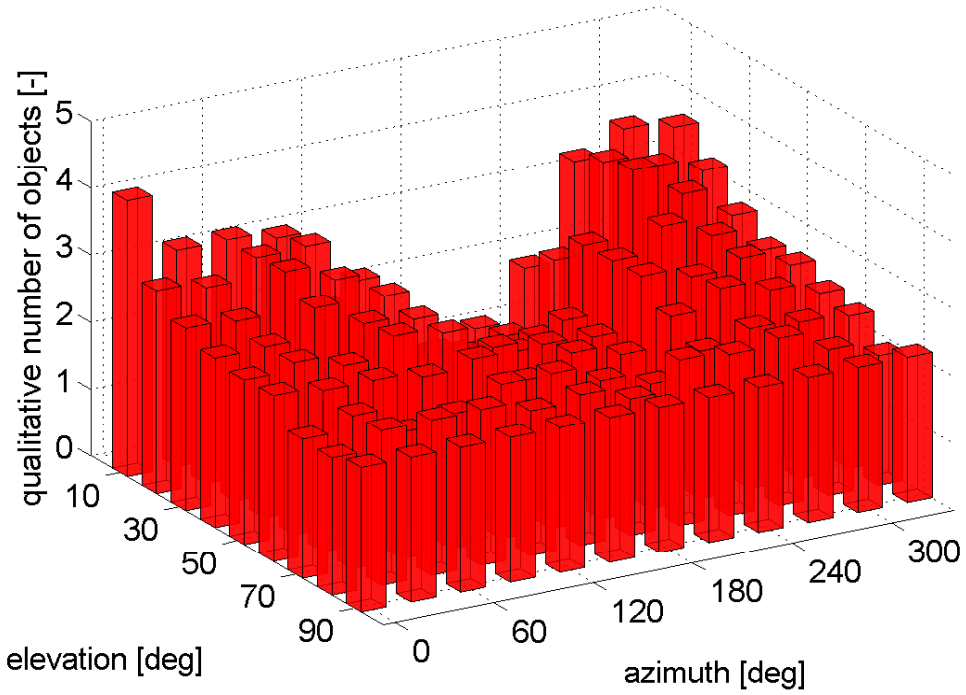

Figure 3.16: Qualitative distribution of detectable objects versus viewing direction for Andor camera without focal reducer at Stuttgart site on 1^{st} of May 2009; simulation over one night. The distribution has been deducted from PROOF outputs with equation 3.8.

issues.

This discussion only treated the case for summer observations. For winter, the same reasons do apply, the associated figures are shown in the appendix (figures D.30 to D.34).

Table 3.11: Results: Total number of detected objects in long term simulations for different cameras without focal reducer on May 1st; simulation over 30 days

objects	Andor	FLI	perfect
detected objects	649	682	1279
different objects	616	567	1196
fragments	76	38	175
NaK-droplets	36	0	146
SRM	0	0	0
TLE-objects	488	513	828
Westford-Needles	0	0	0
MLI	16	16	47

Table 3.12: Results: Total number of detected objects in long term simulations for different cameras with focal reducer on May 1st; simulation over 30 days

objects	Andor	FLI	perfect
detected objects	1078	1305	1993
different objects	1015	1006	1779
fragments	148	61	370
NaK-droplets	97	0	195
SRM	0	0	0
TLE-objects	744	916	1153
Westford-Needles	0	0	0
MLI	26	29	61

3.1.5 Long term simulations for Stuttgart Space Debris Observatory

Another critical point for a space debris surveillance station is the total number of objects and also the number of new and different objects that can be seen throughout a long observation time, which means that 30 days from the given date were simulated. For this, for all cameras, long term simulations have been performed for the same conditions as already simulated before. This means, simulations for all cameras, at four different times, with and without focal reducer have been performed. As the simulations again have been performed in staring mode, as viewing directions the preferable lines of sight given in table 3.9 were used.
The results of these long term simulations are summarized in tables 3.11 and 3.12, for simulations with and without focal reducer, both for May the 1st. Results for simulations at other dates are given in the appendix in tables D.1 to D.3.

In here, again the advantage of a large field of view can be seen, as the FLI camera detects in both simulations slightly more objects than the Andor camera. But when

looking on new objects only (i.e. objects that are non TLE objects), due to its better sensitivity, the Andor camera gains better results. When breaking this down to single observation periods, which are typically one nightfall or one daybreak, one gets roughly 10 objects per campaign (or 20 per night) without focal reducer, or roughly a bit less than double as many with focal reducer.

Table 3.13: Hardware inputs for scaling the field of view. As camera, the Andor camera has been used.

number	textbfField of View [°]	**Aperture [m]**	**focal length [m]**	**pixel scale ["/pix]**
scale #1	0.1	0.4	4.694	0.7031
scale #2	0.25	0.4	1.878	1.7578
scale #3	0.5	0.4	0.939	3.5153

Table 3.14: Detected objects during long term simulations for field of view scaling from Stuttgart in different months. Hardware inputs are given in table 3.13; each simulation was performed for 30 days.

Month	**scale #1**	**scale #2**	**scale #3**
August 2008	334	1022	1868
November 2008	743	2346	3952
February 2009	804	2448	4119
May 2009	354	1078	2010

3.2 Scaling of the used system

So far, only the hardware available for the Stuttgart station has been considered. As this is, especially regarding the telescope and the visible field of view, not of the kind one would use for a final station, this hardware was scaled in two different ways: First, the field of view was enlarged (and thus the focal length reduced) while keeping the other values constant, second, the aperture was changed, while keeping the rest constant to achieve a higher sensitivity of the optical system.

3.2.1 Scaling the field of view

At first, the field of view was changed. This comes together with a reduction of the focal length and, while keeping the camera as before, a growing of the pixel scale. Three different set ups were simulated, the hardware values are given in table 3.13. As camera, only the Andor camera has been used.
The simulations were performed similar to those in section 3.1: First, directions runs have been performed to determine the optimal viewing directions. Not surprising, these are the same as already performed before and shown in table 3.9. Afterwards, long term runs have been performed, to describe the impact of the field of view on the total number of detected objects. The results for this are shown in table 3.14.
The results are as expected, and as also seen before by the use of the focal reducer in the simulations for the DLR Space Debris Observatory: Due to the larger field of view,

Table 3.15: Hardware inputs for scaling the telescope aperture. As camera, the Andor camera has been used.

number	textbfField of View [°]	Aperture [m]	focal length [m]	pixel scale ["/pix]
scale #5	0.16	0.1	2.9338	1.123
scale #6	0.16	0.5	2.9338	1.123
scale #7	0.16	1	2.9338	1.123
scale #8	0.16	2	2.9338	1.123

htp

Table 3.16: Detected objects during long term simulations for aperture scaling from Stuttgart in different months. Hardware inputs are given in table 3.15; each simulation was performed for 30 days. Use numbers for scale #8 with care, as smaller objects than simulated could be detected.

Month	scale #5	scale #6	scale #7	scale #8
August 2008	281	693	1078	1475
November 2008	683	1618	3233	4756
February 2009	721	1659	3393	5011
May 2009	303	732	1109	1563

htp

more objects fly past it, and thus more objects can be detected.

3.2.2 Scaling the aperture

The second scaling was performed by changing the aperture of the telescope. All other inputs were kept unchanged, the most important hardware inputs are given in 3.15. Also here, first direction runs to determine the viewing directions and following long time runs for four different months were performed. As location, again Stuttgart was chosen.
The results of the long term simulations are given in table 3.16. One sees that also enlarging the aperture diameter leads to a growing number of detected objects. While during field of view scaling this was reasoned by simply more objects passing the field of view, in here the reason is that more light can be collected from the same segment of the sky, leading to a higher sensitivity of the whole system regarding to small objects.

This is shown in figure 3.17. In there, also another effect can be seen: Due to the higher sensitivity of the whole system, even objects (in this case only NaK-Droplets) of sizes below 0.01 m can be detected. The simulations were performed only recognizing object down to sizes of 0.01 m, thus the total numbers should only be used considering this.

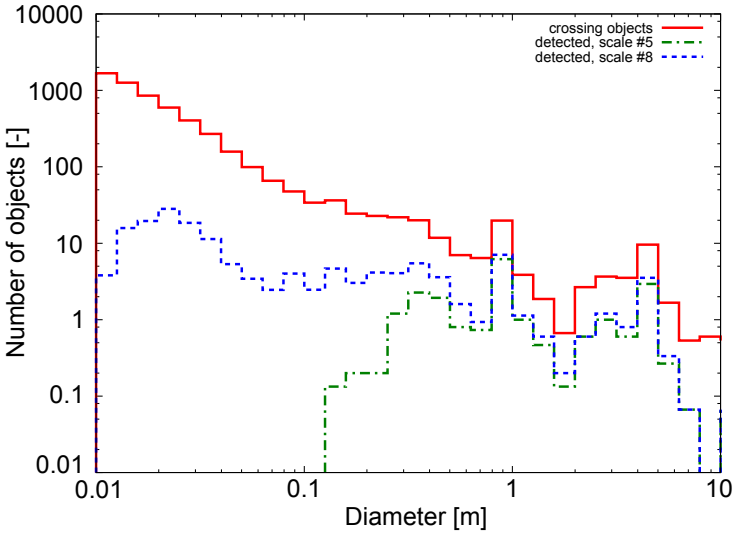

Figure 3.17: Detected objects with different apertures.

3.3 Simulations at other sites

Next, the influence of the location of the station is shown. For this, simulations at different sites over the Earth have been performed and the results will be compared. To take into account for different illumination conditions at different sites throughout the year, all simulations have been performed at four different times during the year, as before during August and November 2008, and February and May 2009. The sites were chosen to assure an equal distribution of sites over the Earth, to have a clear insight on the change of observed objects over longitude and latitude. An overview of them is given in figure 3.18.
As hardware inputs, those for the telescope as described in section 3.1.1, without focal reducer, have been used. As camera, only the Andor camera has been simulated. These constraints were set to keep the simulation times low, as especially larger field of views, as gained by the other cameras and the use of the focal reducer, extend these enormously. Furthermore, as viewing direction only 9 variations were simulated: These were 10, 45 and 90 degree in elevation, and 0, 90, 180 and 270 degree in azimuth (note that elevation of 90 degree is the same for all azimuths). Giving all the yielded outputs would be way too much at this place, thus only a comparison of the possible performance of the Stuttgart station with those at other locations shall be shown.

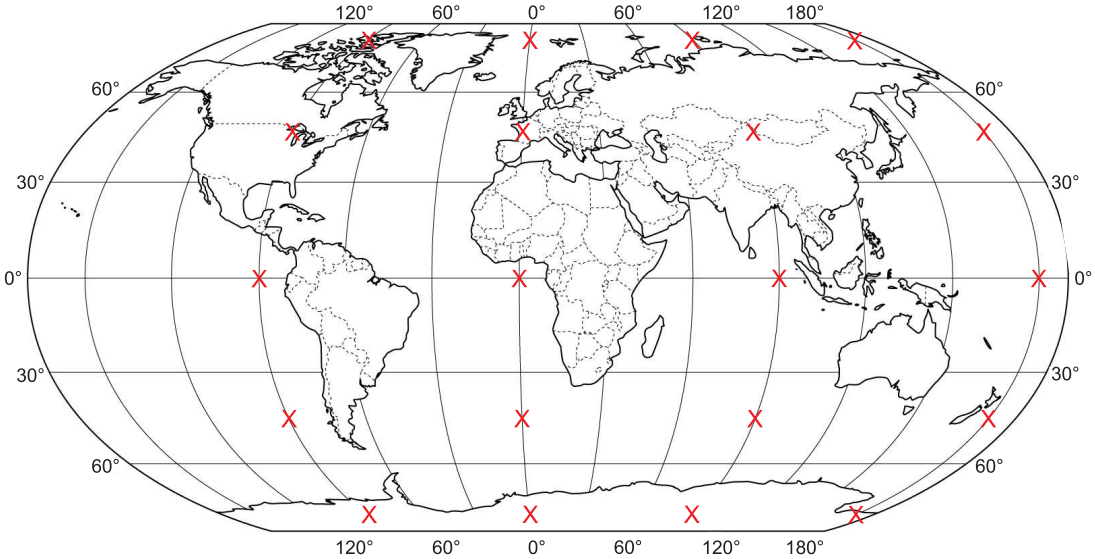

Figure 3.18: Simulated sites over the Earth.

As the single runs were performed for all 20 sites, a first conclusion could be drawn: The number of detectable objects only depends on the latitude, the variations over longitudes are negligible (for this refer to the result tables referenced below). To further analyze the influence of the latitude, from the single runs, the preferable viewing di-

rections (those where most objects were found) were taken and simulated over a whole month (one months in this context always means 30 days, or 720 hours), always only for that longitude with most detected objects. (An overview of the preferable lines of sight and further results from these simulations are given in the appendix in the tables D.4 to D.7.) The results of these long term simulations are given in figure 3.19, compared to the results yielded for the Stuttgart based station. They are shown both for total number, and different number of objects detected.

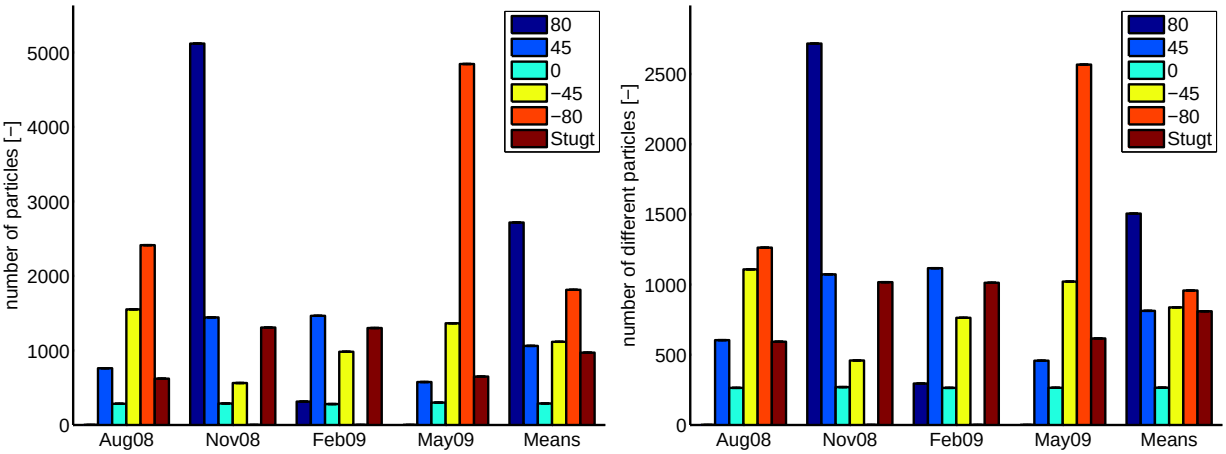

(a) Total objects (b) Different objects

Figure 3.19: Numbers of object per month, different sites.

The results are basically expected: Due to long nights and twilight times in high latitudes close to the poles, in those positions great differences in the numbers of detected objects can be observed over the seasons. Further note that using the focal reducer would nearly double the yielded number of detected objects. In medium latitudes (thus ± 45 degree), the change goes with the seasons, but in general the detected numbers are more constant, but at lower ranges. At the equator, due to very short but equal twilight times, the detection rates are low, but constant. From this, one would conduct that, only referring to the amount of objects, it would be perfect to place stations in the polar regions. Because of the very high variance throughout the year at these stations, for the northern one further simulations have been performed, to see the results for the months in between. The results of these are shown in table 3.17. With those it is obvious that these stations perform remarkable during the summer, but are very inefficient during all the rest of the year, leading to an average number of objects per month that is only slightly above results for medium latitudes.

Table 3.17: Detected objects over one year for a polar station (latitude = 80°). Simulation has been performed for Andor camera without focal reducer, with observations times of 30 days each.

Month	**total number of detected objects**	**number of different detected objects**
January	5321	3250
February	314	295
March	63	56
April	7	7
May	0	0
June	0	0
July	0	0
August	0	0
September	6	6
October	1102	812
November	5120	2717
December	6072	3756
average	1500	908

3.4 Summary of PROOF results

In this chapter, both results for the performance of the Space Debris Observatory in Stuttgart and general dependencies for passive optical sightings have been worked out. These are summarized in short below.

3.4.1 Summary: Results for Space Debris Observatory in Stuttgart

First it was shown that with the given hardware and the Andor camera, it is possible to detect objects down to sizes in the centimeter range (for FLI camera down to sizes of 20 cm). Furthermore, comparing the minimum sizes detected with the Andor camera to those detected with the 'perfect' camera shows that with the Andor camera already a very good performance is achieved (the perfect camera detected a minimum object of 0.8 cm). Following, the optimal staring directions regarding the number of detectable objects were determined. For nearly all runs, low elevations show better results than high elevations. Furthermore, it was found that during summer simulations, most objects can be found when staring east during early summer, and when staring west during late summer. For winter simulations, by far most objects can be detected towards north. Staring south gave worst results in all cases.
Regarding the number of detectable objects, it highly depends on the used setting. When using the Andor camera and no focal reducer, during summer simulations about 20 objects could be detected during one night in summer, and about 43 during winter simulations. Note that these results are only valid for the optimal staring directions. Observations with FLI camera yield slightly higher results (24 during summer, $\approx$55 during winter).
These results could be improved changing the setting: Using the focal reducer roughly doubles the number of detectable objects.

3.4.2 Summary: General results

Additionally to the simulations for the station in Stuttgart, other runs have been performed. In section 3.2 it was shown that the performance, regarding the number of detected objects, can be improved by scaling measures of the optical system: Enlarging the field of view leads to more crossing objects and thus more detected objects, enlarging the aperture leads to a higher sensitivity of the station, leading to more and smaller detected objects.
Regarding the location of a possible station it was shown that in general, higher latitudes lead to more detectable objects, latitudes close to the equator deliver worst re-

sults. As the longitude was found to have no impact on the yielded results, it could be chosen by observational conditions like weather, height etc.
Note that these results are only valid for the number of objects one can see when staring fixed into a set direction.

Chapter 4

Re-detection after initial detection

In the previous chapter only the general sighting of an object was considered. This chapter goes one step further and analyzes the detected objects regarding their further use for tracking and a following orbit determination. For this, first a tool has been written to simulate a sighting and determine the measured lines of sight to the objects from this observation. Furthermore, different methods for the prediction of the future position of the objects have been tested. After, the written tool is used to analyze objects determined to be visible by PROOF directly. From these results, final conclusions regarding the possible passive optical detection are drawn.

4.1 Passive optical re-finding of an object

To analyze the conditions of an object detection and furthermore the re-finding of this objects, the **Pr**ogram for **S**p**A**ce **D**ebris **A**cquisition (*POSADA*) has been written. An overview of the complete program is given in the appendix in image C.1, single subroutines are explained in more detail in the following sections. Aim of this program is to produce the image of a passing space debris object on a CCD matrix and furthermore use the image to determine a prediction for re-finding this object. For this purpose, an user defined object is propagated over the chosen station. While the object is in the field of view of the telescope, a CCD image of the pass is created. After leaving the field of view again, this image is taken to calculate the actual lines of sight from the station to the object. From these, predictions for re-finding the object are calculated for a user defined time and it is checked, if the object can be found. Alternatively, checking the time validity of the predictions is also possible. To ease the whole process, at this point no lighting conditions are considered. This means, if the object is in the field of view, it is assumed to be visible. Furthermore, the object is assumed to be a perfect

spot, thus also the produced image contains perfect spots only.
In the following, the single basic procedures of this program are described. In the scope of the program, a lots of different coordinate systems are used. For a better overview, definitions of the used coordinate systems are given in the appendix (section B).

4.1.1 Needed inputs

To perform this task, several conditions for the sighting have to be defined. In the final program, this will have to be done as inputs by the user. First a sighting and the observing line of sight have to be determined. The general sighting is again found with help of the prior described tool `getSightings` (section 2.3.1). Outputs of this tool are a sighting of the object with a Julian Date in UTC and a state vector in the Earth Centered Inertial TEME coordinate system. This state vector and the epoch are furthermore passed on to the actual tool `POSADA`. Additionally to that, the coordinates of the observing ground station (in WGS-84 coordinates), characteristics of the used telescope and CCD chip and some further inputs for the propagator and analyzing modes are needed. For a full overview, the input file is shown below.

```
##############################################################################################
#                                                                                            #
#                                        INPUT FILE                                          #
#                                                                                            #
##############################################################################################
# First, enter the characteristics of the observing station. Make sure, you station
# fits to the sightings ;)
351.d0                      Height of station, WGS-84, [m], dpSiteHeight
48.7834d0                   Latitude of station, WGS-84, [DEG], dpSiteLat
9.1975d0                    Longitude of station, WGS-84, [DEG], dpSiteLong
1.0d0                       Field of View of the used telescope, [DEG], dpFieldOfView
# NOTE: Real FOV for the chip is calculated from chip size and focal length. This one
# Here should still fit though ;)
1.939d0                     Focal Length of the telescope, [m], dpFocalLength
1024                        Number of pixels in one row, square chip, [-], intPixelNumber
16.d0                       Size (=linear length) of a single pixel, [mum], dpPixelSize
# NOTE: Pixel Scale is also calculated internally, from the real field of view
# Now, enter details of the sighting. Sightings can be determined with help of the
# tool getSightings/posadaSightings. Make sure, sightings fit to the epoch and stuff
-1365451.5729d0             I position of observation, TEME, [m], dpYInit(1)
-3224739.8514d0             J position of observation, TEME, [m], dpYInit(2)
6011922.55606d0             K position of observation, TEME, [m], dpYInit(3)
4628.19392d0                I velocity of observation, TEME, [m], dpYInit(4)
-5631.22515d0               J velocity of observation, TEME, [m], dpYInit(5)
-1961.49625d0               K velocity of observation, TEME, [m], dpYInit(6)
2456094.47986111d0          Julian Date of observation, UTC, [dd,dddd], dpJDInit
# Analysis options
21.d0                       Elevation, where to stare, [DEG], dpElevationStart
60.d0                       Image processing time , [sec], dpFindTime
0                           Flag to choose if linear (0) or square (1) ,intExtraPSwitch
0                           Flag for refraction, [0==off,1==on], intFlagRef
0                           Flag, for use of SEEING
5.d0                     Average seeing ['']
1.d0                        sigma one seeing ['']
# Propagator inputs:
0.01d0                      effective surface of object, [m**2], dpSatA
1.d0                        mass of object, [kg], dpSatM
2.2d0                       drag coefficient of object, [-], dpCd
1.d-9                       relative tolerance of ode solver, [-], set below 1.d-8, dpRelErr
1.d-9                       absolute tolerance of ode solver, [-], set below 1.d-8, dpAbsErr
18                          order and degree of geopotential, max. 70, [-], intMaxOrder
1                           flag, it atm model shall be used, [-], intAtmFlag
low                         the solar activity ('low','medium','shortHigh','longHigh'
##############################################################################################
```

4.1.2 Main routine

The program routine `posadaMain()`is the driver routine of the program. It takes care of setting up generally used constants, file handling and reading of subsequently used values for coordinate transformations, the geopotential, the density model and user

defined inputs. Furthermore, from here the subroutines for getting the staring line of sight and afterwards for the actual passive optical detection are called.

4.1.3 Determination of the telescope's line of sight

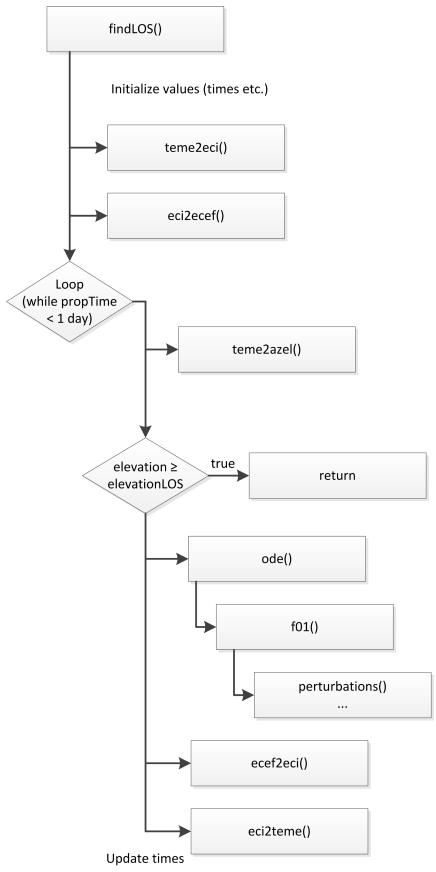

Figure 4.1: Flowchart of subroutine findLOS().

This subroutine determines a suitable line of sight of the telescope for the detection. For this, at first the TEME input vector is changed to ECI coordinates. The process for this is basically taken from [8]. Following, the object is propagated. During this propagation, the current line of sight described by elevation and azimuth is determined. If the elevation of the line of sight reaches the priorly by the user chosen elevation, the propagation is stopped and the current line of sight is set as the telescope staring line of sight. This one is both saved in elevation and azimuth, and for the later image taking as well in ECEF coordinates. For the rotation between ECI and ECEF coordinate systems, subroutines from the SOFA library [18] have been used. As these subroutines can deal with position vectors only, they furthermore have been complemented with transformations for velocity vectors, where basically the rotation of Earth has to be recognized. For propagation, subroutines already described in section 2.2 have been used.

The way of calculating the line of sight by means of azimuth and elevation has already been described in section 2.3.1. Figure 4.1 gives an overview of the flow of this subroutine.

4.1.4 Creating a CCD image

To analyze a passive optical observation, first such has to be simulated. For this, the process of creating a CCD image for analysis is described in the following. It has been implemented in the subroutine `passiveDetecion`, with single steps spread to other subroutines. The general procedure of this subroutine is very similar to the search of the line of sight described in section 4.1.3. Just, this time, instead of checking for

the elevation of the line of sight, a check for the object to be in the field of view is performed.

Checking the field of view

In every propagation step during the passive optical detection, it is checked if the object is currently in the field of view. The process for this is basically taken from the procedures used in PROOF as described in [7] and is implemented in the subroutine `checkFOV()`. For overview, a flow chart of this process is given in figure 4.2.

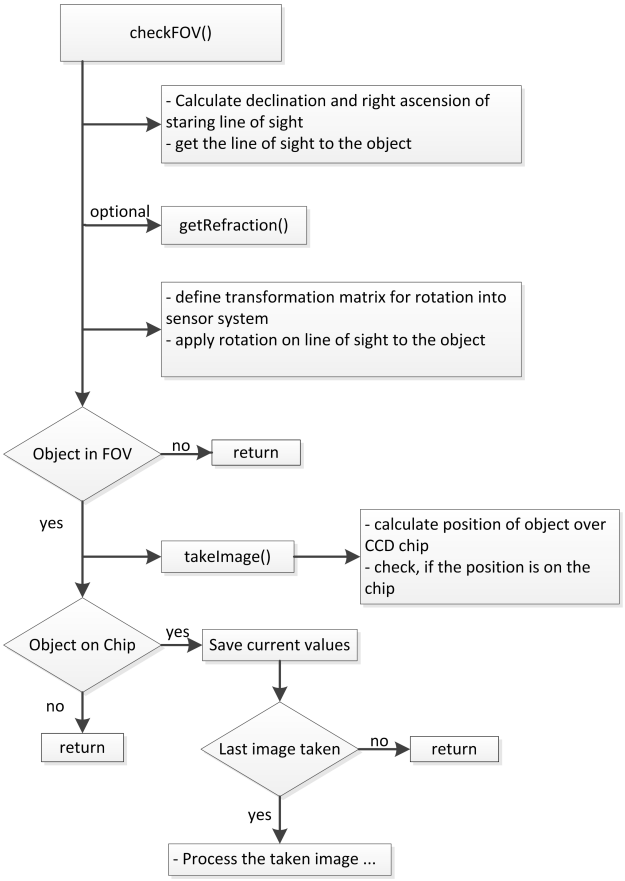

Figure 4.2: Flowchart of subroutine CheckFOV().

At first the right ascension and declination in the local observer system of the telescope's line of sight are needed. This is done via the standard transformation between polar and Cartesian coordinates:

$$\delta_{LOS,TOPO} = arctan\left(\frac{z_{LOS,ECI} - z_{OBS,ECI}}{\sqrt{(y_{LOS,ECI} - y_{OBS,ECI})^2 + (x_{LOS,ECI} - x_{OBS,ECI})^2}}\right),$$
$$\alpha_{LOS,TOPO} = arctan\left(\frac{y_{LOS,ECI} - y_{OBS,ECI}}{x_{LOS,ECI} - x_{OBS,ECI}}\right). \tag{4.1}$$

In here, the subscript *LOS* describes the line-of-sight of the telescope, *OBS* is the observer, *ECI* are coordinates in an Earth Centered (pseudo) Inertial system and *TOPO* describes a locally fixed coordinate system. Note that the subscript *LOS*,*ECI* describes the priorly found line of sight to the object, and thus is actually the state vector of the object for that time when the line of sight as been defined.
Next, the slant range from the observer to the object is calculated. Do not confuse those two different kind of lines of sight: First the staring direction of the telescope, and second the real line of sight from the observer to the object, which is in here denoted as slant range. The latter one is determined by simple vector calculations:

$$\vec{v}_{OBJOBS,ECI} = \vec{v}_{OBJ,ECI} - \vec{v}_{Site,ECI}. \tag{4.2}$$

This vector now defines the position of the object relative to the observer in ECI coordinates. Additionally to that the user can decide to transform this position to the apparent position by applying refraction on the determined line of sight. For the refraction a simple model of the form

$$\zeta_{vac} \approx \zeta_{obs} + A \cdot \tan(\zeta_{obs}) + B \cdot \tan(\zeta_{obs})^3 \tag{4.3}$$

has been implemented. In here, ζ_{vac} describes the real topocentric zenith distance, ζ_{obs} the observed one. A and B are constants that are calculated for certain conditions given at the observation site. This model can be seen as sufficient down to elevations of about 20 to 25 degree. For lower elevations, more sophisticated models would have to be used. The model and the subroutines used to apply it are based on the SLALIB library from [31]. Although it has been implemented in the code, refraction was not used for the analyses in the work.
To determine if the object is in the field of view, the slant range is now transferred into a sensor coordinate system. In this coordinate system, the x-axis is aligned with the line of sight of the telescope, the z-axis is pointing north and the y-axis completes the right handed coordinate system. The transformation is realized with help of the declination and right ascension of the telescope's line of sight as described in equation 4.1, hence:

$$\vec{v}_{OBJ,SENS} = \begin{pmatrix} \cos(\alpha_{LOS})\cos(\delta_{LOS}) & \sin(\alpha_{LOS})\cos(\delta_{LOS}) & \sin(\delta_{LOS}) \\ \cos(\alpha_{LOS})\sin(\delta_{LOS}) & \sin(\alpha_{LOS})\cos(\delta_{LOS}) & -\cos(\delta_{LOS}) \\ -\sin(\alpha_{LOS}) & \cos(\delta_{LOS}) & 0 \end{pmatrix} \cdot \vec{v}_{OBJOBS,ECI}. \tag{4.4}$$

With this vector, one can now determine the field of view of the telescope, as well as the decision, if the object is in the current field of view. For this, first the radius of the circular field of view at the distance of the object has to be calculated as

$$r_{FOV} = r_{\vec{v}_{OBJ,SENS}} \cdot \tan\left(\frac{FOV}{2}\right), \tag{4.5}$$

where $r_{\vec{v}_{OBJOBS,SENS}}$ describes the length of the vector. The radius of the object position in the sensors coordinate system (thus in the y,z-plane of the sensor system) is determined via

$$r = \sqrt{(y^2_{OBJ,SENS} + z^2_{OBJ,SENS})}. \tag{4.6}$$

The crossing decision is then finally defined by two conditions: First, the object has to be above the sensor, thus the x-coordinate of the object in the sensor coordinate system has to be positive. Second, the projection of the object in the y,z-plane of the sensor system has to be in the radius of the field of view at the distance of the object:

$$\begin{aligned} r &\leq r_{FOV} \\ &\text{and} \\ x_{OBJ,SENS} &> 0. \end{aligned} \tag{4.7}$$

If both of these conditions are true the subroutine for taking the actual image is called.

Taking the image

During the passive optical detection, every time the object is in the field of view of the telescope the subroutine `takeImage`is called. This subroutine creates the image of the object on a CCD chip. For this, at first the prior determined slant range between object and observer $\vec{v}_{OBJOBS,ECI}$ has to be transformed into spherical coordinates:

$$\begin{aligned} \alpha_{OBJOBS,ECI} &= arctan(\frac{y_{OBJOBS,ECI}}{x_{OBJOBS,ECI}}), \\ \delta_{OBJOBS,ECI} &= arctan(\frac{z_{OBJOBS,ECI}}{\sqrt{x^2_{OBJOBS,ECI} + y^2_{OBJOBS,ECI}}}). \end{aligned} \tag{4.8}$$

With these, the position of the object above the chip can be determined as described in [7]. First, sine and cosine values of the zenith angle Z (which describes the offset to the line of sight) and azimuth angle A can be determined via:

$$\cos(Z) = \sin(\delta_{LOS})\sin(\delta_{OBJOBS,ECI}) + \cos(\delta_{LOS})\cos(\delta_{OBJOBS,ECI})\cos(\alpha_{OBJOBS,ECI} - \alpha_{LOS}), \tag{4.9}$$

$$\sin(Z) = \sqrt{1 - (\cos(Z))^2}, \tag{4.10}$$

$$\sin(A) = \cos(\delta_{OBJOBS,ECI})\frac{\sin(\alpha_{OBJOBS,ECI} - \alpha_{LOS})}{\sin(Z)}, \tag{4.11}$$

$$\cos(A) = \frac{-\cos(\delta_{LOS})\sin(\delta_{OBJOBS,ECI}) + \sin(\delta_{LOS})\cos(\delta_{OBJOBS,ECI})\cos(\alpha_{OBJOBS,ECI} - \alpha_{LOS})}{\sin(Z)}. \tag{4.12}$$

From these, the actual coordinates in the chip system are calculated:

$$\begin{aligned} z &= \frac{\sin(Z)}{\cos(Z)} \cdot f, \\ x &= -z \cdot \sin(A), \\ y &= z \cdot \cos(A). \end{aligned} \tag{4.13}$$

In here, δ and α are the declination and right ascension of the staring line of sight and the slant range from observer to object respectively. x and y are the positions on the chip matrix, z is the height above the chip (do not confuse the zenith angle Z with the height z). By this, the position of the object in the chip plane is known. Next a check as to be added, to know if the object is really on the chip. In case the chip does not cover the whole image plane of the telescope, this can easily happen. To be on the chip, the two conditions

$$\begin{aligned} |x_{chip}| &\leq \frac{S_{chip}}{2} \text{ and} \\ |y_{chip}| &\leq \frac{S_{chip}}{2}, \end{aligned} \tag{4.14}$$

with S being the edge length of the chip have to be valid. The absolute value of the position and the half length of the chip are needed, as the origin of the chip coordinate system resides in the middle of the chip. If both these conditions are true, the

appertaining pixel to that position is evaluated:

$$\begin{aligned} x_{pixel} &= \text{int}\left(\frac{x_{chip}+S/2}{S/n}\right), \\ y_{pixel} &= \text{int}\left(\frac{y_{chip}+S/2}{S/n}\right). \end{aligned} \tag{4.15}$$

In here, n describes the number of pixels in one direction. At last, the CCD matrix is filled at this point. For a better visualization, the first illuminated pixel gets the value 1, the second a 2 and so on. Note, that no further analyses regarding optical aberrations (e.g. atmospheric turbulence) are performed. The object is considered to be a perfect spot. If the whole image is taken (thus the object has left the CCD chip), the CCD matrix is saved to a file. Such file can be considered as the equivalent of a stack burst of single images.
To this point, the image of a crossing object has been created. Exemplary the thus created CCD image of a GenesisII pass over Stuttgart seen through a 1° field of view telescope with a focal length of a bit less than 2 m, captured on a 512x512 chip with a pixel size of 16μm in the middle of June 2012 is shown in figure 4.3, both with and without refraction. For a better visualization, a cluster of 49 pixels is colored instead of the respective single pixel (during calculations, single pixels are considered). Furthermore, please not that the coloring only gives information about the tracking direction: The pixel travels from gray spots towards bright white ones. The intensity of the single pixels is not considered.

Getting the viewing directions from the CCD matrix

Next step is to find the slant ranges to the object from the CCD image matrix. As with real observations one does not know anything about the object but the just observed spots and some additional data as the staring line of sight and the times when the object has been sighted. To get the viewing directions from the pixels, the process for taking the image from section 4.1.4 is turned around. This has been realized in the subroutine `getViewingDirections`. For this, at first the filled positions of the matrix have to be determined. This is done with the help of simple loops. It has to be noted that this process becomes very inefficient with growing chip sizes. Afterwards, the pixel positions have to be translated into coordinates in the chip frame. As pixel position, always the middle of a pixel is assumed. In here it is important that the chip matrix goes from zero to the total number of pixels, while the zero in the chip coordinate system lies in the middle of the chip (aligned with the staring line of sight

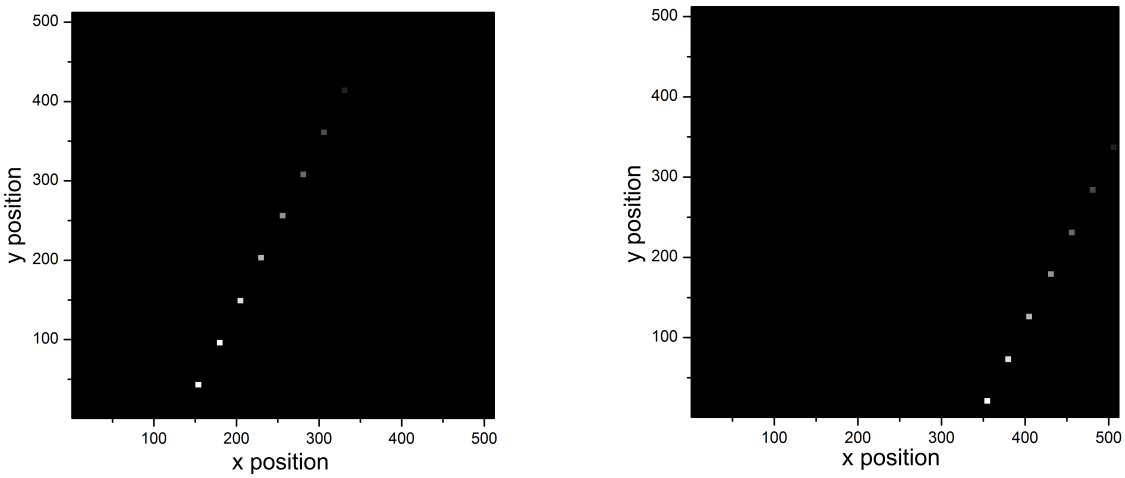

(a) without refraction (b) with refraction

Figure 4.3: Image of Genesis II pass over Stuttgart. The coloring of the spots indicates the travel direction of the object from gray to white.

of the telescope). Thus, for positions in the first half of the chip the actual position in the chip coordinate system is calculated via

$$x_{chip} = -(0.5 \cdot S_{chip} - m \cdot L_{pixel}) - \frac{1}{2} \cdot L_{pixel}, \tag{4.16}$$

and for positions in the second half

$$x_{chip} = m \cdot L_{pixel} - 0.5 \cdot S_{chip} + \frac{1}{2} \cdot L_{pixel}. \tag{4.17}$$

In here, L_{pixel} is the edge length of a single pixel, m is the number of the illuminated pixel on the chip. This process is done separately for x and y positions. Next step is to determine the associated lines of sight to every chip position, using values saved during the observation. These values are the time stamps, the staring line of sight of the telescope and furthermore the focal length of the telescope (f). From these, one can first determine the azimuth (A) and Zenith (Z), in the chip coordinate system:

$$\begin{aligned} A &= \text{atan2}\left(\frac{-x_{chip}}{y_{chip}}\right), \\ Z &= \arcsin\left(\frac{-x_{chip}}{\sin(A)}\right) / f. \end{aligned} \tag{4.18}$$

With these values it is now possible to determine the right ascension and declination

for every chip position:

$$\begin{aligned} \sin(\delta) &= \sin(\delta_{LOS}) \cdot \cos(Z) - \cos(A) \cdot \cos(\delta_{LOS}) \cdot \sin(Z), \\ \cos(\alpha) &= \alpha_{LOS} \pm \frac{\cos(A) \cdot \sin(Z)}{\sin(\delta_{LOS}) \cdot \cos(\delta)} + \frac{\cos(\delta_{LOS}) \cdot \sin(\delta)}{\sin(\delta_{LOS}) \cdot \cos(\delta)}. \end{aligned} \tag{4.19}$$

The sign for the α term hereby depends on the rise or fall of the right ascension, which can be determined from the track of the image on the chip. Note that the pseudo inertial declination and right ascension are determined from the local horizontal staring line of sight of the telescope. Due to the time dependency of the inertial coordinate system, they have to be set up for every image, for the valid observation time stamp. (To do this, just return the process for getting topocentric elevation/azimuth described below).
Now these two angles, which are valid for the ECI frame, still have to be transformed into a local horizontal elevation/azimuth system. For this, one first describes the unit slant range of these angles in the ECI frame

$$\begin{pmatrix} \rho_{I,ECI} \\ \rho_{J,ECI} \\ \rho_{K,ECI} \end{pmatrix} = \begin{pmatrix} \cos(\delta) \cdot \cos(\alpha) \\ \cos(\delta) \cdot \sin(\alpha) \\ \sin(\delta) \end{pmatrix} \tag{4.20}$$

This vector now has to be rotated into the local SEZ system, which means one rotation around the local sidereal time (which is the Greenwich sidereal time plus the geographic longitude) and one around the geographic latitude

$$\vec{\rho}_{SEZ} = \mathrm{ROT2}\left(\frac{\pi}{2} - \phi\right) \cdot \mathrm{ROT3(LST)}\vec{\rho}_{ECI}. \tag{4.21}$$

In this system, azimuth and elevation are defined as

$$\begin{aligned} \mathrm{A}_{SEZ} &= \mathrm{atan2}\left(\frac{\rho_{I,SEZ}}{\rho_{J,SEZ}}\right), \\ \mathrm{h}_{SEZ} &= \arcsin\left(\frac{\rho_{K,SEZ}}{|\vec{\rho}|}\right). \end{aligned} \tag{4.22}$$

Now the lines of sight for every pixel on the image have been determined. They are available both as azimuth and elevation as well as right ascension and declination. As so far the line of sight was always described in azimuth and elevation, these shall be

used for further process.

4.1.5 Refinding the object

In order to assess the ability to re-find the prior detected orbit, the taken image and the corresponding viewing directions are evaluated. The data is employed in two different ways.
With real observations, it would take a certain time span to create and then analyze this image. There are several techniques available to analyze satellite images of staring telescopes. A possible approach in sidereal staring mode would be to first mask all already known objects, like stars, and then overlay the images to get a trace of the object. But this topic shall not be of concern at this point (for example, refer to [32]). In here, the analysis part is basically implemented as a user given time, in which the object is further propagated, and the telescope keeps staring. This time as to account for both the image processing and the moving of the telescope itself. Aim is now to re-find the object after the assumed image processing time. For this, two approaches has been analyzed, one using initial orbit determination methods, the other one using extrapolation of the data from the matrix.

Refinding the object using initial orbit determination

From the CCD image, several observations giving azimuth and elevation to the object have been determined. The approach now is to use these observation with the prior described angles only orbit determination method (refer to section 2.1.2). This method requires as inputs three observationsof azimuth and elevation, the associated times and some other inputs like the site's location. As observations, the first, middle one and last have been chosen to be used, to have a maximum angular spacing between them.
This method has been tested with several different sets of orbits and telescopes (regarding field of view and CCD chip and pixel size), but it has been found out that it is not suitable for this application, as the angular spacing even for enormous telescopes stay too small. Problem in here is that either the equation for the initial distance guess (see equation 2.33) cannot be solved, or the slant ranges to the object do not converge. Thus, one yields either no result at all, or an orbit that does not make any sense at all (for example below Earth radius, highly parabolic etc.). This was already expected, as this method is not meant to be used for such small spacing. Furthermore, discussions of angles only methods in the literature let assume that these techniques in general need much longer observation times ([33] and [32]). Although other initial determination methods like an algorithm proposed by Gooding in [34] might give reasonable

results faster (i.e. with smaller spacing) than the used Gauss' Angles Only method, due to the statements in the literature, no other methods of angles only orbit determination have been tested.

Refinding the object using extrapolation

The second approach is to re-find the object by extrapolating the observed elevation and azimuth values, thus expanding the tendency of their variation into the near future. As a first step, to proof the general work of this method, a simple linear extrapolation has been used. This one works just as a linear interpolation, but in here the value to be found is out of the range of the known values

$$h_{extra} = h_{k-1} + \frac{(t_{extra} - t_{k-1})}{(t_k - t_{k-1})} \cdot (h_k - h_{k-1}). \tag{4.23}$$

The subscript *extra* refers to the point of interest. The subscripts k and $k-1$ refer to the two last known elevations. The same equation is of course valid for azimuth calculations.
This approach has been tested for different kinds of orbits, furthermore for each orbit one sighting reaching a high elevation (above 75°) and one reaching a low elevation (below 35°, for TerraSarX 48°) have been taken. Mostly satellites on circular sun synchronous orbits at different heights where chosen, as here lies the focus of interest for the first observations. To recheck, one satellite with a lower inclination, and one with a higher eccentricity have been chosen (refer to table 4.1). The station in Stuttgart was again used as observatory.

As telescope two different set ups with two different cameras were used which are

Table 4.1: Orbits from TLE objects used for analysis of possible re-acquisition.

Satellite	Perigee [km]	Apogee [km]	Inclination [DEG]	Period [min]	SMA [km]
TerraSAR X	514.5	516.7	97.4	94.8	6886.6
Gensis II	515.6	594.1	64.5	95.6	6925.8
CartoSat 2B	628.7	652.5	97.7	97.4	7011.6
CryoSat 2	718.4	733.0	92.0	99.2	7096.7
Metop A	825.9	829.0	98.7	101.3	7198.4
Azur	369.0	1498.6	102.7	103.6	7304.8

very similar to those from chapter 3. The simulated hardware values of these are given in table 4.2.

Table 4.2: Hardware set ups used for re-acquisition analysis. The used telescope and cameras correspond to those used in chapter 3 for the Stuttgart station.

case	field of view [°]	focal length [m]	pixels [-]	pixel size [μm]
FLI camera	1.089	1939.68	4096	9
Andor camera	0.2421	1939.68	512	16

Furthermore, some conditions for the sightings have been set, These are:

- the detection elevation is at 20°,
- the object has to be rising (to allow sufficient long observation times),
- the time for detection is neglected.

Figure 4.4 shows the linear prediction of the line of sight and the associated field of view for the two simulated cameras for the Azur high elevation pass. The difference in the line of sight progress is due to the different values used for the extrapolation (small chip vs. large chip). In general, the predictions are good, especially for case #1: The true object position stays inside the field of view for elevation spanning over 10°. For the small chip in case #2 this looks different: The prediction is close, even closer than in the first case, to the actual line of sight, but due to the very narrow field of view the object leaves it again already after less than 5° in elevation. Coming back into sight another 5° later is a coincident. But as later shown, the further away from the observation the worse the time prediction gets.

Now it is shown that in general a prediction for the line of sight for the next some degrees is possible. But as mentioned before, just because the extrapolated line of sight is close to the true one, does not mean it is good enough for a re-find of an object. For this, also the time has to fit to the prediction. Analysis of this is shown in figure 4.5, again for the Azur high elevation pass, together with the one-dimensional field of view for the investigated case. In here, it can be seen that the elevation prediction is valid for one minute for the FLI camera and about 40 seconds for the Andor camera. For this sighting the values are acceptable, as this means that one has nearly 40 or 60 seconds (depending on the optical system) for the re-finding process respectively. But especially during passes with fast changes in azimuth and elevation, the linear prediction can give results that are valid too short. For example, during the TerrarSarX low elevation pass, one yields a prediction valid for ten seconds (compare figure E.1 in the appendix). These fast changes usually appear when the satellite is close to its turning point.

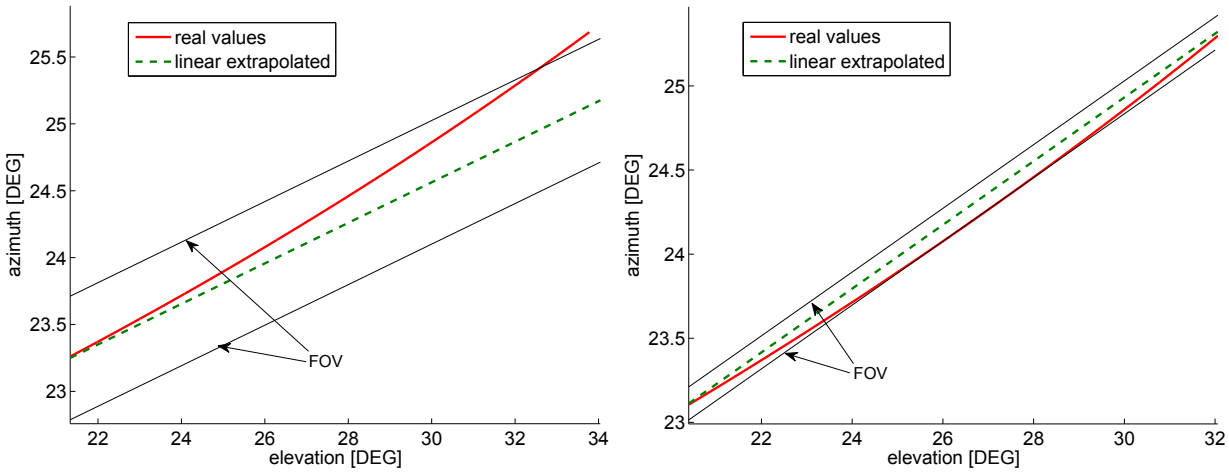

(a) FLI camera (b) Andor camera

Figure 4.4: Line of site prediction for Azur hight elevation pass. It can be seen, due to the different chip sizes, different values are used for the extrapolation and thus the progresses of this are different.

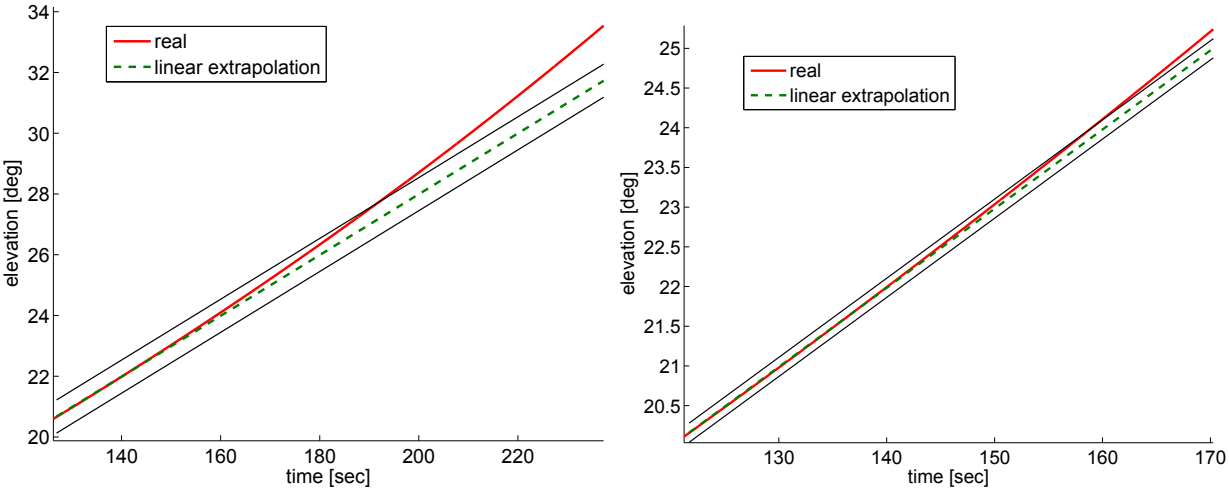

(a) FLI camera (b) Andor camera

Figure 4.5: Elevation over time for Azur high elevation pass. It can be seen that due to the larger field of view the prediction for the FLI chip is valid longer.

To get a more flexible prediction, in the following a quadratic least square method was used to fit the data. The aim of this method is basically to fit a function of the form

$$f(t) = c_1 + c_2 \cdot t + c_3 \cdot t^2 \tag{4.24}$$

to the detected data. In most cases, this method yields better results than the linear way. As example, the square fitted curves for the CryoSat-2 low elevation pass are shown in figure 4.6. In here, the square prediction is valid for 67 seconds (linear: 24 seconds).

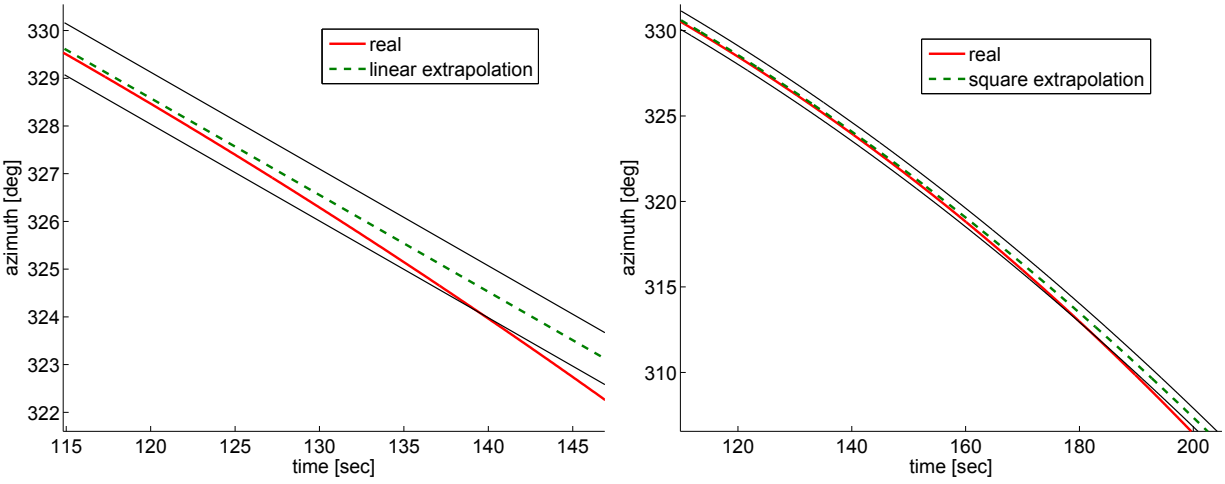

(a) linear (b) square

Figure 4.6: Azimuth over time for CryoSat-2 low elevation pass, with Andor camera. The square prediction is valid about 40 s longer than the linear prediction.

In the final code, both methods have been implemented so the user can choose which one to use, but referring to yielded results, it is recommended to choose the least square method. For the implementation of the latter one code from the linpack library [35] has been used.

The prediction can be run in two different analysis modes: First, one can enter a certain time, and the program checks, if the object is found giving this threshold (for example when total image processing and telescope moving time are known). Second, the program can determine how long one predictions of the extrapolated values can be used to re-find an object. The latter version was used for all further analyses.

4.2 Using POSADA with PROOF results

Now a tool to analyze the general possibility of passive optical detection and short-term re-acquisition of space debris objects exists. This tool shall be used to assess some of the in chapter 3 yielded results. In there, the numbers of visible objects for certain staring directions and observational system set ups were determined, without taking into the account of the usability of these objects. This is aim of the following analysis.
For analysis, the outputs of three different PROOF runs have been taken: Two ones during May while staring east (with the Andor camera with focal reducer) or west (with the FLI camera and focal reducer) respectively, and one during February, while staring north (with the FLI camera without focal reducer). The elevation during all the three runs was at 20°. Furthermore, all PROOF runs were performed for the Stuttgart Space Debris Observatory and give as results the visible objects over one night.

One problem for a further analysis of the PROOF results is the output created: Although orbital elements of each detected object are given, no valid time stamp for these elements is available. The only time stamp given states the time of the closest approach, which is not said to be at the actual sighting. Furthermore, in the output only the true anomaly of the object is updated, the other orbital elements stay as they were in the beginning of the whole simulation. So one cannot directly take the output and extend the analysis from there. Because of that, a workaround has been undertaken: From the given objects' orbits, new sightings have been determined. For this, the orbits given by PROOF have been taken and propagated till a sighting under the same line of sight as in PROOF was achieved. For propagation, only the geopotential till the 18th degree and order were considered, the line of sight had an error tolerance of $\pm 1°$ in elevation and $\pm 5°$ in azimuth. To perform this task, already written subroutines regarding propagation and line of sight determination already written for `analyzeMeasurements` and `POSADA` could be used.
This way of treating the objects of course brings some problems: First, the orbit is only close to that one used by PROOF. This is due to the unclear time validity and true anomaly. Second, reasoned by the first problem, and furthermore also due to different propagation techniques and accuracies, the sighting will not appear at the same time, very likely even not during the same observation period. This might lead to some uncertainties in the reflection of the results.
On the other hand, this approach gives realistic conditions of the sightings of the determined objects under the determined line of sight.

All three prior described PROOF runs were processed in this way, and assorted for

rising objects only. The observation staring west yielded 19 objects to be rising (of 36 detected ones in total), which orbits are shown in table 4.3. For staring north, 10 of 26 objects were rising, while staring east 13 of 37 rising objects could be detected. Of those 13 objects, tow reached its final elevation at just 20° and where thus not considered in the analysis. The orbital parameters for rising objects of those two simulations as well as all orbit parameters from not rising objects are shown in the appendix in tables E.2 to E.6. An explanation for the difference in rising objects will be given later in the discussion of the maximum yielded elevation.

Table 4.3: Rising objects from PROOF simulation staring west with an elevation of 20°. The simulation was performed for the Stuttgart site on 1st of May 2009 over one night with the FLI camera without focal reducer.

Object	sma [km]	ecc [-]	incl [°]	AoP [°]	RAAN [°]
#6	7152.80	86.39	0.0002	79.32	30.74
#10	7884.30	82.64	0.0025	39.80	30.79
#13	7578.70	99.61	0.0150	215.63	175.49
#15	7123.90	86.45	0.0002	78.03	359.24
#16	7367.90	82.94	0.0032	41.41	63.61
#17	7161.40	86.35	0.0026	340.07	61.84
#19	6992.80	64.56	0.0050	267.84	25.78
#21	8283.00	79.16	0.1691	206.86	66.37
#22	7291.00	70.08	0.0023	319.57	81.71
#23	7327.90	82.53	0.0014	276.25	173.93
#24	10013.80	46.60	0.3379	187.43	81.56
#25	7465.50	63.40	0.0362	256.53	143.76
#26	7486.50	63.40	0.0038	51.03	83.60
#28	7866.60	50.01	0.0011	253.71	114.68
#30	7236.60	81.21	0.0021	193.19	172.84
#32	7875.90	73.61	0.0026	101.98	71.07
#33	8998.90	81.36	0.1147	24.66	40.40
#34	7325.70	82.53	0.0014	260.73	171.39
#36	6862.50	73.85	0.0299	308.19	80.57

All these rising objects were analyzed using POSADA. Although, the objects were determined to be visible given a certain camera (depending on the run FLI or Andor), the

calculations of predictions and possible re-detection were performed for both camera set-ups, to further describe the differences using those cameras. The camera inputs, as realized in POSADA were already stated in table 4.2.
Below, the results for the predictions of the simulation while staring west are given in table 4.4. As before, shown are the times for which a prediction made on the basis of observed angles by the appertaining camera is valid. Additionally, the maximum elevation reached by that object as well as the time it is theoretically visible from the observer's ground station. (In here, it is assumed to be visible as long as the object has an elevation of 20°. Again, results for staring east and north are given in the appendix in tables E.7 and E.8.

Table 4.4: Validity of predictions for rising objects from table 4.3. Shown are the times for which the state vector of the propagated object stays in the predicted field of view and the maximum elevation reached.

Object #	FLI [s]	Andor [s]	maximum elevation [°]	time visible [s]
#6	75.4	34.1	20.98	114
#10	146	44.4	25.78	441
#13	122.7	47.1	20.4	106
#15 [1]	74	28.1	20.0	0
#16	100.4	26.2	23.5	247
#17 [2]	79.8	18.6	23.06	187
#19	65.2	17.4	33.64	303
#21	320.9	111.2	31.01	1096
#22	96.5	26.6	29.2	355
#23	97.2	29.9	22.3	203
#24	532.5	350.7	82.42	1915
#25	122.6	50.8	21.7	211
#26	100.7	30.1	39.78	520
#28	151.2	44.1	27.06	476
#30 [3]	86.6	29.6	25.39	257
#32 [4]	137.9	39	33.5	602
#33	160.1	39	28.85	592
#34	101.6	29.5	22.98	229
#36	60.7	25.3	25.7	198
average	138.5	53.8	29.33	257[5]

[1] peak elevation reached at 20°
[2] staring elevation set to 21°
[3] staring elevation set to 21.2°
[4] staring elevation set to 20.2°
[5] median

Now the first look is taken on the prediction times. In general one can say that all rising

objects deliver prediction times that are valid for a time span that should be sufficient for a recognizing of the object and a following rotation of the optical system: Minimum value, yielded for the Andor camera with object #19 is 17.4 seconds, in general the predictions last even much longer. The prediction times for the two other runs give similar results, although average values for staring east appear to be the worst.
As the predictions appear to be sufficient for a re-detection, the two other outputs get more into focus: The maximum yielded elevation and the time, the object is visible from the observer's location. Note that visible only refers to the theoretical visibility: There are no illumination aspects considered.
When first looking at the maximum elevations, a clear difference between staring north and staring west or east can be observed: While the two latter ones reach average elevations of below 30°, staring north yields an average of about 46°. This is explained by the connection between the inclination of the orbit and the viewing direction, which is furthermore also the explanation for the difference in numbers of rising objects.
Going step-by-step, one can divide all orbits into two parts regarding their travel direction relative to Earth: Direct orbits, on which the object travels in the spin direction of Earth, and retrograde orbits, on which the object travels against the spin. Direct orbits have inclinations below 90°, retrograde orbits above 90°. From this one could deduct that when staring west, in general staring west, direct objects appear to be rising and retrograde objects to be deceasing. Actually, the border is not as strict as the objects travel at certain heights so that orbits in the range around 90° degree can be see rising from both staring directions. Now taking into account that most orbits have inclinations below 90° (as seen already in figure 1.1, this could be taken as explanation for most object seen rising to the west, medium ones to the north and least when staring east.
The maximum elevation reached is reasoned by a similar reason: A highly inclined orbit entering the field of view at elevations at 90° (east) or 270° would never reach a high elevation, as it only travels along the edge of the observer's location. Best results regarding the elevation would be achieved when looking directly against the orbit, for example an object with an inclination of 80° would reach zenith when rising at an azimuth of 350°. Also this explanation is idealized in some ways, as it for example neglects the rotation of Earth while the object is visible, but it is sufficient to explain the large difference in yielded maximum elevations.
The last value, the time an object is between elevations of 20° is more complex, as here also the shape of the orbit and its actual height above ground would have to be considered. But as seen on the results, in general the higher the elevation, the longer the object is visible. Note that the average value for the visible times in the tables is given with the median, instead of the geometrical average as with the other values. This has

been done to filter the huge variances in the yielded times.
To further classify the described results, especially in regard to later laser illumination, please refer to the section 4.4.

4.3 Attenuation of the results

As already mentioned at some points, the yielded results where yielded for mostly perfect conditions. During real observations, these are in general not given. There are several reasons that will lead to worse conditions during real observations. These include:

- Atmospheric turbulence,
- Weather conditions,
- Realistic irradiation of the object,
- Misguiding of the telescope.

While the two latter ones lie behind the scope of this work, but at least a rough assessment of the two first ones shall be made to allow a classification of the yielded results.

4.3.1 Atmospherical turbulence

At this point the influence of atmospheric turbulence shall be assessed. The effect of this, also referred to as seeing, lead to a misplacing of the spots on the pixel. To account for these, a quite simple model was implemented. This model assumes that the local seeing is given by a Gaussian distribution around a given mean value and a standard deviation. The applied values are determined randomly with subroutines from [36]. As the seeing angle is given as a magnitude, it is now split up and applied on both measured angles.
Referring to [22], typical nights at average sites have average seeing conditions around 2″. To also account for other aberrations, like vibrations of the telescope, this analysis has been performed for a mean seeing of 5″ and a standard deviation around this value of 1″. The effect of applying this model on the simulated measurements is shown in figure 4.7.

It can be seen that seeing has a clear influence on the measured values: Without seeing the measured values run exactly like the true ones. With seeing, they jump around those. But as for extrapolation of azimuth and elevation a fitting function is applied, these jumps are smoothen again, so that still a valid prediction can be made.
To see the influence of seeing on the predictions, this model has been applied on several objects from table 4.3. The results for this are shown in table 4.5. As one can see there is a clear influence of seeing on the validity of the predictions, as it changes in

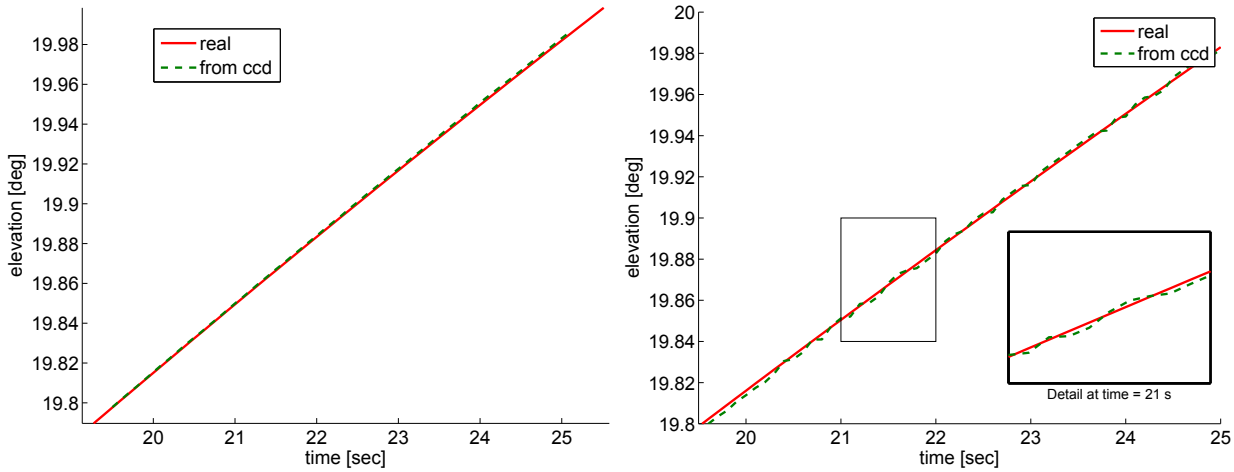

(a) without seeing (b) with seeing

Figure 4.7: Influence of seeing on measured elevation. Shown is object #6 from table 4.3, measured with FLI camera.

all cases, in some more than others. But still, for all runs predictions with at least 61 seconds validity could be made, the average validity even stays nearly the same.

4.3.2 Weather conditions for Stuttgart

So far, all observations assumed a perfect weather in Stuttgart. But of course, this is usually not the case and passive optical observations can only be performed during clear nights. To estimate the number of possible observation times, data from [37] has been used. From there, the relative cloud cover of the sky in eighth has been used. Due to the missing of night data, values for 6:00 and 18:00 for each day have been averaged. The average cloud cover over one year (2009) of the meteorological station in Stuttgart/Echterdingen is shown in figure 4.8. This yields the result of an average cloud cover over the year of about 70%, leaving 30% of nights with good conditions. Thus, for more realistic results, all values would have to be taken by 0.3. Although this assumption is not very accurate (first, clouds are not the only constraint, second, having clouds does not mean that there are no observations possible at all), it shows that Stuttgart is not a suitable place for a constantly working space debris observation station. But as shown in section 3.3, the longitude has no impact on the detectable object, thus for a final station one would have to choose a sight with good weather and sighting conditions.

Table 4.5: Validity of predictions for rising objects from table 4.3, applying atmospherical turbulence. Shown are the times for which the state vector of the propagated object stays in the predicted field of view. As camera, the FLI camera was used

Object #	without turbulence [s]	with turbulence [s]
#6	75.4	64.2
#10	146	103.4
#15 [1]	74	73.3
#19	65.2	61.2
#21	320	257.1
#22	96.5	122.7
#23	97.2	99.7
#25	122.6	114.1
#28	151.2	237.8
#34	101.6	106.9
#36	60.7	72.6
average	119.2	119.4

[1] peak elevation reached at 20°

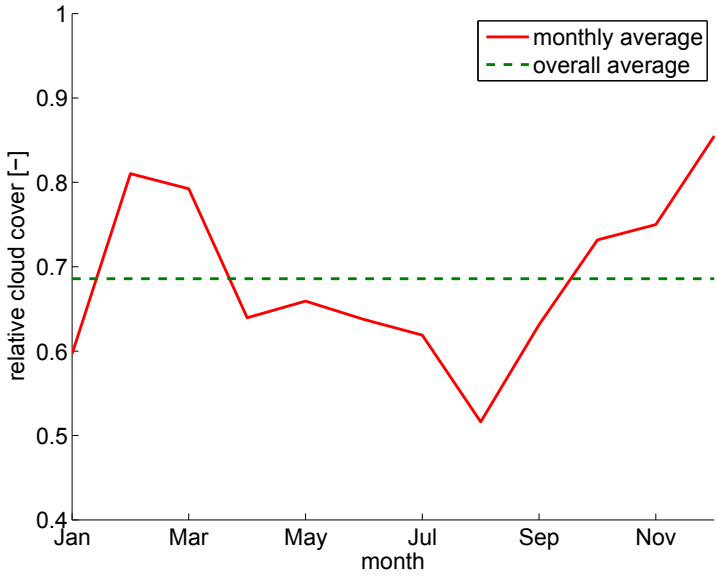

Figure 4.8: Relative cloud cover over Stuttgart, 2009.

4.4 Discussion of the results

In this chapter, first a written tool has been described to simulate a sighting of an object and further analyze it regarding the possibility of re-detection (section 4.1). Following, this tool has been used to analyze some results from PROOF observations from chapter 3 regarding the further use of the detected objects (section 4.2). For this, the first constraint was that elevations of the object have to be rising to allow a further tracking of those. Depending on the simulation, objects between 30% and 50% were found to be rising. All rising objects from three different PROOF simulations (one each for staring east, west and north) have been used as inputs for POSADA. In there it was shown that in general for all those objects, angular predicitions for at leat 17 seconds could be calculated, in average between 34 and 134 seconds, depending on the simulation run and camera. Furthermore, another effect was observed: Not only the total number of visible objects changes with the viewing direction, but also their possibility of further use for orbit determination. In here, large angular spacings (thus high maximum elevations) and long visible times are advantageous. [38] for example even gives time spans of ten minutes between the measurements for geocentric orbits when using angles only orbit determination.

Regarding these findings, the optimal staring directions for detecting most objects as summarized in section 3.4 need to be changed. Although when only considering the total number of detectable objects changes over the seasons, it appears that in general observations towards northern directions seem to be most suitable: In this direction, in average higher maximum elevations and longer observations times for most objects could be achieved. These could be further improved for single objects, if concentrating on certain staring directions depending on orbit inclinations during observations campaigns.

Applying the results regarding the further use of objects certainly mitigates the number of detected objects as described in chapter 3. This shall be visualized on the example of the long term simulation from Stuttgart at the 1^{st} of February 2009, staring at an elevation of 20° towards north (azimuth = 0°) using the FLI camera without focal reducer. During this run, PROOF stated 26 objects to be visible. From these 26, 10 were found to be rising. Although these ten objects seem to be re-findable and thus further trackable, probably not all of them will be useful for a final laser illumination. In here, the constraints will depend on the finally chosen technical implementation of the laser ranging. But experiments in Graz so far showed that objects should be rising above 30° and stay above as long as possible to tune the laser. Additionally, as approached

in section 4.3.2, weather and atmospheric conditions will attenuate the number of usable objects further, for weather conditions as in Stuttgart by roughly 70%, leaving a total number of 3 objects per night with the given optical system. Now also taking into account that ongoing visibility of the object was not considered during the further use reflection, this number actually might decrease further. Thus only a small fraction of all detected objects will finally qualify to be used for laser illumination.

Chapter 5

Summary

Comparing the space debris observation methods In the first part (chapter 2), three different space debris observation techniques were analyzed regarding their accuracies for initial orbit determinations. The techniques compared were radar, passive optical and combined laser ranging and tracking.
For this, the deviations in measurements with these techniques have been assessed. In here, radar measurements, errors in radar measurements were set to $\pm$ 57 m in range and angular $\pm$ 400 μrad for a 10 cm sphere, and $\pm$ 45 m in range and $\pm$ 231 μrad in angular measurements for a 1 m sphere. Combined laser ranging and tracking were found out to yield accuracies of $\pm$ 3 m in range and 30 μrad in angular accuracy. As passive optical observations yield angular measurements only, for these the accuracies were assumed to be 27 μrad.
Following, these techniques were analyzed using the in the scope of this work written FORTRAN tool `analyzeMeasurements`. In this tool, the influence of the errors in measurements on initial orbit determination on the first measurement as well as on the orbit propagated over one day. As initial orbit determinations methods, depending on the measurements either a combined Gibbs/Herrick-Gibbs method (for a set of three angular and range measurements) or Gauss' angles-only method (for a set of three angular measurements) were used. For propagation, a numerical propagator considering the geopotential (EGM-96) and atmospheric perturbations has been implemented.
In this tool, first a reference orbit (the orbit, determined with the according determination method and no errors in measurements) has been calculated and propagated over one day. Afterwards, orbits considering the prior determined errors have been determined and also propagated over one day. Afterwards, these orbits were compared.
As results, it was found out that, especially for predictions after one day, orbits determined with combined laser ranging and tracking yield best results, in comparison to radar due to the lowest errors in the measurements, in comparison with passive-optical measurements due to the advantage of a three dimensional measurement. In a

discussion, the yielded results have been set into context.

Simulations with PROOF2009 During the second part (chapter 3) the visibility of space debris objects referring to PROOF2009 was assessed. The performed simulations were split into two parts: First into simulations for the DLR Space Debris Observatory in Stuttgart, second more general ones regarding scaling of hardware and the location of the optical system.
For the first part in the beginning the hardware of the DLR Observatory was presented. Following, different sets of simulations have been performed to determine the performance of the DLR Space Debris Observatory in Stuttgart. These assessed the size of minimum detectable objects, the dependency of the numbers of detected objects over viewing directions and the influence of the seasons for observations.
Furthermore, more general simulations have been performed. These addressed the scaling of the used hardware as well as the dispersion of stations at different locations on Earth.
For the DLR Space Debris Observatory, it was found out that with the given hardware, objects down to sizes in the centimeter range could be found. For detecting most objects, staring at low elevations appeared to yield best results during all seasons. Regarding the azimuth, during early summer simulations yielded best results when staring east, for late summer for staring west. For winter, north was found to be optimal. Staring south gave worst results in all cases. Regarding the total numbers it could be shown that these highly depend on the used setting. Using a high sensitive EMCCD camera with a small field of view for optimal staring direction, 20 objects could be detected during one night in summer, and about 43 during one night in winter. Using a camera with lower sensitivity but larger field of view yielded slightly higher results (24 during summer, 55 during winter). Furthermore, all numbers could be improved by a factor just below two when enlarging the field of view using a focal reducer.
In general, simulations showed that scaling the used optical system improves the number of detected objects. Two different scalings were analyzed, changing the field of view and changing the aperture. With both, more objects could be detected due to different reasons. Regarding the location of a possible station it was shown that in general, higher latitudes lead to more detectable objects, latitudes close to the equator deliver worst numbers. The longitude of the station seems to have no clear influence on the number of detectable objects.

Re-detection after initial detection In chapter 4, the further use of detected objects has been analyzed. For this, the tool `POSADA` was written. This tool simulates a sighting of an object, takes an idealized CCD image of the sighting and uses this image to

predict the future position of the object on the local sky. As prediction methods, initial orbit determination methods and extrapolation were tested. As angular spacing of the observations appeared to be too small for initial orbit determination methods, as final method extrapolating the observed angles with a quadratic least square method was used. During the implementation, the tool has been tested with a set of different TLE objects.

Following, three results from PROOF were analyzed regarding the further use of the detected objects. In here, two simulations performed in May, one staring east and one staring west, and one February simulation staring north were used. The first condition for objects to be re-findable was that the object has to be rising. From the PROOF results, depending on the simulation between 30% and 50% of the objects were found to be rising. Using the implemented method, for all rising objects predictions valid for at least 17 seconds regarding the future position could be made, the average validity lied between 34 and 138 seconds, depending on the used hardware and simulation. It further was shown that predictions made with camera with larger field of views in general lasted longer.

Furthermore, two other crucial factors for re-use of objects were considered, which are the maximum elevation during the sighting and the time the object is visible. The elevation is important as for laser illumination, the object has to rise above a certain height, the time is important, as longer observation times lead to in general more accurate determined orbits. Taking this into consideration, staring north gave best results. This could be explained by the distribution of space debris objects regarding their inclination.

As only perfect conditions have been considered to this point, following the influence of attenuations has been broached. First, the influence of atmospheric turbulence was included. Due to the statistic influence of turbulence and the predictions being calculated by data fitting methods, it could be shown that the results do change, but in average do not get worse: Still for all analyzed cases, lasting predictions could be calculated, in some cases worse, in some better than without turbulence. Last, it was shown that when considering weather conditions, average results regarding total numbers of used objects get reduced dramatically. In a final reflection for a certain PROOF simulation performed for Stuttgart the number of 26 detected objects was reduced to 3, when considering the found constraints for re-usability and local weather conditions.

Bibliography

[1] H. Klinkrad, *Space Debris - Models and Risk Analysis*. Berlin: Springer, 2006.

[2] S. Flegel, J. Gelhaus, M. Moeckel, and C. Wiedemann, *Maintenenance of the MASTER Model*. No. 21705/08/D/HK, Braunschweig: Institute of Aerospace Systems, TU Braunschweig, 2010.

[3] H. Klinkrad, *Raumfahrttechnik IV: Space Debris*. Braunschweig: Institute of Aerospace Systems, TU Braunschweig, 2008.

[4] U. Voelker, I. Buske, T. Hall, B. Huettner, and W. Riede, "Laser-based space debris monitoring," in *AIP Conference Proceedings*, (Melville, New York), American Institute of Physics, 2011.

[5] G. Kirchner, D. Kucharski, and F. Koidl, "Millimeter ranging to centimeter targets," 2008.

[6] G. Kirchner, F. Koidl, F. Friederich, I. Buske, U. Voelker, and W. Riede, "Laser measurements to space debris from graz slr station," 2012.

[7] J. Gelhaus, S. Flegel, and C. Wiedemann, *Program for Radar and Optical Observation Forecasting*. No. 21705/08/D/HK, Braunschweig: Institute of Aerospace Systems, TU Braunschweig, 2011.

[8] D. A. Vallado, *Fundamentals of Astrodynamics and Applications, Third Edition*. New York, NY: Space Technology Library, Springer, 2007.

[9] P. Escobal, *Methods of Orbit Determination*. New York: John Wiley & Sons, Inc., 1965.

[10] O. Montenbruck and Gill, *Satellite Orbits*. Berlin: Springer, 2001.

[11] H. Bucerius, "Bahnbestimmung als Randwertproblem," in *Astronomische Nachrichten 278*, pp. 193 – 216, 1950.

[12] A. E. Roy, *Orbital Motion, Fourth Edition*. Bristol and Philadelphia: Institute of Physics, 2005.

[13] R. W. Freund and R. H. Hoppe, *Stoer/Bulirsch: Numerische Mathematik, 10. Auflage*. Berlin: Springer, 2007.

[14] J. Bendisch, *Raumfahrttechnik II: Raumfahrtmissionen*. Braunschweig: Institute of Aerospace Systems, TU Braunschweig, 2008.

[15] L. Shampine and M. Gordon, *Computer-Lösung gewöhnlicher Differentialgleichungen*. Braunschweig/Wiesbaden: Vieweg, 1984.

[16] B. R. Bowman, W. K. Tobiska, F. A. Marcos, and C. Valladares, "The jb2006 empirical thermospheric density model," *Journal of Atmospheric and Solar-Terrestrial Physics*, vol. 70, pp. 774–793, 2008.

[17] *ECSS Standards: Space Engineering: Space Environment*. No. ECSS-E-ST-10-04C, Noordwijk: ECSS Secretariat ESA-ESTEC, Requirements & Standards Division, November 2008.

[18] "The SOFA Software Libraries, Internaional Astronomical Union,."

[19] G. Curry, *Radar System Performance Modeling*. Boston: Artech House Publishers, 2004.

[20] J. Markkanen and M. Postilla, "Real-time small-size space debris detection with eiscat radar facilities." http://www.eiscat.se/spade/FiPresentation_SDII.pdf. accessed 28.06.2012.

[21] J. Markkanen, M. Lehtinen, and M. Landgraf, "Real-time space debris monitoring with eiscat." http://www.eiscat.se/spade/paper_JASR7345.pdf. Elsevier Science, 9 March 2005.

[22] C. Kitchin, *Telescopes and Techniques, Second Edition*. London: Springer, 2007.

[23] Astelco, "New Technology Mount (NTM)." http://www.astelco.com/html/products/ntm/ntm.htm. accessed 24.07.2012.

[24] J. N. Opiela, "A study of the material density distribution of space debris," *Advances in Space Research*, vol. 43, pp. 1058–1064, 2009.

[25] M. Weigel and A. Patyuchenko, "Orbit Determination Error Analysis for a future Space Debris Tracking Radar," in *European Space Surveillance Conference*, 2011.

[26] J. Gelhaus and S. Flegel, *Software User Manual: PROOF 2009*. No. 21705/08/D/HK, Braunschweig: Institute of Aerospace Systems, TU Braunschweig, 2011.

[27] Planewave, "17 inch dck optical tube assembly." http://www.planewave.com/index.php?page=1&id0=0&id=1. accessed August 2012.

[28] Finger Lakes Institutes, "Pro line pl 16803 data sheet," 2012.

[29] P. Jorden, "Sensor developments at e2v," 2008.

[30] Andor Technology, "ixon ultra 897 data sheet," 2012.

[31] T. Wallace, "SLALIB – Positional Astronomy Library." http://www.starlink.rl.ac.uk/docs/sun67.htx/sun67.html, 2005. accessed 17.10.2012.

[32] J. Choi, J. H. Jo, Y.-J. Choi, G.-I. Cho, J.-H. Kim, Y.-H. Bae, H.-S. Yim, H.-K. Moon, and J.-H. Park, "A study on the strategies of the positioning of a satellite on observed images by the astronomical telescope and the observation and initial orbit determination of unidentified space objects," *Journal of Astronomy and Space Sciences*, 2011.

[33] F. M. Fadrique, A. A. Mate, J. J. Grau, J. F. Sanchez, and L. A. Garcia, "Comparison of angles only initial orbit determination algorithms for space debris cataloguing," in *22nd International Symposium on Space Flight Dynamics*, (Issac Newton 11, 28760 Tres Cantos, Spain), 2011.

[34] R. Gooding, "A New Procedure for Orbit Determination Based on Three Lines of Sight (Angles Only)," 1993.

[35] J. Dongarra, "Linpack - Linear Algebra PACKage." http://www.netlib.org/linpack. accessed 17.10.2012.

[36] R. Chandler and P. Nortrop, "Documentation for file randgen.f." http://www.ucl.ac.ul/ ucakarc/work/software/rangen.txt. accessed 08.11.2012.

[37] Deutscher Wetterdienst, "Klimadaten für Stuttgart/Leinfelden 2009." www.dwd.de. accessed 02.11.2012.

[38] G. J. Der, "New angles-only algorithms for initial orbit determination," in *AMOS Conference*, pp. 412–427, 2012.

List of Figures

List of Tables

Appendix A

German summary

Die vorliegende Arbeit ist in drei Teile gegliedert. Daher soll sich diese Zusammenfassung an der Gliederung orientieren.

Vergleich von verschiedenen Space Debris Beobachtungsmethoden Im ersten Teil (Kapitel 2) wurden drei verschiedene Space Debris Beobachtungsmethoden hinsichtlich ihrer Genauigkeiten bei vorläufigen Orbitbestimmungen untersucht. Die verglichenen Methoden waren Radar, passiv optische Beobachtungen und kombiniertes Laser Ranging und Tracking. Dafür wurden zunächst die Abweichungen in Messungen mit diesen Techniken abgeschätzt. Dabei wurden für Radarmessungen Abweichungen von $\pm$ 57 m in Entfernung und $\pm$ 400 μrad in Winkelgenauigkeit für eine Kugel mit 10 cm Durchmesser, und $\pm$ 45m und $\pm$ 231 μ rad für eine Kugel mit 1 m Durchmesser bestimmt. Für die kombinierte Laser Ranging und Tracking Methode liegen diese Werte bei $\pm$ 3 m in der Entfernung und $\pm$ 30 μrad in den Winkeln. Da passiv optische Beobachtungen nur Winkel messen, ist hier nur dessen Genauigkeit zu berücksichtigen, die bei $\pm$ 27 μrad liegt.
Anschließend wurden diese verschiedenen Methoden mit Hilfe des in dieser Arbeit geschriebenen FORTRAN Tools `analyzeMeasurements` untersucht. In diesem Tool wird der Einfluss der Messfehler auf die vorläufige Orbitbestimmung sowohl direkt nach der Messung als nach einem Tag untersucht. Als Orbitbestimmungsmethoden wurde je nach Messmethode entweder eine kombinierte Gibbs/Herrick-Gibbs (für drei Winkel und Entfernungsmessungen) oder eine Gauss' angles-only Methode (für drei Winkelmessungen) verwendet. Für die Propagation wurde ein numerischer Propagator geschrieben, der als Störungen sowohl das Geopotential (EGM-96) als auch atmosphärische Störungen berücksichtigt, geschrieben.
In diesem Tool wird zunächst ein Referenzorbit bestimmt und anschließend über einen Tag propagiert. Referenzorbit bezeichnet den Orbit, der mit der jeweiligen Orbitbestimmungsmethode unter Annahme keiner Messfehler bestimmt wurde. Anschließend

werden Orbits unter Berücksichtigung der Messfehler bestimmt und ebenfalls über einen Tage propagiert. Als Ergebnis werden die absoluten Positionsfehler sowohl vor als auch nach der Propagation betrachtet.
Es wurde dabei herausgefunden, dass, besonders für die propagierten Orbits, die mit Laser Ranging und Tracking bestimmten Objekte die besten Ergebnisse erzielen. Dieses liegt an den im Vergleich zum Radar geringer angenommenen Messfehlern, im Vergleich zu der passive optischen Methode an dem Vorteil der dreidimensionalen Messung. In einer angeschlossenen Diskussion wurden dieser Ergebnisse weiter eingeordnet.

Simulationen mit PROOF2009 Im zweiten Teil (Kapitel 3) wurde die generelle Sichtbarkeit von Space Debris Objekten nach PROOF2009 untersucht. Die durchgeführten Simulation waren in zwei Teile unterteilt: Zunächst wurden die Machbarkeiten für das DLR Space Debris Observatory in Stuttgart betrachtet, als zweites wurden ein mehr generelles Scaling von Hardware und der Einfluss der Position einer möglichen Station auf die Sichtbarkeiten analysiert.
Im ersten Teil wurde zunächst die Hardware des DLR Obervatory beschrieben. Anschließend wurden Simulationen für diese Hardware durchgeführt. Bei diesen wurde die Größe der kleinsten sichtbaren Objekte, die Abhängigkeit der Anzahl an sichtbaren Objekten je nach Blickrichtung und der Einfluss der Jahreszeiten auf die Ergebnisse untersucht.
Für das DLR Space Debris Observatory wurde herausgefunden, dass es mit der vorhandenen Hardware möglich ist, Objekte bis zu minimalen Größen von wenigen Zentimetern zu finden. Die meisten Objekte wurden jeweils bei niedrigen Elevationen gefunden, unabhängig von der Jahreszeit. Bezüglich der Blickrichtung in Azimut, als beste Blickrichtungen wurde im frühen Sommer der Osten, im späten Sommer der Westen identifiziert. In Wintersimulationen wurden die meisten Objekte bei Blickrichtungen nach Norden gefunden. Beobachtungen in Richtung Süden ergaben in allen Fällen die schlechtesten Ergebnisse. Die Anzahl der dabei entdeckten Objekte hängt zum stark von den verwendeten Hardware Settings ab. Bei der Verwendung einer hochempfindlichen EMCCD Kamera mit einem kleinen Gesichtsfeld wurden in einer Sommernacht bei optimaler Blickrichtung 20 Objekte, in einer Winternacht 43 Objekte Entdeckt. Mit einer wenig empfindlichen Kamera mit dafür größerem Gesichtsfeld wurden leicht mehr Objekte entdeckt (im Sommer 24, im Winter 55). Weiterhin konnte die Gesamtanzahl durch Verwendung eines Focal Reducers, durch den das Gesichtsfeld vergrößert wird, um einen Faktor von etwas unter zwei verbessert werden.
Weiterhin wurde gezeigt, dass eine Skalierung des optischen Systems die Anzahl der entdeckten Objekte verbessern kann. Zwei verschiedene Skalierungen wurden betrachtet, zum einen ein durch eine Vergrößerung des Gesichtsfeldes, zum anderen durch

eine Vergrößerung der Teleskopöffnung. Mit beiden Methoden lassen sich auf Grund von verschiedenen Gründen mehr Objekte entdecken. Bezüglich der Lage der Station zeigen die Simulationen, dass der Längengrad keinen erkennbaren Einfluss auf die Anzahl der entdeckten Objekte hat. Bei den Breitengraden hingegen zeigt sich, dass bei höheren Breitengraden mehr Objekte entdeckt werden können, am wenigsten am Äquator.

Wiederfinden der Objekte nach der Erstentdeckung In Kapitel 4 wurde die Weiterverwendbarkeit der entdeckten Objekte analysiert. Dafür wurde das Toll POSADA geschrieben. Dieses Tool simuliert die Sichtung eines Objektes, erzeugt ein idealisiertes CCD Bild dieser Sichtung und verwendet es anschließend für die Vorhersage der zukünftigen Position des Objektes am Himmel. Für Bestimmung der Vorhersage wurden sowohl vorläufige Orbitbestimmungsmethoden als auch Extrapolationen getestet. Da die Winkel zwischen den aufgenommenen Beobachtungen jedoch bei Weitem zu gering waren, wurde für die weitere Analyse eine Extrapolation der Beobachteten Winkel mit Hilfe eines quadratischen Least-Square Fits durchgeführt. Während der Umsetzung des Tools wurden die einzelnen Methoden mit verschiedenen TLE Objekten getestet.
Anschließend wurden die Ergebnisse von drei PROOF Simulationen hinsichtlich ihrer weiteren Verwendbarkeit betrachtet. Dabei wurden zwei Mai-Simulationen mit Blickrichtungen nach Westen und Osten, und eine Februarsimulation mit Blickrichtung nach Norden verwendet. Die erste Bedingung um Objekte weiter betrachten zu können war, dass diese aufsteigend sein müssen. Nach den PROOF Ergebnissen gingen je nach Simulation zwischen 30 % und 50% der Objekte auf. Mit der implementierten Methode für die Vorhersage der Objektposition konnten für alle Objekte gültige Positionen von mindesten 17 Sekunden getroffen werden, im Durchschnitt je nach Simulation und verwendeter Hardware für zwischen 34 und 138 Sekunden. Dabei zeigte sich, dass auch hier ein größeres Gesichtsfeld von Vorteil ist.
Weiterhin wurden zwei andere wichtige Faktoren für die Wiederentdeckbarkeit betrachtet. Dieses sind die maximale Elevation und die Gesamtzeit, die das Objekt vom Beobachtungsstandort sichtbar ist. Dabei ist die Elevation wichtig für eine Erfolgreiche Bestrahlung mit dem Laser, da das Objekt eine gewisse Höhe über erreichen muss. Die Beobachtungszeit ist von Bedeutung, da längere Beobachtungen in der Regel genauere Orbitbestimmungen zulassen. Unter Berücksichtigung dieser Faktoren ergab sich, dass die meisten weiter verwendbaren Objekte bei Blickrichtungen nach Norden zu entdecken sind. Erklärung dafür ist die Verteilung Anzahl der Space Debris Objekte über der Inklination.

Da bisher für die Wiederentdeckung optimale Bedingungen angenommen waren, wurde zusätzlich der Einfluss von weiteren Störungen betrachtet. Zunächst wurde der Einfluss atmosphärischer Turbulenz untersucht. Durch den statistischen Einfluss von Turbulenz und die Vorhersage auf Grundlage von Data Fitting konnte gezeigt werden, dass sich die Gültigkeit der Vorhersagen zwar verändern, aber im Durchschnitt nicht schlechter wird: Es konnten weiterhin für alle betrachteten Objekte gültige Vorhersagen getroffen werden. Diese waren in manchen Fällen bessern, in manchen schlechter als ohne Turbulenz. Als letztes wurde gezeigt, dass bei Berücksichtigung der Wetterbedingungen die durchschnittlich erzielten Ergebnisse dramatisch verschlechtert werden. In einer finalen Betrachtung einer bestimmten PROOF Simulation für Stuttgart wurde gezeigt, dass die durchschnittliche Anzahl der entdeckten Objekte von zunächst 26, unter Berücksichtigung der Wiederverwendbarkeit und der lokalen Wetterbedingungen, nur noch 3 Objekte übrig bleiben.

Appendix B

Coordinate systems

Throughout the whole process of orbit determination and propagation, many different coordinate systems are used. Especially when reading the source code, it might be useful to have a certain overview of the systems used. For a more detailed and more complete overview of coordinate systems used in orbit dynamics, refer to the sources [8] and [9], which both give remarkable overviews over coordinate systems and transformations between them. The descriptions given here also base on those sources. To maintain a certain structure, the systems have been divided in typical systems used for observations, and 'other' systems, which are used both to express the observations as well to perform the orbit determinations, propagations and orbit descriptions.

B.1 Earth centered systems

First, an overview of the Earth centered systems is given.

B.1.1 Earth Center Intertial (ECI) Systems

The **E**arth **C**entered **I**nertial (**ECI**) coordinate system describes a coordinate system that's center is aligned with the Earth, but not rotating with it. Other common designations for this coordinate system in the literature is Geocentric Equatorial System, IJK-System or Conventional Inertial System (CIS). In this this system the x-axis (or I-axis) is pointing towards the vernal equinox, the z-axis (K-axis) is pointing through the north pole. The y-axis (J-axis) fulfills the requirements for a right handed coordinate system. Furthermore, the x,y-plane (I,J-plane) lies in the equatorial plane.
Due to movements of the vernal equinox and the equatorial plane, this system is not a real inertial system, but when referring to the equator and equinox at particular epochs, one yields a 'pseudo' Newtonian inertial system. In this work used systems are the IAU-76/FK5 based on the Fundamental Katalog and the J2000, which is is realized in

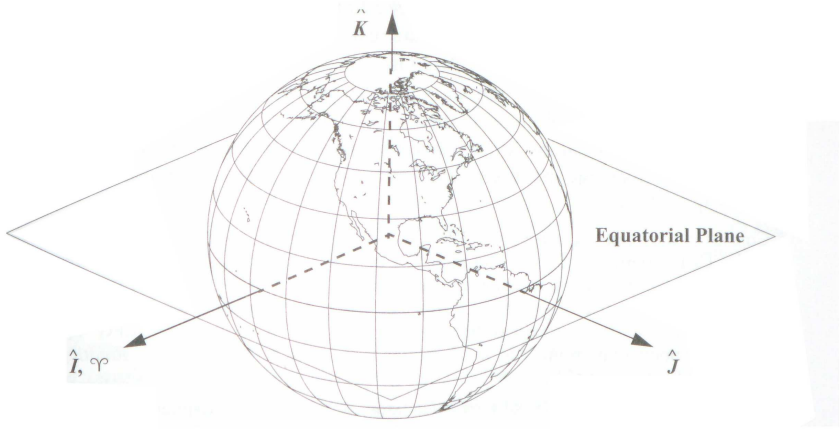

Figure B.1: ECI coordinate system [8]

the IAU-76/FK5 system but with 2000 as reference epoch. As methods for transformations, either the IAU-76/FK5 or IAU-2000A reductions where used. Another ECI system appearing in this work is the TEME system (true equator mean equinox). Because of the lack of clear definitions for this coordinate system, the state vectors given in this system always have been transformed to standard systems prior use. The standard inertial reference frame for Earth is the GCRF (geocentric celestial coordinate system), which is basically identical to J2000 and IAU-76/FK5 systems.
The polar description of the system is realized by right ascension and declination. The right ascension is here the angle from the vernal equinox, positive to the eat, in the equatorial plane ($-90...90°$), the declination the angle in the plane perpendicular to that, counted from the equatorial plane in both directions, positive to the north (thus from $-90...90°$). Depending on the purpose, the range ρ describes the total distance between the object and the center of Earth.

B.1.2 Earth Centered Earth Fixed (ECEF) Systems

The **E**arth **C**entered **E**arth **F**ixed (**ECEF**) coordinate system is fixed with the rotating Earth. It is also known as Body-Fixed(BF), or as a counterpart to the GCRF as International Terrestrial Reference Frame (ITRF). The center of this system is the center of Earth. The x-axis is pointing towards the zero-meridian, z to the north and y com-

pletes the right handed system. Also, the x,y-plane lies in the equatorial plane. It is frequently used to describe observations. In here, as geoid to convert between polar and Cartesian coordinates, the WGS-84 conventions are used, which are basically identically with ITRF coordinates.
The polar realization of this system is the well known used description in latitude and longitude. The distance is usually given in a height above the used ellipsoid. Further note that values change slightly depending on the geoid used. Furthermore, for high accuracy applications one has to differ between geocentric and geodetic values.

B.2 Observer/Topocentric systems

Now an overview of the observer centered systems is given. Note that topocentric always refers to an observer point of view. But depending on the purpose, this point of view might change: For Earth-bound satellite (as in this work), topocentric usually refers to the local position on Earth, while during stellar observations topocentric usually refers to the Earth itself.

B.2.1 Topocentric IJK-System

This system is the local realization of the ECI system. It means, that its center is translated from the Earth's center to the local position, while the pointing of the axes stays the same. Usually, this system is used when observation of Earth bound satellites are described as declination and right ascension. Although for stellar observation, topocentric and Earth centered values are identical, for low flying objects they vary dramatically.

B.2.2 Topocentric Horizon Coordinate System (SEZ)

This system is commonly used to describe observations. It is fixed to a certain given site. The S-axis of this system points due to the South of the location (also on the Southern Hemisphere), the E-axis to the East and the Z-axis towards the local zenith (thus the name SEZ system). The polar realization of this system is the in this work very often used description as azimuth and elevation. In here, azimuth is defined from North positive to the East from 0° to 360°, the elevation is define to be positive over the local horizon, between -90° and 90°. If further needed, the distance to an object

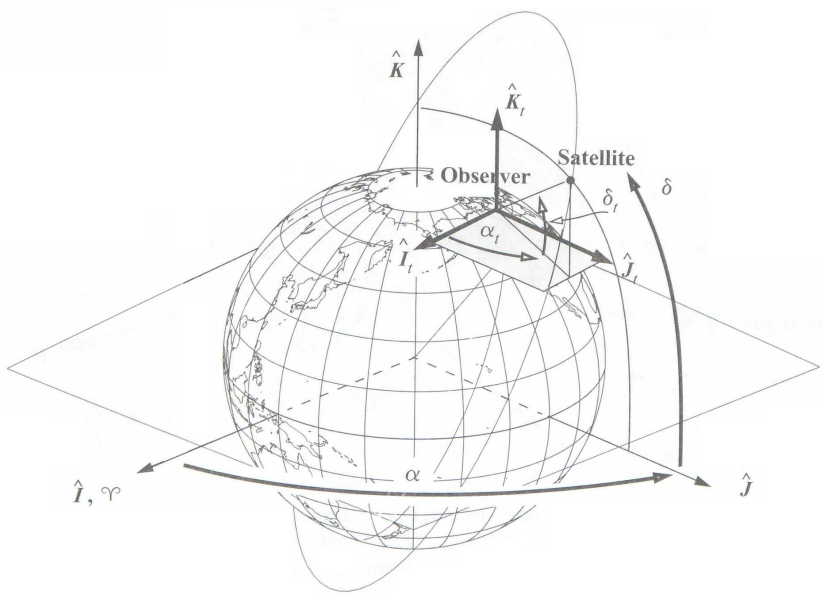

Figure B.2: Topocentric IJK coordinate system [8]

is given as range ρ.As one can directly measure local angles as seen, this system is especially useful for observations.

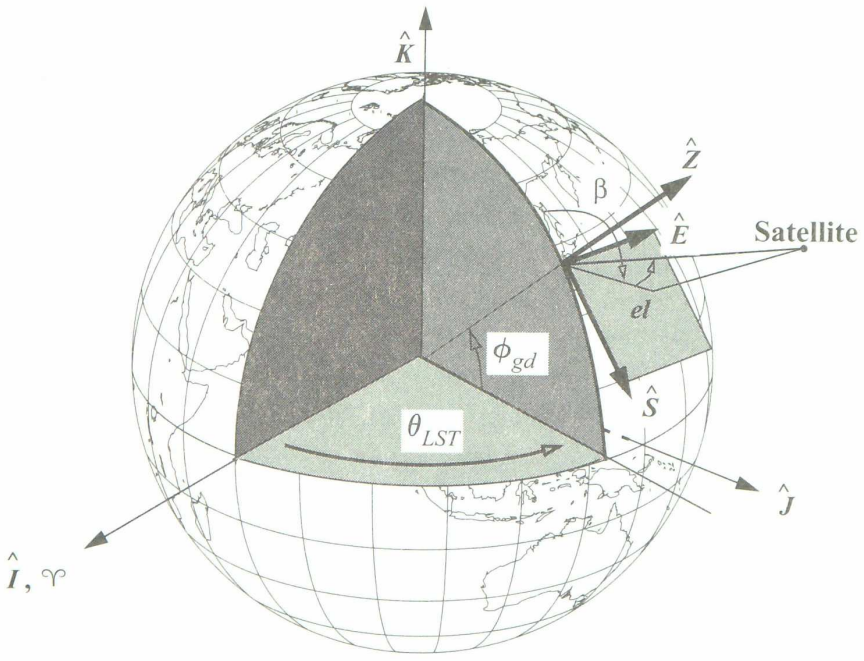

Figure B.3: SEZ coordinate system [8]

Appendix C

Documentation of tools

C.1 Radar Accuracy Determination

At this point, the Matlab tool to determine the radar accuracy is shown. As the description given in section 2.4.1 only the source codes will be given. Source for all functions is [19].

Matlab Script: `scriptRadar`

```
% the script to combine all the radar FUNCTIONS!
%
%% INPUTS: Define here the required inputs
clc
clear all
peakPower= 1500000; % the peak power of the radar, [W], from Eiscat
tau= 2e-6; % the pulse duration time [s]   ( from Eiscat, from slides!)
gainTrans= 64565; % the gain of the transmitter [-] NOT IN DB!!!, (from Eiscat)
areaReceiv= 3216.033998; % the area of the receiving antenna [m^2]  (from Eiscat,
% with Gain receiver=gain transmitter!!!)
range= 1500000; % the range to the object (assuming monostatic) [m]
systemTemp= 100; % the system noise temperature [K] ( from Eiscat)
losses= 75; % the overall system losses [-]
integration= 30; % from 300ms integration time given in EISCAT paper
minSize= 0.01; % the minimum size of particle to look at [m^2]
maxSize= 10; % the maximum size of particle to look at [m^2]
stepSize= 0.01; % the step size in size variation [m^2]
theta=0.5*pi/180; % the radar beamwidth in the angular coordinate of measurement  (from Eiscat)


%% call of functions
% constants
c=299792458; % speed of light in m/s
% getting the signal to noise, for single pulse and coherent integration.
% Note that this is more or less a quite rough calculation
[signalToNoise, signalToNoiseCoherent]=Signal2Noise(peakPower,tau,gainTrans,areaReceiv, ...
range,systemTemp,losses,integration,minSize,maxSize,stepSize);

% get the delta R value (assuming a CW-Waveform, with tau=tau_r)
deltaR=c*tau/2;
% now: getting the standard deviation for range measurement
[rangeError, rangeErrorCoherent]=RadarRangeError(deltaR,signalToNoise,signalToNoiseCoherent);

% and the same for the angle
[angleError, angleErrorCoherent]=RadarAnglesError(theta,signalToNoise,signalToNoiseCoherent);

%% preparing the outputs
figure
hold on
title('range error from radar measurement for Eiscat radar [m]')
plot([minSize:stepSize:maxSize],rangeError,'r','linewidth',2)
plot([minSize:stepSize:maxSize],rangeErrorCoherent,'g','linewidth',2)
legend ('normal signal to noise','coherent integration')
xlabel(['effective radar cross section of object [m^2]'])
ylabel(['sigma-1 value of error [m]'])

figure
hold on
title('angular error from radar measurement for Eiscat radar [rad]')
plot([minSize:stepSize:maxSize],angleError,'r','linewidth',2)
plot([minSize:stepSize:maxSize],angleErrorCoherent,'g','linewidth',2)
legend ('normal signal to noise','coherent integration')
xlabel(['effective radar cross section of object [m^2]'])
ylabel(['sigma-1 value of error [rad]'])
```

Matlab function: `Signal2Noise`

```
% function to get the signal to noise ratio for a radar over the signal's
% effective radar cross-section
%
% Source: Curry G.R., 'Radar System Performance Modeling', Artech House
% Publishers, Boston, 2001, pp. 65
%
% Required inputs: please check under inputs!
%
%
% Outputs:  - 'Normal' The signal to noise ratio, so far as FACTOR, not [dB]
%           - 'coherent integrated': The coherent integrated signal to
%           noise ration [NOT dB!!!]
%
% Author and Date: Jonas Radtke, 06.06.2012
%
% Tested: Has been tested manually! Results are conform with results from
% 2001 edition of the book
%
%--------------------------------------------------------------------------
%% Inputs
function [signalToNoise, signalToNoiseCoherent]=Signal2Noise(peakPower,tau,gainTrans, ...
areaReceiv,range,systemTemp,losses,integration,minSize,maxSize,stepSize)
%% calculations
% constants
clc
k=1.3806488e-23; % Mr. Boltzman's constant [J/K]
sigma =minSize; % target radar cross section [m^2]
arraySize=(maxSize-minSize)/stepSize;
signalToNoise(1:arraySize)=0;
signalToNoiseCoherent(1:arraySize)=0;
intI=1;
while (sigma <= maxSize)  % you could vectorize it
  signalToNoise(intI)=peakPower*tau*gainTrans*sigma*areaReceiv/((4*pi)^2)/(range^4)/k/ ...
  systemTemp/losses;

  if (sigma >= 0.01 && sigma <= 0.1)
      sigma
      signalToNoise(intI)
  end
  sigma=sigma+stepSize;
  intI=intI+1;
end

signalToNoiseCoherent=signalToNoise*integration; % the coherent integrated signal to noise...
 ratio (simplified so far)
```

Matlab function: `RadarAnglesError`

```
% This is supposed to be a short script to calculate the standard deviation
% of radar angle-measuerement errors
%
%--------------------------------------------------------------------------
% Source: Curry G.R., 'Radar System Performance Modeling', Artech House
% Publishers, First Edition 2001, pp. 173, Formulas 8.7, 8.8, 8.9, 8.31
%
% Required Inputs: (have to be done in the script directly)
%   - Beamwidth [mR] UNKNOWN UNIT SO FAR
%   - Signal to Noise ratio for detection [dB]
%   - Composite fixed random angle error in the measurement coordinate [mR]
%   - might add some optional inputs later, but not so far
%
% Outputs: (done directly on the Matlab workspace)
%   - Standard deviation of the radar of the radar angular-measurement
%   error [mR]
%
% Date and Author: Jonas Radtke, 05.06.2012
%
%--------------------------------------------------------------------------
function [angleError, angleErrorCoherent]=RadarAnglesError(theta,signalToNoise, ...
signalToNoiseCoherent)
%% calculations
% change signal to noise to dB
kM=1.6; % an assumed normal value
signalToNoise=10*log10(signalToNoise);
intX=find(signalToNoise < 0);
signalToNoise(intX)=0;
signalToNoiseCoherent=10*log10(signalToNoiseCoherent);
intX=find(signalToNoiseCoherent < 0);
signalToNoiseCoherent(intX)=0;

sigmaAN=theta./(kM.*(signalToNoise));
sigmaANCoherent=theta./(kM.*(signalToNoiseCoherent));

angleError=sigmaAN;
angleErrorCoherent=sigmaANCoherent;
```

Matlab function: `RadarRangeError`

```
% this is supposed to be a short script(!) to calculate the STANDARD
% deviation of the radar range-measurement error
%
%-------------------------------------------------------------------------
% Source: Curry G.R., 'Radar System Performance Modeling', Artech House
% Publishers, First Edition 2001, pp. 173, Formulas 8.5, 8.6, 8.30
%
% Required Inputs: (have to be done in the script directly:
%   - Ranges Resolution [m] (deltaR)
%   - Signal to Noise Ration [dB]
%   - Range Fix Er [m]
%
% Outputs: (shown in matlab workspace)
%   - standard deviation of the radar range-measurement error [m]
%
% Author and Date: Jonas Radtke, 05.06.2012
%
%-------------------------------------------------------------------------

%% Inputs:
function [rangeError, rangeErrorCoherent]=RadarRangeError(deltaR,signalToNoise,signalToNoiseCoherent)


%% calculations
% change signal to noise to dB:
sigmaXX=0.0;
sigmaYY=0.0;
signalToNoise=10*log10(signalToNoise);
intX=find(signalToNoise < 0);
signalToNoise(intX)=0;
signalToNoiseCoherent=10*log10(signalToNoiseCoherent);
intX=find(signalToNoiseCoherent < 0);
signalToNoiseCoherent(intX)=0;
% first get the sigma from signal to noise: NOTE: might be clever to do
% both the coherent and normal signal to ratio devitation
sigmaRN=deltaR./(sqrt(2.*signalToNoise));
sigmaRNCoherent=deltaR./(sqrt(2.*signalToNoiseCoherent));

% combining the values to the overall rangeError
rangeError=sqrt(sigmaRN.^2+sigmaXX^2+sigmaYY^2);
rangeErrorCoherent=sqrt(sigmaRNCoherent.^2+sigmaXX^2+sigmaYY^2);
```

C.2 Overview: POSADA

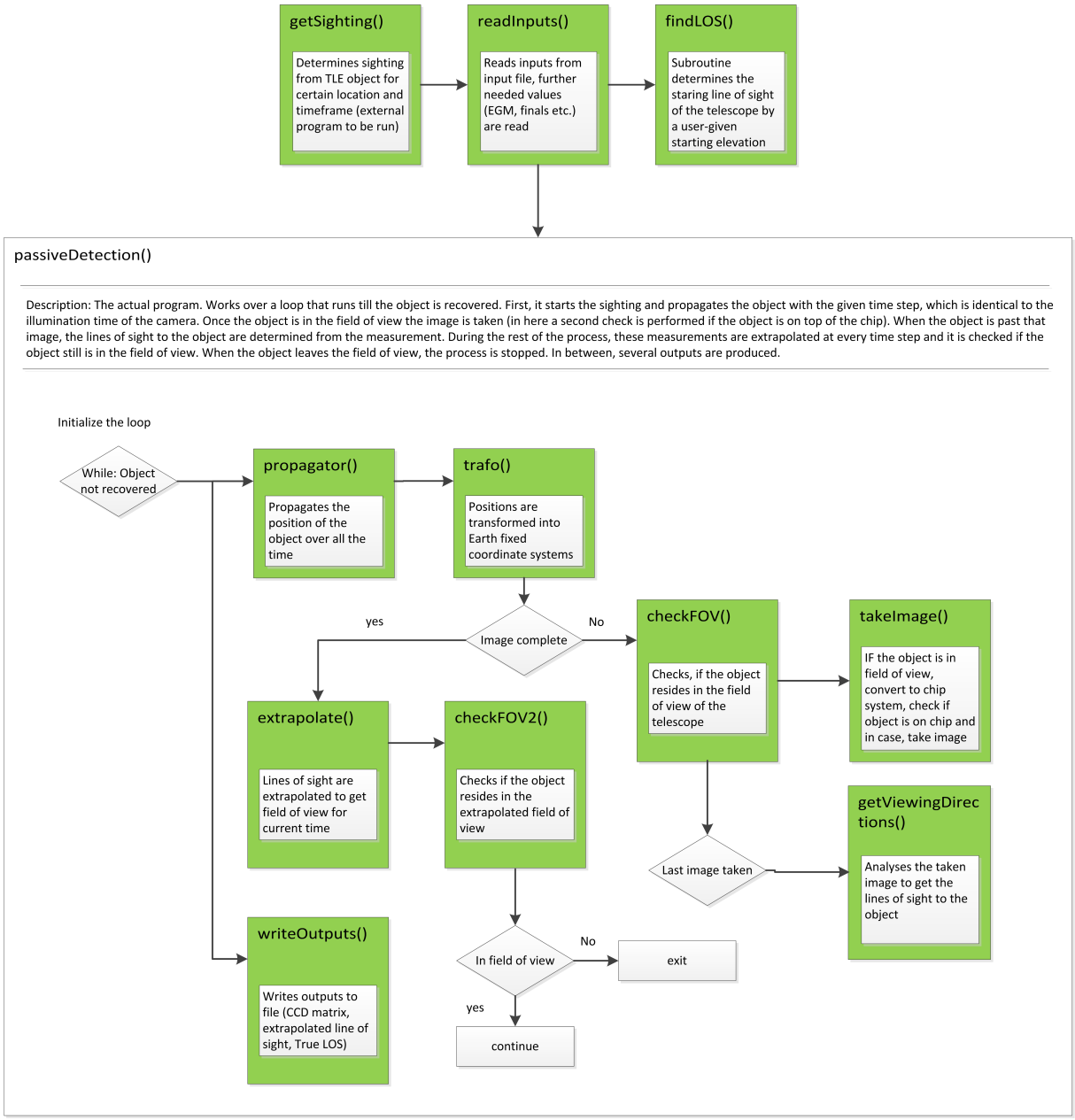

Figure C.1: Flow Chart of the tool POSADA. Note that this flow is rather for an overview of the program than the exact programmatic implementation. Shown is the process for determining the time frame for which a prediction is valid.

Appendix D

Further results from PROOF simulations

At this point, some further results from the simulations performed with PROOF2009 shall be shown. This is for a better overview in the continuous text.

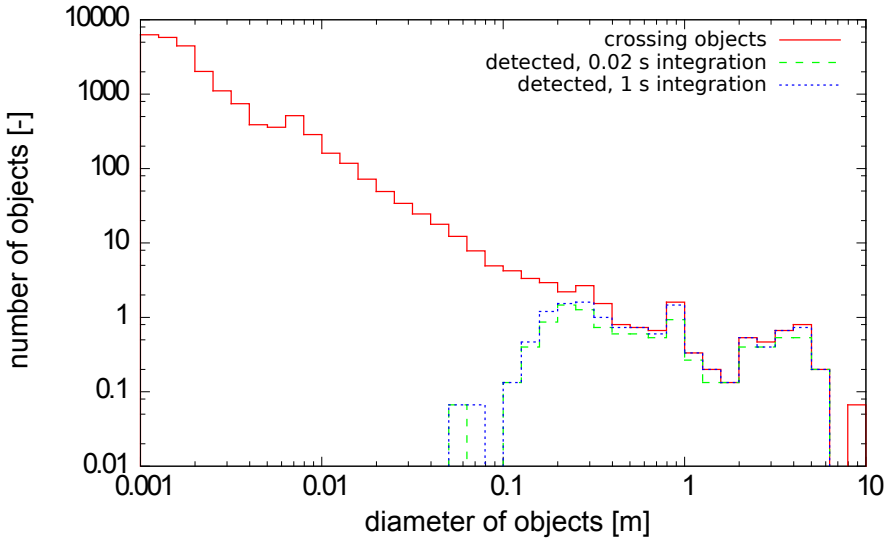

Figure D.1: Detected particles over size for FLI camera without focal reducer on 1st of May 2009; simulation over one night.

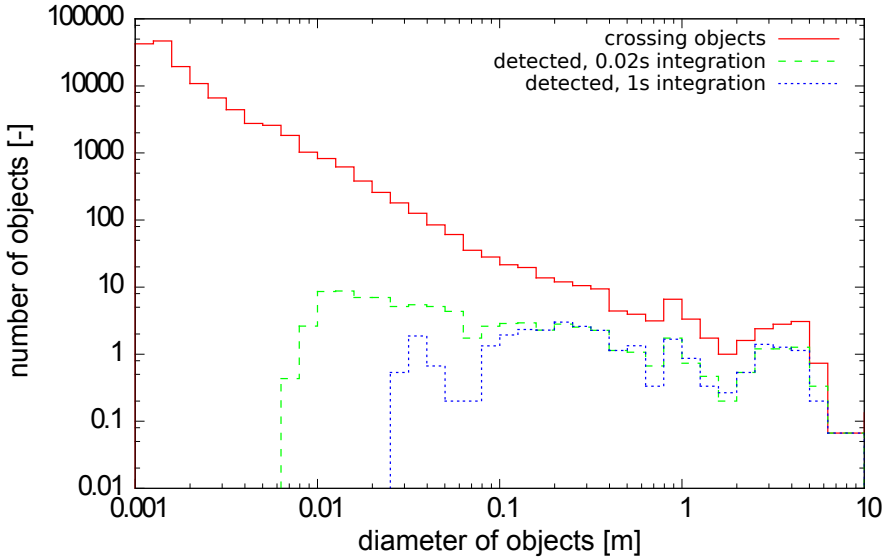

Figure D.2: Detected particles over size for perfect camera without focal reducer on 1st of May 2009; simulation over one night.

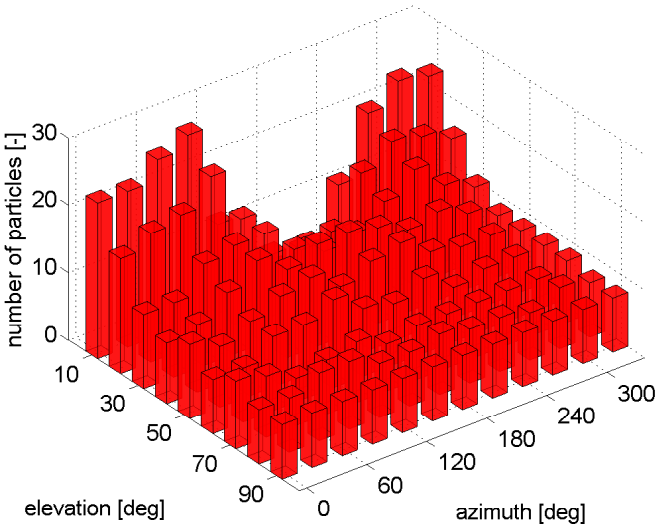

Figure D.3: Number of detected particles over direction for FLI camera without focal reducer on 1st of May 2009; simulation over one night.

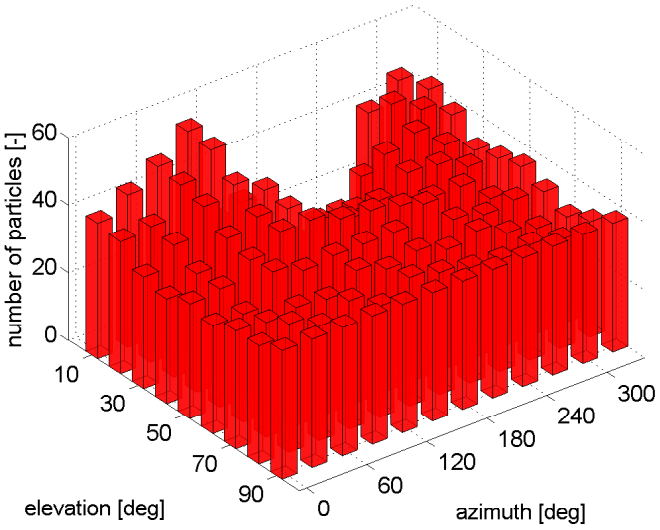

Figure D.4: Number of detected particles over direction for perfect camera without focal reducer on 1st of May 2009; simulation over one night.

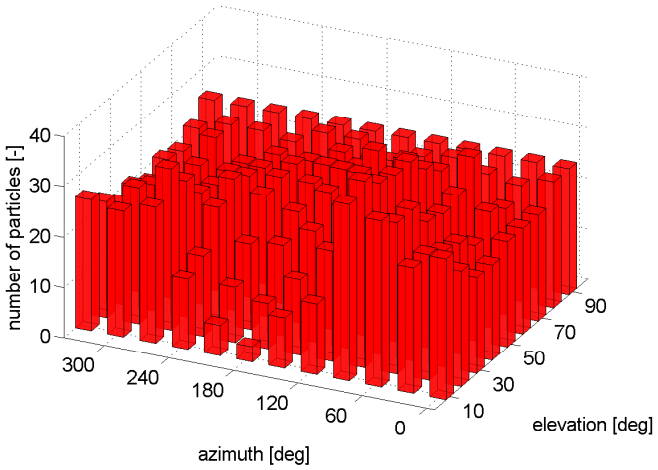

Figure D.5: Number of detected particles over direction for Andor camera with focal reducer on 1st of May 2009; simulation over one night.

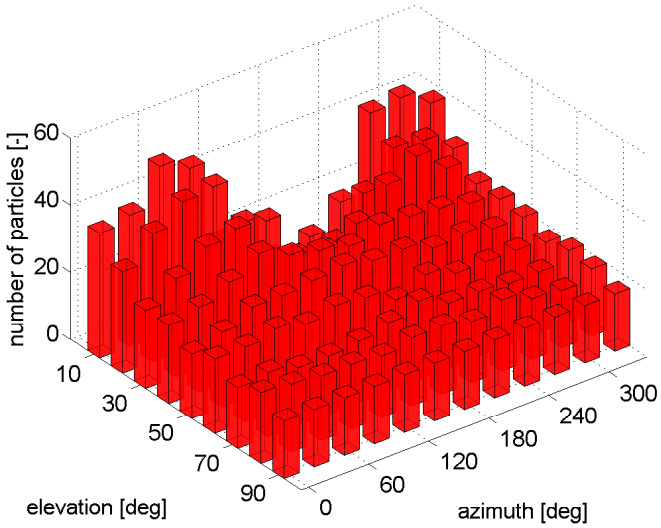

Figure D.6: Number of detected particles over direction for FLI camera with focal reducer on 1st of May 2009; simulation over one night.

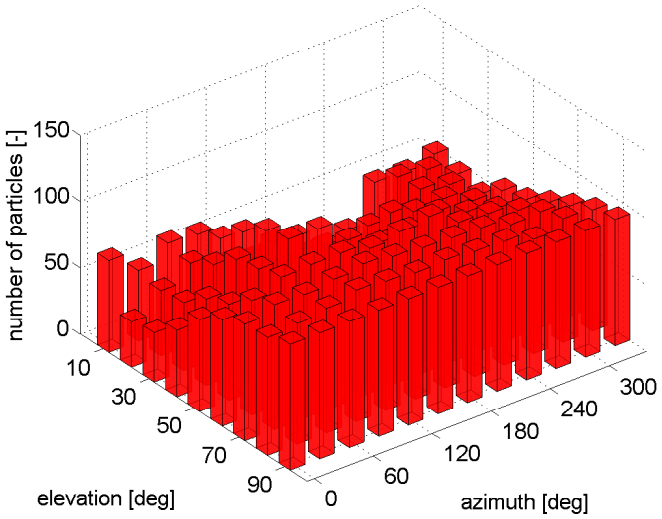

Figure D.7: Number of detected particles over direction for perfect camera with focal reducer on 1st of May 2009; simulation over one night.

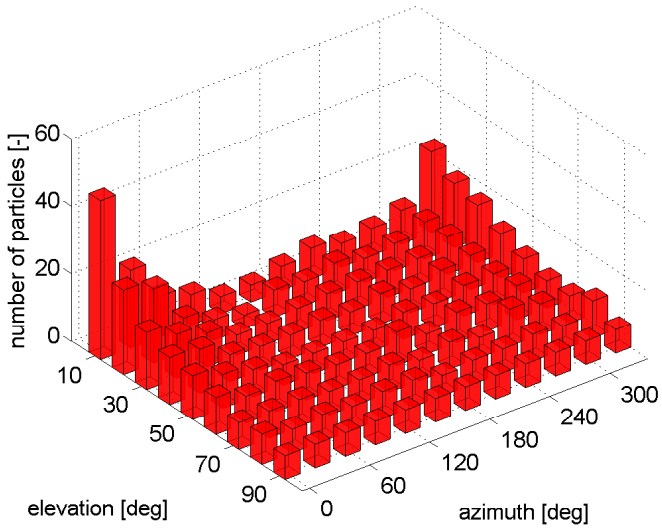

Figure D.8: Number of detected particles over direction for Andor camera without focal reducer on 1st of November 2008; simulation over one night.

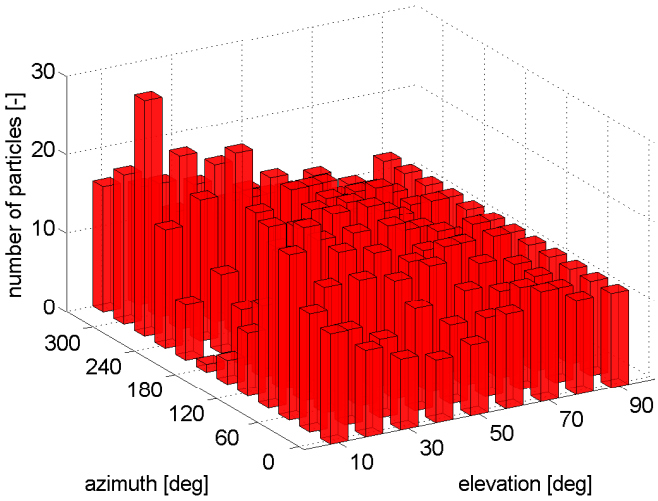

Figure D.9: Number of detected particles over direction for Andor camera without focal reducer on 1st of August 2008; simulation over one night.

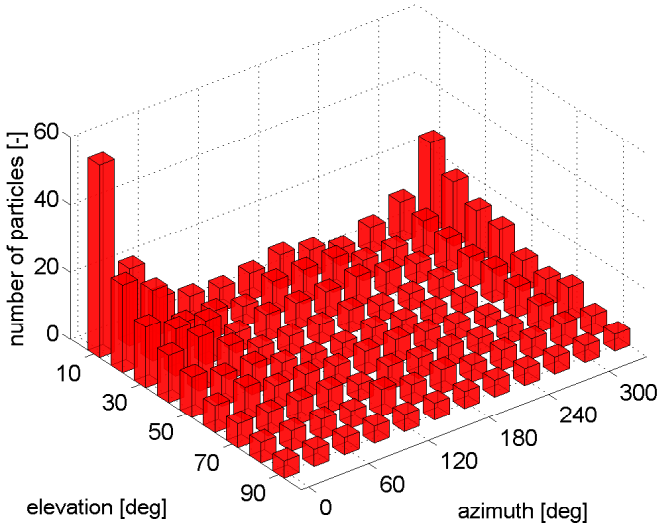

Figure D.10: Number of detected particles over direction for FLI camera without focal reducer on 1st of February 2009; simulation over one night.

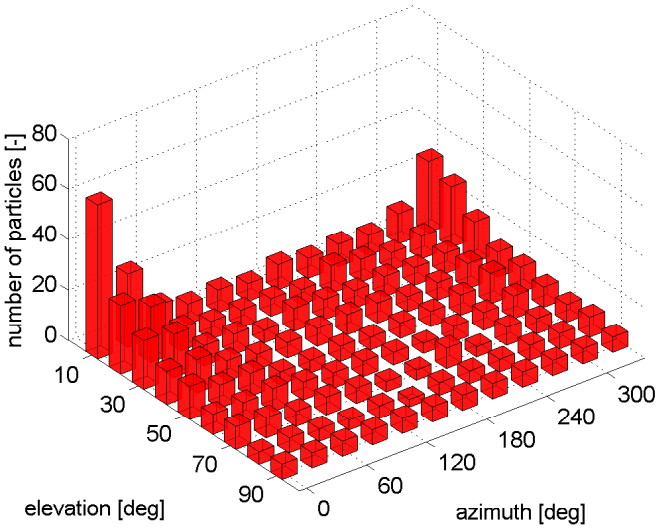

Figure D.11: Number of detected particles over direction for FLI camera without focal reducer on 1st of November 2008; simulation over one night.

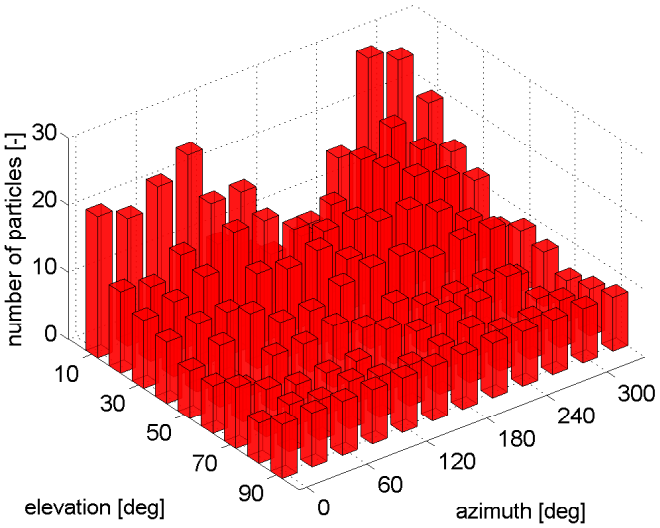

Figure D.12: Number of detected particles over direction for FLI camera without focal reducer on 1st of August 2008; simulation over one night.

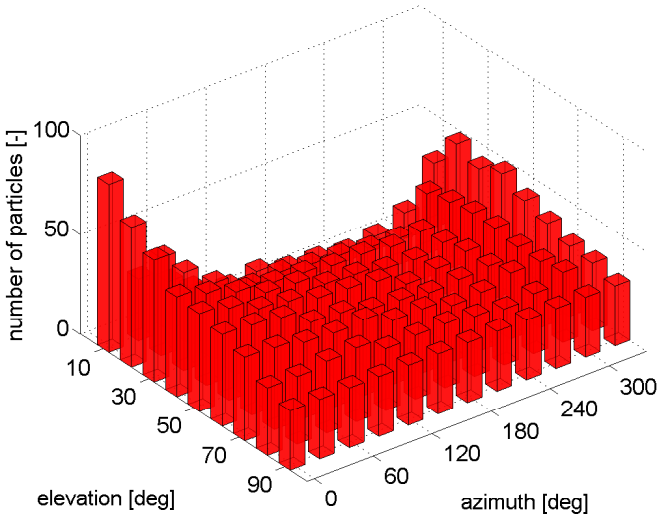

Figure D.13: Number of detected particles over direction for perfect camera without focal reducer on 1st of February 2009; simulation over one night.

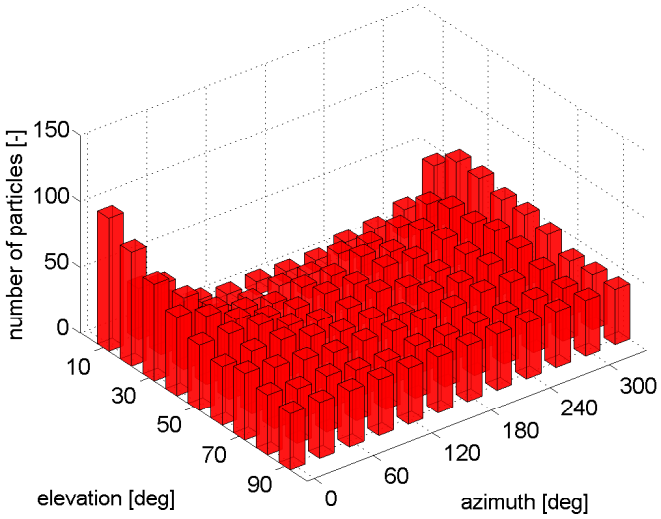

Figure D.14: Number of detected particles over direction for perfect camera without focal reducer on 1st of November 2008; simulation over one night.

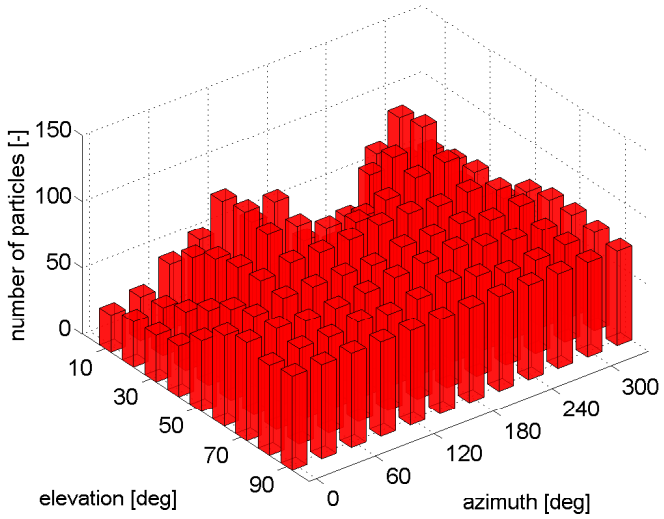

Figure D.15: Number of detected particles over direction for perfect camera without focal reducer on 1st of August 2008; simulation over one night.

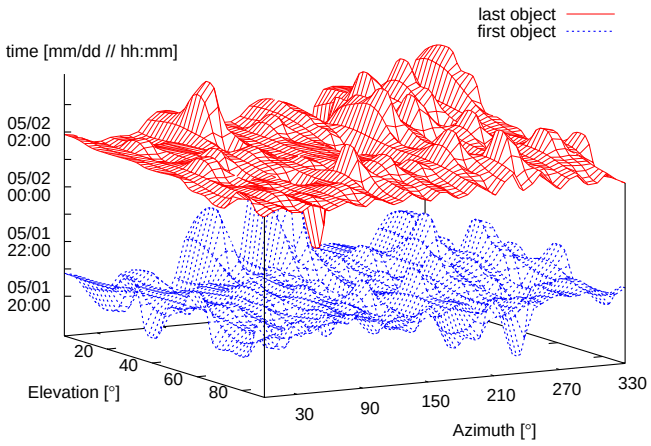

Figure D.16: Detection times of first object over viewing direction for Andor camera without focal reducer on 1st of May 2009; simulation over one night.

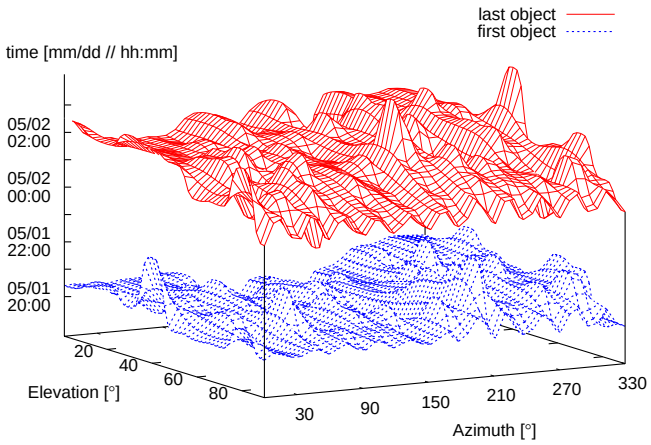

Figure D.17: Detection times of first object over viewing direction for FLI camera without focal reducer on 1st of May 2009; simulation over one night.

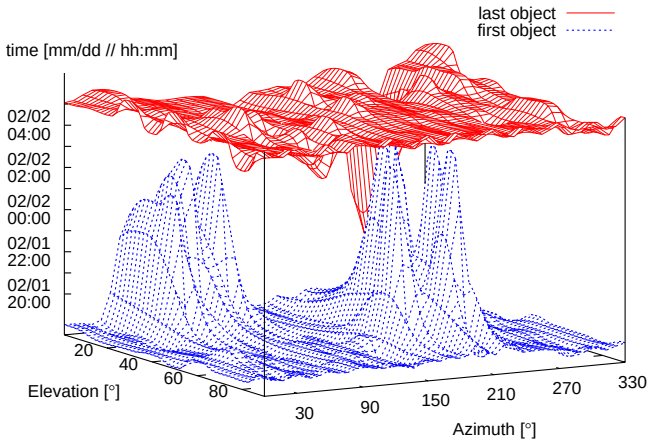

Figure D.18: Detection times of first object over viewing direction for Andor camera without focal reducer on 1st of February 2009; simulation over one night.

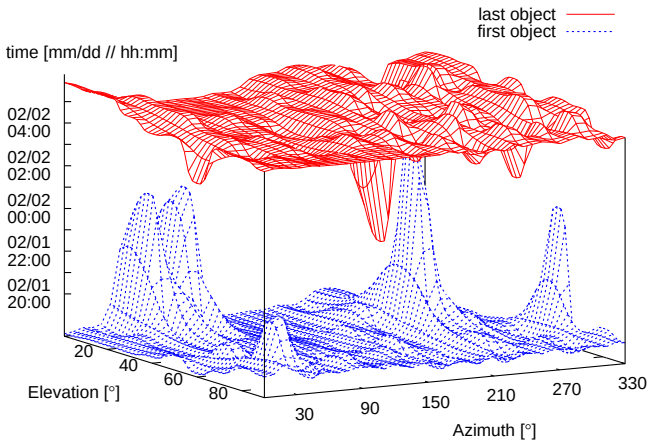

Figure D.19: Detection times of first object over viewing direction for FLI camera without focal reducer on 1st of February 2009; simulation over one night.

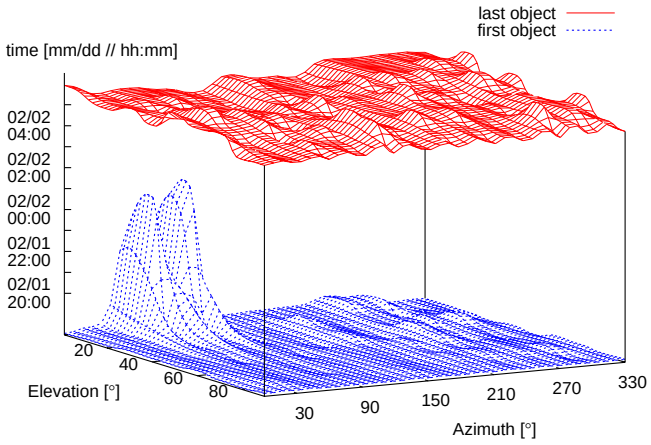

Figure D.20: Detection times of first object over viewing direction for perfect camera without focal reducer on 1st of February 2009; simulation over one night.

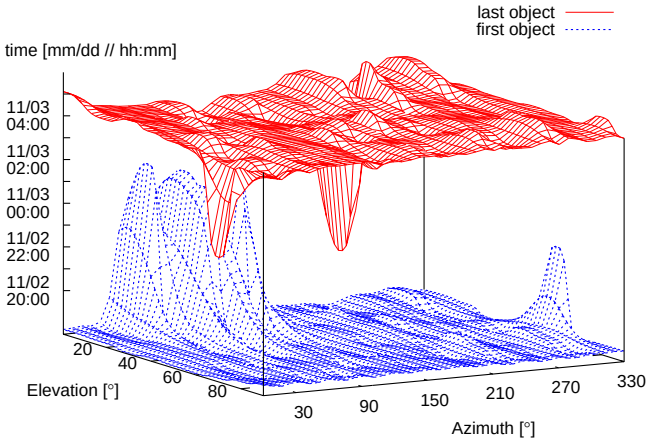

Figure D.21: Detection times of first object over viewing direction for Andor camera without focal reducer on 1st of November 2008; simulation over one night.

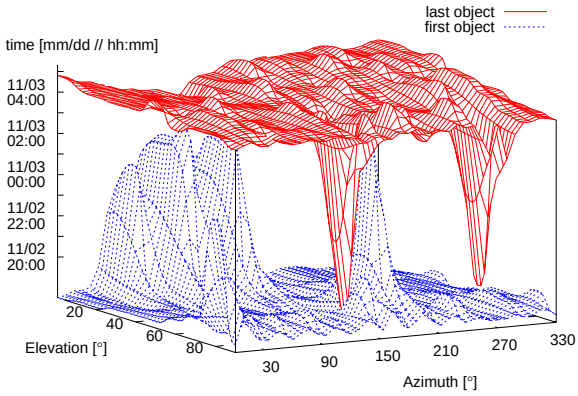

Figure D.22: Detection times of first object over viewing direction for FLI camera without focal reducer on 1st of November 2008; simulation over one night.

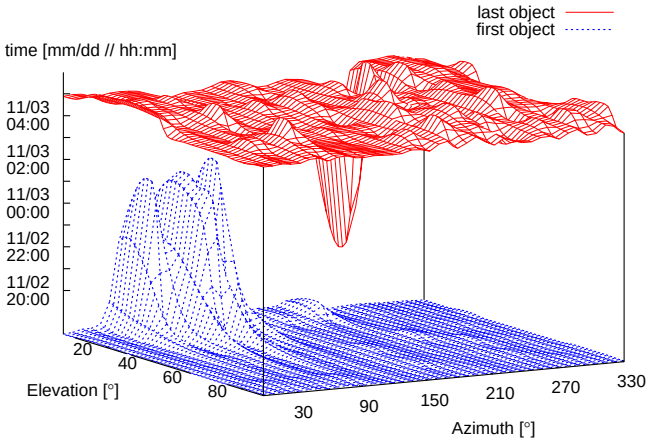

Figure D.23: Detection times of first object over viewing direction for perfect camera without focal reducer on 1st of November 2008; simulation over one night.

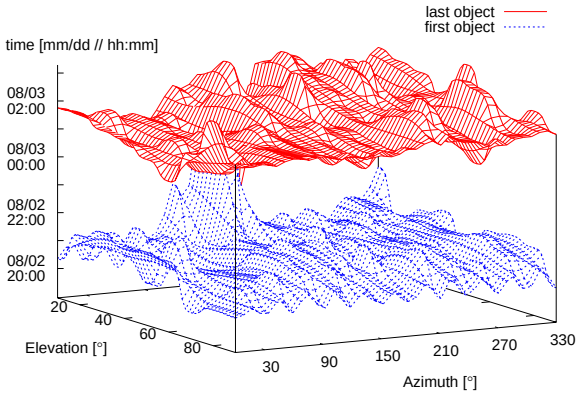

Figure D.24: Detection times of first object over viewing direction for Andor camera without focal reducer on 1st of August 2008; simulation over one night.

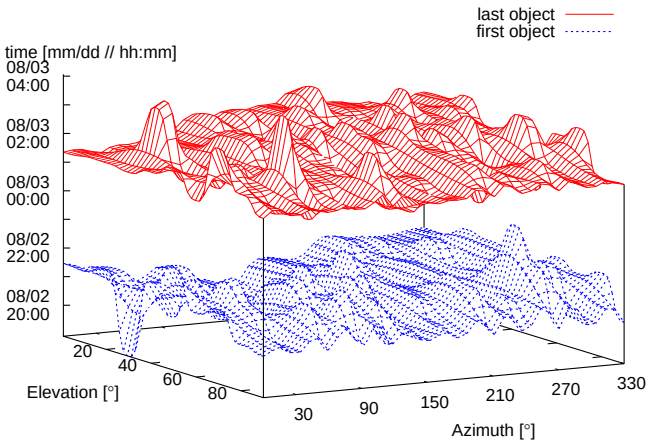

Figure D.25: Detection times of first object over viewing direction for FLI camera without focal reducer on 1st of August 2008; simulation over one night.

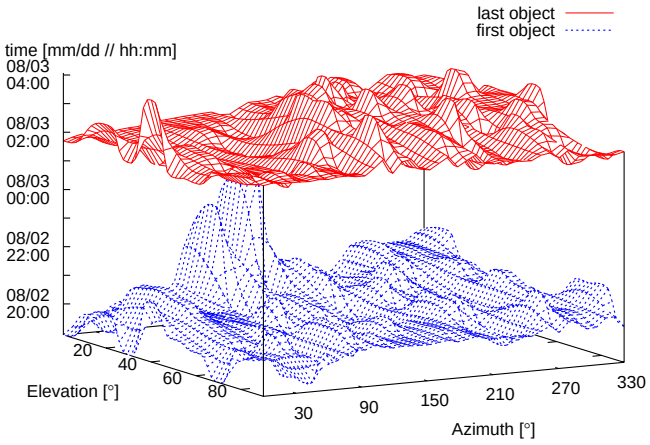

Figure D.26: Detection times of first object over viewing direction for perfect camera without focal reducer on 1st of August 2008; simulation over one night.

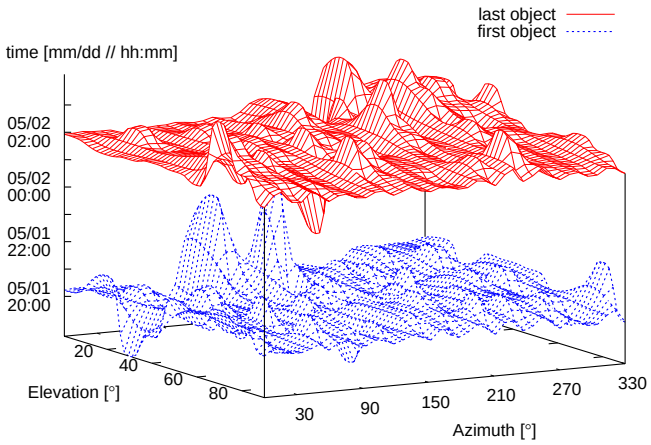

Figure D.27: Detection times of first object over viewing direction for Andor camera with focal reducer on 1st of May 2009; simulation over one night.

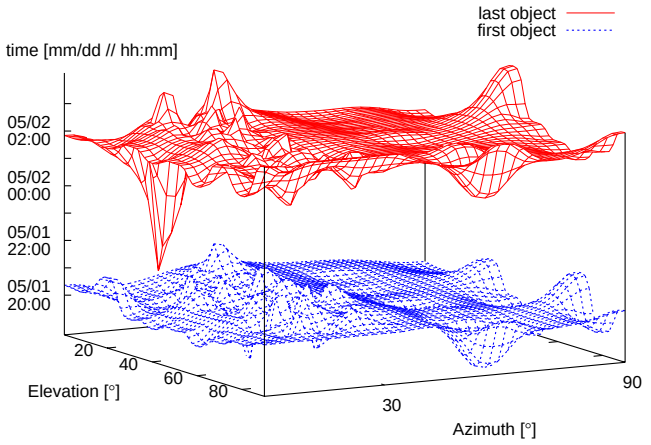

Figure D.28: Detection times of first object over viewing direction for FLI camera with focal reducer on 1st of May 2009; simulation over one night.

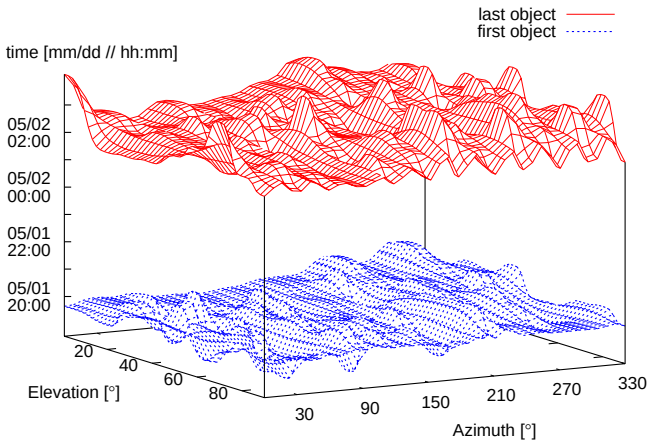

Figure D.29: Detection times of first object over viewing direction for perfect camera with focal reducer on 1st of May 2009; simulation over one night.

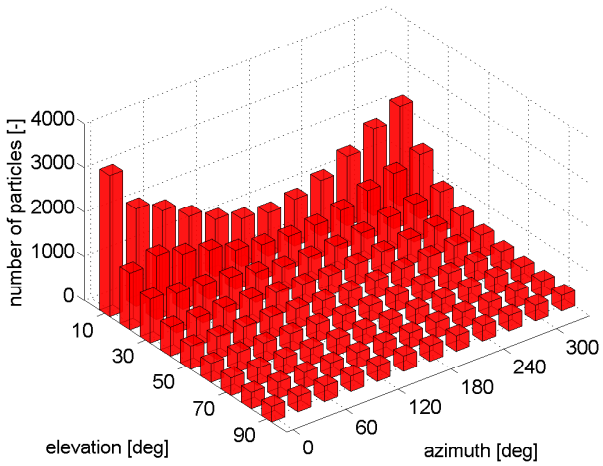

Figure D.30: Total number of crossing objects over viewing direction for Andor camera without focal reducer at Stuttgart site on 1st of February 2009; simulation over one night.

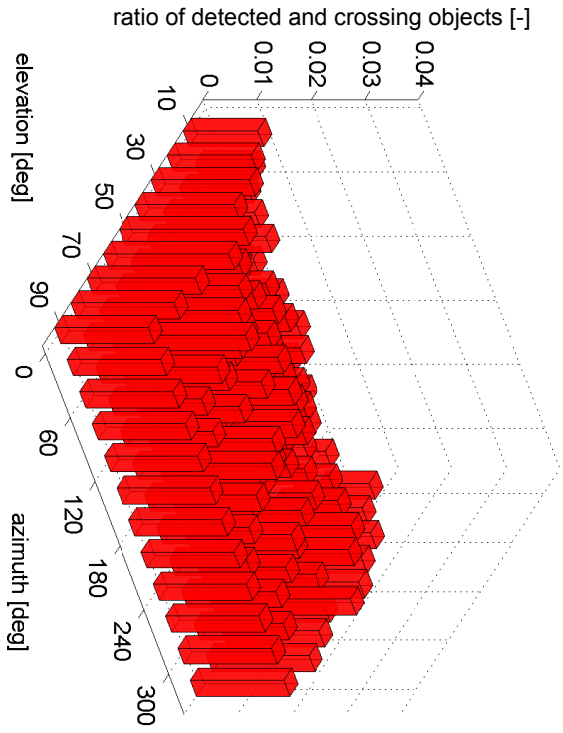

Figure D.31: Relative number of detected objects over crossing objects for Andor camera without focal reducer at Stuttgart site on 1st of February 2009; simulation over one night.

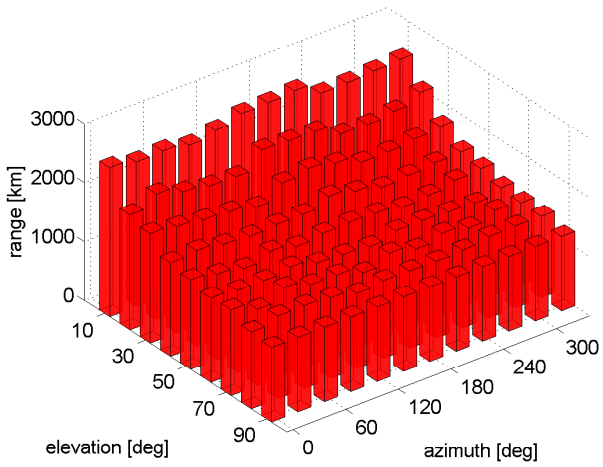

Figure D.32: Average range of all crossing objects over viewing direction for Andor camera without focal reducer at Stuttgart site on 1st of February 2009; simulation over one night.

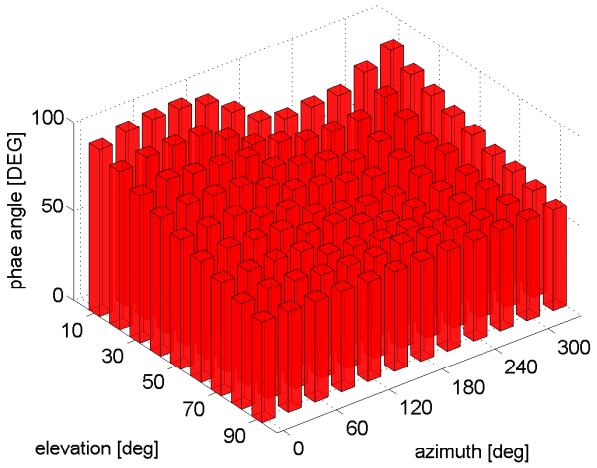

Figure D.33: Average phase angle of all crossing objects over viewing direction for Andor camera without focal reducer at Stuttgart site on February 1st of 2009; simulation over one night

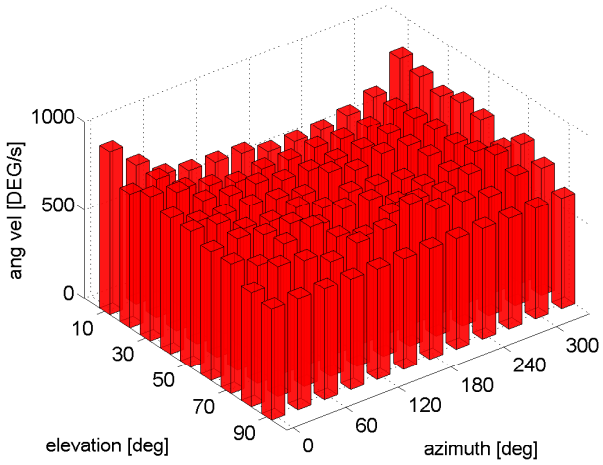

Figure D.34: Illumination of all crossing particles over viewing direction for Andor camera without focal reducer at Stuttgart site on 1st of February 2009; simulation over one night

Table D.1: Total number of detected objects in long term simulations for different cameras without focal reducer on February 1st 2009; each simulation over 30 days.

objects	Andor	FLI
detected objects	1301	1523
different objects	1013	813
fragments	109	40
NaK-droplets	40	0
SRM	0	0
TLE-objects	824	740
Westford-Needles	0	0
MLI	40	33

Table D.2: Total number of detected objects in long term simulations for different cameras without focal reducer on November 1st 2008; each simulation over 30 days.

objects	Andor	FLI
detected objects	1308	1810
different objects	1017	916
fragments	139	58
NaK-droplets	74	0
SRM	0	0
TLE-objects	763	819
Westford-Needles	0	0
MLI	41	39

Table D.3: Total number of detected objects in long term simulations for different cameras without focal reducer on August 1st 2008; each simulation over 30 days.

objects	Andor	FLI
detected objects	622	722
different objects	593	586
fragments	65	34
NaK-droplets	41	0
SRM	0	0
TLE-objects	475	525
Westford-Needles	0	0
MLI	12	27

Table D.4: Preferable viewing directions for different cameras without focal reducer at different sites on 1st of August 2008; each simulation over one night.

site	lat [°]	long [°]	max. particles [-]	LOS (el,az),[°]	min. particles [-]	LOS (el,az), [°]
1	80	0	-	-	-	-
2	80	90	-	-	-	-
3	80	180	-	-	-	-
4	80	270	-	-	-	-
5	45	0	20	10,0	2	10,180
6	45	90	25	10,0	4	10,180
7	45	180	23	10,0	2	10,180
8	45	270	22	10,270	1	10,180
9	0	0	12	90,0	5	10,180
10	0	90	12	90,0	5	45,0
11	0	180	12	90,0	3	45,180
12	0	270	11	10,0	3	10,180
13	-45	0	57	10,180	7	45,0
14	-45	90	53	10,180	6	10,90
15	-45	180	57	10,180	7	10,0
16	-45	270	55	10,180	6	10,90
17	-90	0	151	10,180	26	10,0
18	-90	90	151	10,180	27	45,180
19	-90	180	145	10,180	27	10,0
20	-90	270	149	10,180	27	45,180

Table D.5: Preferable viewing directions for different cameras without focal reducer at different sites on 1st of November 2008; each simulation over one night.

site	**lat** [°]	**long** [°]	**max. particles [-]**	**LOS (el,az),[°]**	**min. particles [-]**	**LOS (el,az), [°]**
1	80	0	122	10,0	20	10,180
2	80	90	120	10,0	23	45,0
3	80	180	122	10,0	19	10,180
4	80	270	128	10,0	22	10,180
5	45	0	55	10,0	5	10,90
6	45	90	58	10,0	7	10,90
7	45	180	57	10,0	6	10,180
8	45	270	54	10,0	7	10,90
9	0	0	12	90,0	4	45,0
10	0	90	12	90,0	4	45,180
11	0	180	10	90,0	5	10,0
12	0	270	11	90,0	4	10,0
13	-45	0	24	10,180	1	10,0
14	-45	90	26	10,180	1	10,0
15	-45	180	28	10,180	1	10,0
16	-45	270	26	10,180	6	10,0
17	-90	0	-	-	-	-
18	-90	90	-	-	-	-
19	-90	180	-	-	-	-
20	-90	270	-	-	-	-

Table D.6: Preferable viewing directions for different cameras without focal reducer at different sites on 1st of February 2009; each simulation over one night.

site	lat [°]	long [°]	max. particles [-]	LOS (el,az),[°]	min. particles [-]	LOS (el,az), [°]
1	80	0	104	10,0	19	10,180
2	80	90	107	10,0	18	10,180
3	80	180	105	10,0	15	10,180
4	80	270	107	10,0	19	10,180
5	45	0	50	10,0	4	10,270
6	45	90	43	10,0	4	10,270
7	45	180	48	10,0	3	10,270
8	45	270	48	10,0	4	10,270
9	0	0	10	90,0	3	10,0
10	0	90	10	45,90	3	45,0
11	0	180	11	10,180	3	45,0
12	0	270	12	90,0	3	45,0
13	-45	0	28	10,180	3	10,0
14	-45	90	28	10,180	2	10,0
15	-45	180	27	10,180	5	10,0
16	-45	270	28	10,180	6	10,0
17	-90	0	-	-	-	-
18	-90	90	-	-	-	-
19	-90	180	-	-	-	-
20	-90	270	-	-	-	-

Table D.7: Preferable viewing directions for different cameras without focal reducer at different sites on 1st of May 2009; each simulation over one night.

site	lat [°]	long [°]	max. particles [-]	LOS (el,az),[°]	min. particles [-]	LOS (el,az), [°]
1	80	0	-	-	-	-
2	80	90	-	-	-	-
3	80	180	-	-	-	-
4	80	270	-	-	-	-
5	45	0	26	10,0	1	10,180
6	45	90	24	10,0	2	10,180
7	45	180	23	10,0	1	10,180
8	45	270	26	10,0	1	10,180
9	0	0	10	90,0	4	45,0
10	0	90	12	90,0	4	45,0
11	0	180	12	45,90	4	45,0
12	0	270	10	45,90	3	45,180
13	-45	0	51	10,180	4	10,270
14	-45	90	52	10,180	4	10,270
15	-45	180	51	10,180	5	10,0
16	-45	270	50	10,180	2	10,270
17	-90	0	123	10,180	25	10,0
18	-90	90	128	10,180	20	10,0
19	-90	180	121	10,180	22	10,0
20	-90	270	124	10,180	24	10,0

Appendix E

Further results from Re-detection analyses

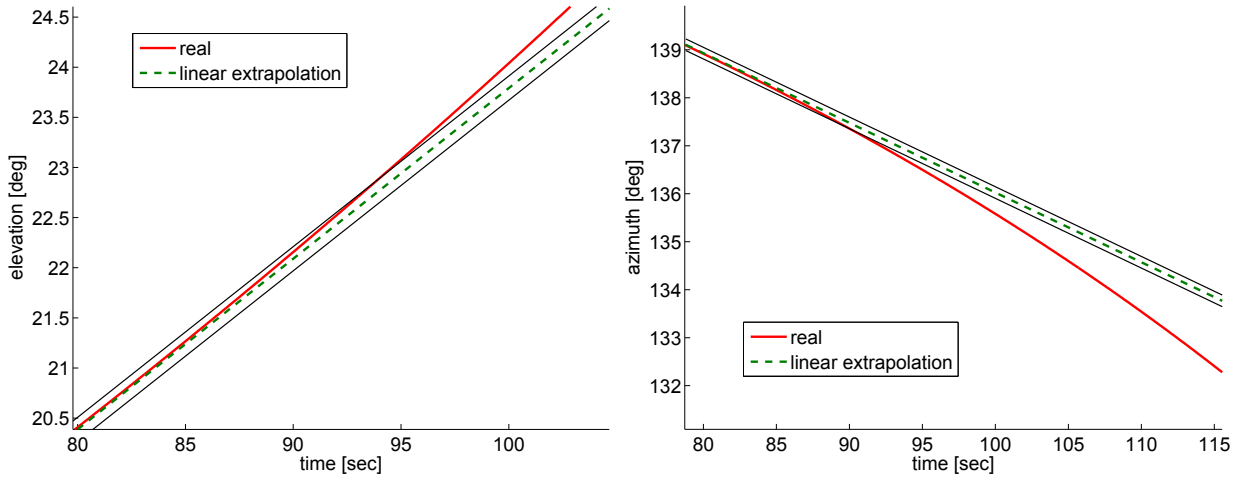

(a) azimuth (b) elevation

Figure E.1: Line of sight predictions for TerrarSarX low elevation pass, Andor camera.

Table E.1: Validity of predictions for TLE objects from table 4.1. Shown are the times for which the state vector of the propagated object stays in the predicted field of view.

Orbit	linear Az [s]	linear El [s]	square Az [s]	square El [s]	total [s]	better
Azur, high, #1	91	64	139	127	127	square
Azur, high, #2	88	37	120	50	50	square
Azur, low, #1	47	>150	150	>150	150	square
Azur, low, #2	21	85	32	38	32	square
CartoSat, high, #1	46	29	66	57	57	square
CartoSat, high, #2	8	17	37	58	37	square
CartoSat, low, #1	23	60	130	63	63	square
CartoSat, low, #2	7	38	18	11	11	square
CryoSat2, high, #1	64	31	82	62	62	square
CryoSat2, high, #2	19	16	54	53	53	square
CryoSat2, low, #1	26	79	71	75	71	square
CryoSat2, low, #2	13	71	13	22	13	linear
GenesisII, high, #1	49	25	70	49	49	square
GenesisII, high, #2	31	15	15	60	15	square
GenesisII, low, #1	25	45	87	57	57	square
GenesisII, low, #2	13	21	13	12	12	linear
MetopA, high, #1	60	36	85	70	70	square
MetopA, high, #2	31	23	24	26	24	square
MetopA, low, #1	32	117	77	83	77	square
MetopA, low, #2	7	94	25	26	26	square

Table E.2: Rising objects from PROOF simulation staring north with an elevation of 20°. The simulation was performed for the Stuttgart site on 1st of May 2009 over one night with the Andor camera.

Object	sma [km]	incl [°]	eccs [-]	AoP [°]	RAAN [°]
#1	7271.10	97.82	0.0414	125.1	287.87
#2	7109.6	98.08	0.0081	57.71	203.77
#4	7774.4	102.36	0.0125	310.51	54.27
#8	7357.00	99.54	0.0014	167.49	59.06
#10	7423.70	89.93	0.0043	24.68	195.94
#12	6973.20	98.41	0.0019	312.56	74.61
#15	7841.90	101.96	0.0039	46.89	255.58
#23	7453.70	98.91	0.0293	162.15	26.15
#28	7083.00	98.99	0.0230	148.26	255.60
#29	7339.50	82.83	0.0063	207.44	213.36
#36	7082.60	86.42	0.0091	138.44	61.34

Table E.3: Rising objects from PROOF simulation staring north with an elevation of 20°. The simulation was performed for the Stuttgart site on 1st of February 2009 over one night with the FLI camera.

Object	sma [km]	incl [°]	eccs [-]	AoP [°]	RAAN [°]
#7	7337.5	82.97	0.008	250.90	190.72
#9	7879.6	73.63	0.0027	72.19	317.44
#10	7215.1	69.96	0.0006	276.35	115.43
#13	7317.0	98.9	0.0124	247.51	221.5
#18	7189.0	98.95	0.0262	312.75	19.96
#20	7160.7	98.25	0.0012	40.29	67.18
#23	7190.1	98.95	0.0052	148.07	28.70
#24	7252.5	98.89	0.003	44.47	71.71
#25	7218.9	71.02	0.0014	194.10	198.95
#26	7265.8	71.11	0.0126	87.31	37.11

Table E.4: Not rising objects from PROOF simulation staring west with an elevation of 20°. The simulation was performed for the Stuttgart site on 1st of May 2009 over one night with the FLI camera.

Object	sma [km]	ecc [-]	incl [°]	AoP [°]	RAAN [°]
#1	7350.60	82.97	0.0018	313.23	18.63
#2	7776.30	82.59	0.0016	104.71	218.86
#3	15776.50	65.40	0.5455	352.42	193.95
#4	7417.50	99.21	0.0004	290.77	54.82
#5	7826.20	74.03	0.0017	340.80	182.66
#7	7086.90	98.42	0.0162	22.77	355.51
#8	6927.60	99.05	0.0094	256.55	250.06
#9	7076.30	98.25	0.0009	131.66	185.37
#11	7352.10	82.92	0.0025	39.80	85.35
#12	7215.10	98.89	0.0037	250.57	339.80
#14	7323.00	100.11	0.0085	87.25	348.38
#18	7235.60	81.25	0.0097	135.36	165.30
#20	7092.60	98.66	0.0015	126.69	15.82
#27	7085.90	99.03	0.0178	150.43	248.07
#29	7271.50	99.30	0.0078	188.95	237.91
#31	7865.20	102.00	0.0055	51.93	234.67
#35	7321.10	82.53	0.0017	290.40	221.55

Table E.5: Not rising objects from PROOF simulation staring east with an elevation of 20°. The simulation was performed for the Stuttgart site on 1st of May 2009 over one night with the Andor camera.

Object	sma [km]	ecc [-]	incl [°]	AoP [°]	RAAN [°]
#3	7188.98	74.2	0.0027	293.45	206.55
#5	7151.0	99.49	0.0503	348.52	269.65
#6	7869.4	74.02	0.0027	301.31	102.74
#7	7273.6	64.93	0.0045	216.61	111.82
#9	7308.30	64.68	0.0047	257.42	68.32
#11	6922.30	73.93	0.0259	305.33	94.38
#13	7074.60	86.61	0.0278	83.72	66.27
#14	7357.30	65.05	0.0040	234.09	170.17
#16	7006.00	66.05	0.0029	47.97	171.17
#17	7905.80	74.04	0.0080	146.70	86.38
#18	7366.50	67.00	0.0101	24.69	105.36
#19	7334.90	65.00	0.0022	215.28	214.04
#20	7176.80	86.32	0.0040	338.51	61.69
#21	7322.30	64.93	0.0051	226.20	232.87
#22	7314.00	82.96	0.0025	147.86	60.68
#24	7815.30	73.99	0.0032	144.05	95.94
#25	7853.60	73.67	0.0019	99.34	107.05
#26	7313.70	64.99	0.0062	223.74	100.39
#27	7865.30	74.01	0.0020	270.32	56.98
#30	7089.30	86.21	0.0153	38.20	82.34
#31	7138.22	73.49	0.0071	43.35	216.33
#32	7287.30	64.88	0.0061	120.35	58.41
#33	7218.80	71.02	0.0011	46.16	8.02
#34	6977.24	81.68	0.0043	214.54	232.60
#35	7861.80	74.02	0.0016	200.75	97.35
#37	7314.80	64.77	0.0098	253.98	203.18

Table E.6: Not rising objects from PROOF simulation staring north with an elevation of 20°. The simulation was performed for the Stuttgart site on 1st of February 2009 over one night with the FLI camera.

Object	sma [km]	ecc [-]	incl [°]	AoP [°]	RAAN [°]
1	7477.00	63.6	0.0140	258.85	141.89
2	7848.4	74.00	0.0009	55.15	60.35
3	8004.2	74.11	0.0191	51.87	35.4
4	7826.1	74.03	0.0018	243.38	299.08
5	7865.7	74.01	0.0026	198.44	134.99
6	7876.00	73.61	0.0026	327.84	81.46
8	10472.4	84.54	0.1112	144.86	300.7
11	7820.80	74.00	0.0020	315.27	295.97
12	7317.00	98.90	0.0124	247.51	221.50
14	7784.2	82.56	0.0005	90.44	274.83
15	7383.1	99.49	0.0303	161.0	75.23
16	8696.9	81.87	0.1532	230.17	358.01
17	7189.00	98.95	0.0262	312.75	18.96
19	7820.1	74.03	0.0027	11.37	273.97
21	7188.50	97.03	0.0184	47.84	36.42
22	7842.330	74.01	0.0015	152.38	43.94

Table E.7: Validity of predictions for rising objects from table E.2. Shown are the times for which the state vector of the propagated object stays in the predicted field of view.

Object #	FLI [s]	Andor [s]	maximum elevation [°]	time visible [s]
#1	72.3	17.7	21.63	129
#2	67.3	21.3	25.15	214
#4	112.6	59.6	33.11	533
#8	101.2	41	27.02	232
#10	112.4	22.7	24.04	256
#12	62.36	42.8	22.11	131
#15	130	58.4	28.77	465
#23	80.1	34.6	27.42	369
#28	65.9	15.2	25.09	204
#29	93	40.4	20.22	67
#36	65	21.2	21.52	110
average	87.5	34.1	25.1	214

[1] median

Table E.8: Validity of predictions for objects from table E.3. Shown are the times for which the state vector of the propagated object stays in the predicted field of view.

Object #	FLI [s]	Andor [s]	maximum elevation [°]	time visible [s]
#7	89.2	59.3	76.88	531
#9	147.6	103.7	25.07	393
#10	101.8	47.7	36.2	384
#13	-	81.1	51.42	486
#18	85.6	35.9	56.96	516
#20	66.4	53.2	47	392
#23	67	52.4	50.7	400
#24	74.8	65.5	56.76	435
#25	85.5	45.7	32.01	351
#26	83.9	31.6	29.27	309
average	89.1	57.6	46.23	396.5[1]

[1] median

Appendix F

Description of work packages

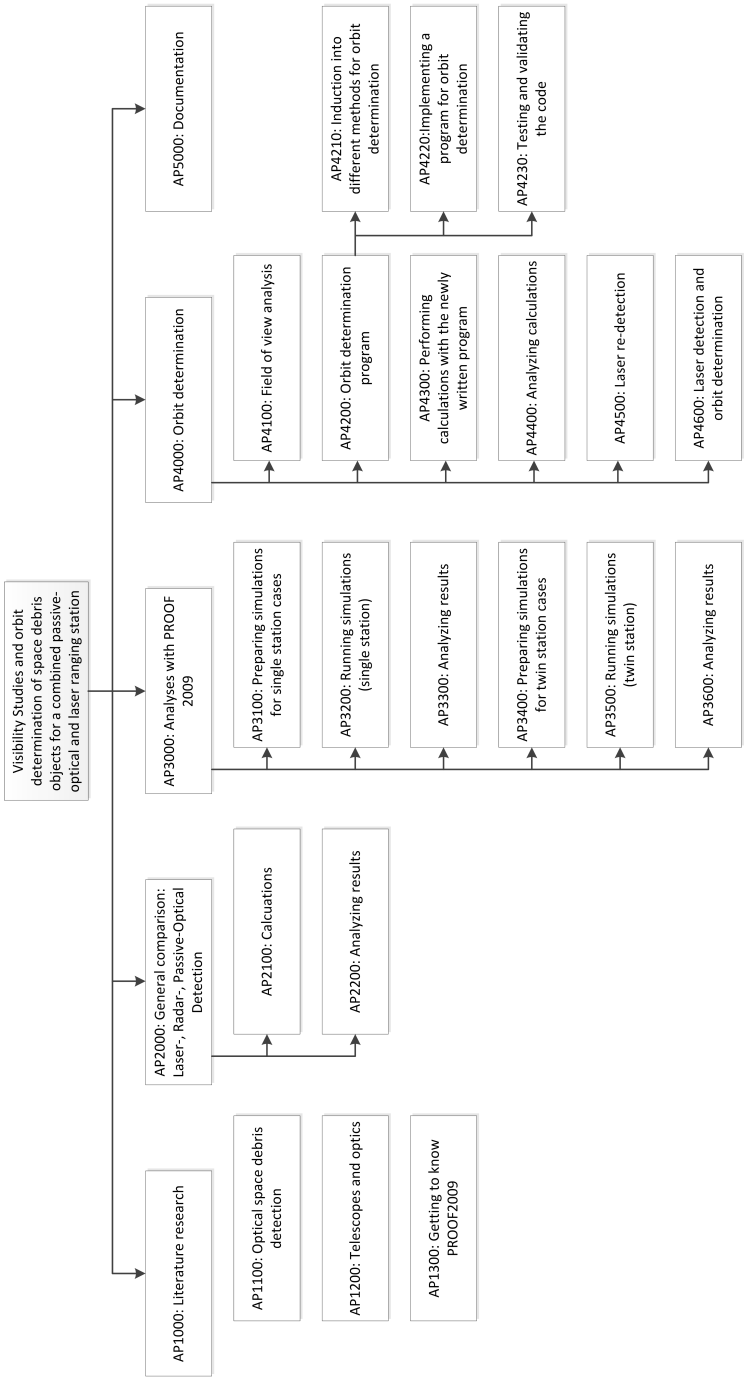

Figure F.1: work breakdown structure

F.1 AP1000: Literature research

		AP 1100
Title	**optical space debris detection**	**Page:** 1 of 21
responsible	Jonas Radtke	**Version:** 1.0
		Date: 15.05.2011
Begin	01.06.2012	
End	15.11.2012	**Duration**: 120 days
Processor	Jonas Radtke	

Aims:
• Achieving basic knowledge regarding optical space debris detection in LEO-Regions (with Laser, Radar, and passive optical ground stations)

Inputs:
• Literature regarding Space Debris Detection

Interfaces to other work packages:
• AP 2100
• AP 2200
• AP 3100
• AP 3400
• AP 4100
• AP 4210
• AP 4500
• AP 4600
• AP 5000

Purpose:
• Building a basic background knowledge in these topics
• Having inputs/starting point to the further work packages

Results:
• Contribution to technical report

		AP 1200
Title	**telescopes and optics**	**Page:** 2 of 21
responsible	Jonas Radtke	**Version:** 1.0
		Date: 15.05.2011
Begin	01.06.2012	
End	15.11.2011	**Duration**: 120 days
Processor	Jonas Radtke	

Aims:
• Achieving basic knowledge regarding telescopes and optics as well as current and future camera techniques

Inputs:
• Literature regarding telescope designs, optics and camera techniques

Interfaces to other work packages:
• AP 2100
• AP 2200
• AP 3100
• AP 3400
• AP 4100
• AP 4210
• AP 4500
• AP 4600
• AP 5000

Purpose:
• Building background knowledge
• Getting an overview of the used techniques
• Having inputs to the other work packages

Results:
• Contribution to technical report

		AP 1300
Title	**PROOF 2009**	**Page:** 3 of 21
responsible	Jonas Radtke	**Version:** 1.0
		Date: 15.05.2011
Begin	01.06.2012	
End	08.06.2012	**Duration**: 6 days
Processor	Jonas Radtke	

Aims:
• Knowing about and how to use PROOF 2009

Inputs:
• PROOF 2009
• PROOF 2009 Final Report [7]
• PROOF 2009 User Manual [26]

Interfaces to other work packages:
• AP 3100
• AP 3200
• AP 3400
• AP 3500
• AP 4100

Purpose:
• Being able to correctly run PROOF 2009 simulations
• Knowing how PROOF 2009 is working (included effects, not included effects, assumptions, estimations etc.)

Results:
• Contribution to technical report

F.2 AP2000: General Comparison of detection methods

		AP 2100
Title	**Calculations**	**Page:** 4 of 21
responsible	Jonas Radtke	**Version:** 1.0
		Date: 15.05.2011
Begin	11.06.2012	
End	22.06.2012	**Duration**: 10 days
Processor	Jonas Radtke	

Aims:
• Being able to compare the different concepts of optical space debris detection

Inputs:
• AP1100 and AP 1200

Interfaces to other work packages:
• AP1100
• AP1200
• AP2200

Purpose:
• Knowing about the theoretical possibilities of the different ground station concepts
• Setting up calculations to get a glance on the accuracies of the different concepts
• Getting inputs for analysis in AP2200

Results:
• Numerical quantities to compare the different concepts

		AP 2200
Title	**Analyzing results**	**Page:** 5 of 21
responsible	Jonas Radtke	**Version:** 1.0
		Date: 15.05.2011
Begin	18.06.2012	
End	29.06.2012	**Duration**: 10 days
Processor	Jonas Radtke	

Aims:
• Overview of the possibilities and fields of use for the different space debris detection principles

Inputs:
• AP1100 and AP1200
• Results from AP2100

Interfaces to other work packages:
• AP1100
• AP1200
• AP2100

Purpose:
• Assessment: Classification of the field of use for a combined laser passive optical station regarding their accuracy

Results:
• Classification of the possibilities and of the fields of use for all different concepts

F.3 AP3000: Analyses with PROOF 2009

		AP 3100
Title	**Preparing Simulations**	**Page:** 6 of 21
responsible	Jonas Radtke	**Version:** 1.0
		Date: 15.05.2011
Begin	02.07.2012	
End	13.07.2012	**Duration**: 10 days
Processor	Jonas Radtke	

Aims:
• Preparing simulations for AP3200

Inputs:
• Knowledge and data gained from AP1000

Interfaces to other work packages:
• AP1000
• AP3200

Purpose:
• Especially knowing what to expect from the planned test ground station in Stuttgart
• Having comparable data for other stations
• Being able to run simulations with PROOF 2009 in AP3200

Results:
• Input files for different cases of single stations to run with PROOF 2009 (reference station, Stuttgart based station, outlook to future technologies ...)

		AP 3200
Title	**Running simulations**	**Page:** 7 of 21
responsible	Jonas Radtke	**Version:** 1.0
		Date: 16.05.2011
Begin	11.07.2012	
End	24.07.2012	**Duration**: 10 days
Processor	Jonas Radtke	

Aims:
• Running simulations for analysis in AP3300

Inputs:
• Input files from AP3100

Interfaces to other work packages:
• AP1000
• AP3100
• AP3300
• AP4230

Purpose:
• Running the simulations to get the results for AP3300
• Furthermore same as in AP3100

Results:
• Outputs from PROOF 2009

		AP 3300
Title	**Analyzing results**	**Page:** 8 of 21
responsible	Jonas Radtke	**Version:** 1.0
		Date: 16.05.2011
Begin	23.07.2012	
End	01.08.2012	**Duration**: 8 days
Processor	Jonas Radtke	

Aims:
• Knowing the performance of single based stations for the different cases
• Estimating the possibilities of a Stuttgart based test station in comparison to a reference station

Inputs:
• Results from AP3200

Interfaces to other work packages:
• AP1000
• AP3200

Purpose:
• Gaining an insight to passive-optical space debris detection regarding different station set-ups and station sites

Results:
• Analysis of single station performances (number of objects, number of new objects etc.)
• Grading of the performance of a Stuttgart based ground station
• Outlook to the possibilities in the future (better cameras)
• Possibilities of a reference station running under optimal conditions

		AP 3400
Title	**Preparing simulations (twin station)**	**Page:** 9 of 21
responsible	Jonas Radtke	**Version:** 1.0
		Date: 16.05.2011
Begin	02.08.2012	
End	15.08.2012	**Duration**: 10 days
Processor	Jonas Radtke	

Aims:
• Preparing simulations for AP3500

Inputs:
• Knowledge and data gained from AP1000

Interfaces to other work packages:
• AP1000
• AP3500

Purpose:
• Assessing a possible improvement of the results (for example for the discovery of new objects) by a combination of two stations
• Being able to run simulations with PROOF 2009 in AP3500

Results:
• Different cases of twin station cases to run with PROOF 2009 (regarding the detection of new objects and the dispersion of the stations)

		AP 3500
Title	**Running simulations (twin station)**	**Page:** 10 of 21
responsible	Jonas Radtke	**Version:** 1.0
		Date: 16.05.2011
Begin	07.08.2012	
End	20.08.2012	**Duration**: 10 days
Processor	Jonas Radtke	

Aims:
• Running simulations for analysis in AP3600

Inputs:
• Input files from AP3400

Interfaces to other work packages:
• AP3400
• AP3600
• AP4230

Purpose:
• Running simulations to get the results for AP3600

Results:
• Outputs from PROOF 2009

		AP 3600
Title	**Analyzing results**	**Page:** 11 of 21
responsible	Jonas Radtke	**Version:** 1.0
		Date: 16.05.2011
Begin	16.08.2012	
End	29.08.2012	**Duration**: 10 days
Processor	Jonas Radtke	

Aims:
• Knowing the change of the performance by combined station in comparison to single stations
• Having a basis for further research in combining stations up to networks

Inputs:
• Results from AP3500

Interfaces to other work packages:
• AP1000
• AP3500

Purpose:
• Getting an impression of the possibilities and the significance of combined stations
• Finding sensible sites for possible twin stations

Results:
• Order of improvement by combining stations

F.4 AP4000: Orbit determination

		AP 4100
Title	**Field of View analysis**	**Page:** 12 of 21
responsible	Jonas Radtke	**Version:** 1.0
		Date: 16.05.2011
Begin	30.08.2012	
End	03.09.2012	**Duration**: 3 days
Processor	Jonas Radtke	

Aims:
• Knowing how long the different detected objects stay in the field of view of the telescope

Inputs:
• AP1000
• Simulation results from AP3200 and AP3500

Interfaces to other work packages:
• AP1000
• AP3200
• AP3500
• AP4200
• AP4300

Purpose:
• Finding out the time available to detect objects for further considerations

Results:
• The field of view time of space debris objects (time available to detect object and estimate the travel direction/orbit)

		AP 4200
Title	**Orbit determination program**	**Page:** 13 of 21
responsible	Jonas Radtke	**Version:** 1.0
		Date: 16.05.2011
Begin	04.09.2012	
End	2.10.2012	**Duration**: 21 days
Processor	Jonas Radtke	

Aims:
• Orbit determination

Inputs:
• for details refer to AP4210-AP4230

Interfaces to other work packages:
• AP4300
• AP4500
• AP4600
• for more details refer to AP4210-AP4230

Purpose:
• Being able to get knowledge about orbit determination from observations, for more details refer to AP4210-AP4230

Results:
• Program to determine the orbit from optical observations

		AP 4210
Title	**Methods of orbit determination**	**Page:** 14 of 21
responsible	Jonas Radtke	**Version:** 1.0
		Date: 16.05.2011
Begin	04.09.2012	
End	11.09.2012	**Duration**: 6 days
Processor	Jonas Radtke	

Aims:
• knowing different methods of orbit determination from observations

Inputs:
• AP1000
• AP4100

Interfaces to other work packages:
• AP1000
• AP4100
• AP4220

Purpose:
• Gaining background knowledge about different orbit determination methods
• Shall contain methods for determining orbits from passive-optical observations (angular measurements only) as well as combined optical-laser measurements (angular and range measurements)

Results:
• usable methods for upcoming AP4220

		AP 4220
Title	**Implementing the code**	**Page:** 15 of 21
responsible	Jonas Radtke	**Version:** 1.0
		Date: 16.05.2011
Begin	12.09.2012	
End	25.09.2012	**Duration**: 10 days
Processor	Jonas Radtke	

Aims:
• Developing a program to determine orbital data from observations

Inputs:
• Knowledge from AP4210

Interfaces to other work packages:
• AP4210
• AP4230

Purpose:
• Coding a program for further considerations of orbit determination from different measurements
• Being able to perform these calculations

Results:
• Runnable program for orbit determination

		AP 4230
Title	**Testing and validating the code**	**Page:** 16 of 21
responsible	Jonas Radtke	**Version:** 1.0
		Date: 16.05.2011
Begin	19.09.2012	
End	02.10.2012	**Duration**: 10 days
Processor	Jonas Radtke	

Aims:
- Testing the code
- Validating the results

Inputs:
- Code from 4220
- Sightings and orbital data from AP3200 and AP3500

Interfaces to other work packages:
- AP3200
- AP3500
- AP4220

Purpose:
- Debugging and testing the written program to have a correctly running one

Results:
- Final version of the program for orbit determination

		AP 4300
Title	**Calculations with program**	**Page:** 17 of 21
responsible	Jonas Radtke	**Version:** 1.0
		Date: 16.05.2011
Begin	03.10.2012	
End	09.10.2012	**Duration**: 5 days
Processor	Jonas Radtke	

Aims:
•

Inputs:
• Field of view times from AP4100
• Program from AP4200

Interfaces to other work packages:
• AP4100
• AP4200
• AP4400

Purpose:
• Setting up a database for further considerations in the upcoming analyses. This might be an iterative process with AP4400.

Results:
• Orbits from passive optical observations

		AP 4400
Title	**Analyzing calculations**	**Page:** 18 of 21
responsible	Jonas Radtke	**Version:** 1.0
		Date: 16.05.2011
Begin	05.10.2012	
End	18.10.2012	**Duration**: 10 days
Processor	Jonas Radtke	

Aims:
• Knowing about performance and accuracy of orbit determination from short time optical observations

Inputs:
• Results from AP4300

Interfaces to other work packages:
• AP4300
• AP4500
• AP4600

Purpose:
• Gaining knowledge about fast time orbit determination methods
• Estimating accuracy from orbit determinations for AP4500

Results:
• Start-off points for following WPs

		AP 4500
Title	**Laser re-detection**	**Page:** 19 of 21
responsible	Jonas Radtke	**Version:** 1.0
		Date: 16.05.2011
Begin	19.10.2012	
End	01.11.2012	**Duration**: 10 days
Processor	Jonas Radtke	

Aims:
• Assessment of the re-detection of space debris objects after detection with a passive-optical system

Inputs:
• knowledge from AP1000
• program from AP4200
• analyzed results from AP4400

Interfaces to other work packages:
• AP1000
• AP4200
• AP4400
• AP4600

Purpose:
• Finding out if and how the re-detection (means: pointing the laser on the objects) of passive-optical detected objects with a laser is possible. Critical aspects will be the determination accuracy and time an object is visible

Results:
• Re-detection

		AP 4600
Title	**Laser detection and orbit determ.**	**Page:** 20 of 21
responsible	Jonas Radtke	**Version:** 1.0
		Date: 16.05.2011
Begin	02.11.2012	
End	15.11.2012	**Duration**: 10 days
Processor	Jonas Radtke	

Aims:
• determining the orbit of a space debris object from laser ranging measurement

Inputs:
• knowledge from AP1000
• program from AP4200
• analyzed results from AP4400
• results from AP4500

Interfaces to other work packages:
• AP1000
• AP4200
• AP4400
• AP4500

Purpose:
• Orbit determination from laser measurements

Results:
• Calculating orbits from laser ranging measurements

F.5 AP5000: Documentation of the results

		AP 5000
Title	**Documentation of the results**	**Page:** 21 of 21
responsible	Jonas Radtke	**Version:** 1.0
		Date: 16.05.2011
Begin	T_0	
End	T_0	**Duration**: 125 days
Processor	Jonas Radtke	

Aims:
• Document the performed work

Inputs:
• results from all prior work packages

Interfaces to other work packages:
• AP1000
• AP2000
• AP3000
• AP4000

Purpose:
• Documenting the project

Results:
• Documentation of all performed work

Name: Jonas Radtke
Date: 15/10/2012

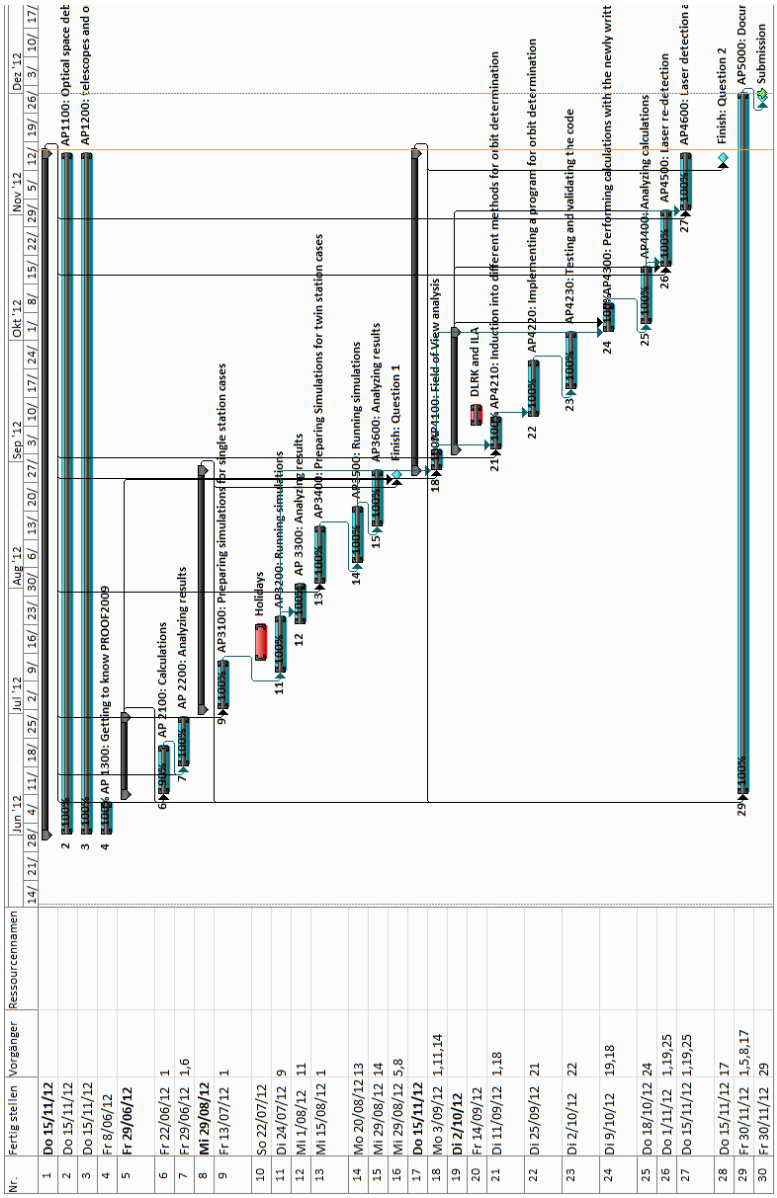

Figure F.2: Gantt-Diagram